

ARO 15646.6-EL

FINAL TECHNICAL REPORT  
PROJECT A-2179

(12)

**NEAR-FIELD THEORY AND TECHNIQUES FOR  
WIDEBAND RADIATING SYSTEMS AT IN-BAND  
AND OUT-OF-BAND FREQUENCIES**

By

B. J. Cown and C. E. Ryan, Jr.

CONTRACT NO. DAAG29-78-C-0029

JULY 1978 through JANUARY 1982

Prepared for

U. S. ARMY RESEARCH OFFICE  
P. O. BOX 12211  
RESEARCH TRIANGLE PARK  
NORTH CAROLINA 27709

DTIC  
ELECTE  
SEP 8 1982  
S D B

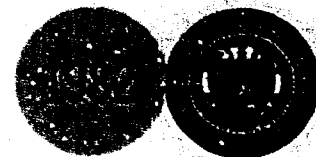
**GEORGIA INSTITUTE OF TECHNOLOGY**

A Unit of the University System of Georgia  
Engineering Experiment Station  
Atlanta, Georgia 30332



**DISTRIBUTION STATEMENT A**

Approved for public release;  
Distribution Unlimited



82 09 07 246

AD A118956

DTIC FILE COPY

UNCLASSIFIED

SECURITY CLASSIFICATION OF THIS PAGE (When Data Entered)

REPORT DOCUMENTATION PAGE		READ INSTRUCTIONS BEFORE COMPLETING FORM																		
1. REPORT NUMBER	2. GOVT ACCESSION NO.	3. RECIPIENT'S CATALOG NUMBER																		
4. TITLE (and Subtitle) Near-Field Theory and Techniques for Wideband Radiating Systems at In-Band and Out-of-Band Frequencies		5. TYPE OF REPORT & PERIOD COVERED Final Technical Report July 14, 1978-JAN. 14, 1982																		
7. AUTHOR(s) B. J. Cown and C. E. Ryan, Jr.		6. PERFORMING ORG. REPORT NUMBER																		
9. PERFORMING ORGANIZATION NAME AND ADDRESS Electromagnetic Effectiveness Division Engineering Experiment Station Georgia Institute of Technology, Atlanta, Georgia 30332		8. CONTRACT OR GRANT NUMBER(s) DAAG29-78-C-0029																		
11. CONTROLLING OFFICE NAME AND ADDRESS Army Research Office P.O. Box 12211 Research Triangle Park, North Carolina 27709		10. PROGRAM ELEMENT, PROJECT, TASK AREA & WORK UNIT NUMBERS																		
14. MONITORING AGENCY NAME & ADDRESS (if different from Controlling Office)		12. REPORT DATE March 1982																		
		13. NUMBER OF PAGES viii + 150																		
		15. SECURITY CLASS. (of this report) Unclassified																		
		15a. DECLASSIFICATION/DOWNGRADING SCHEDULE																		
16. DISTRIBUTION STATEMENT (of this Report)  Approved for public release; distribution unlimited.																				
17. DISTRIBUTION STATEMENT (of the abstract entered in Block 20, if different from Report)																				
18. SUPPLEMENTARY NOTES THE VIEW, OPINIONS, AND/OR FINDINGS CONTAINED IN THIS REPORT ARE THOSE OF THE AUTHOR(S) AND SHOULD NOT BE CONSIDERED AS AN OFFICIAL DEPARTMENT OF THE ARMY POSITION, POLICY, OR DECISION, UNLESS SO DESIGNATED BY OTHER DOCUMENTATION.																				
19. KEY WORDS (Continue on reverse side if necessary and identify by block number) <table border="0"> <tr> <td>site effects</td> <td>waveguide modes</td> <td>coax-to-waveguide adapter</td> </tr> <tr> <td>near-field</td> <td>microwave</td> <td>average value</td> </tr> <tr> <td>wideband</td> <td>reflector antenna</td> <td>standard deviation</td> </tr> <tr> <td>broadband</td> <td>phased array antenna</td> <td>covariance</td> </tr> <tr> <td>out-of-band</td> <td>probability density function</td> <td>correlation</td> </tr> <tr> <td>gain</td> <td>mutual gain</td> <td>antenna coupling</td> </tr> </table>			site effects	waveguide modes	coax-to-waveguide adapter	near-field	microwave	average value	wideband	reflector antenna	standard deviation	broadband	phased array antenna	covariance	out-of-band	probability density function	correlation	gain	mutual gain	antenna coupling
site effects	waveguide modes	coax-to-waveguide adapter																		
near-field	microwave	average value																		
wideband	reflector antenna	standard deviation																		
broadband	phased array antenna	covariance																		
out-of-band	probability density function	correlation																		
gain	mutual gain	antenna coupling																		
20. ABSTRACT (Continue on reverse side if necessary and identify by block number) Theoretical and numerical analyses were performed to study the application of near-field theory and techniques to characterize the radiation and coupling characteristics of wideband, in-band and out-of-band pulsed or cw radiating systems. Specifically, theory and equations were developed for characterizing the radiation patterns of wideband cw or pulsed antennas over both in-band and out-of-band frequency intervals from measured data collected via near-field																				

DD FORM 1 JAN 73 1473

EDITION OF 1 NOV 58 IS OBSOLETE

UNCLASSIFIED

SECURITY CLASSIFICATION OF THIS PAGE (When Data Entered)

UNCLASSIFIED

SECURITY CLASSIFICATION OF THIS PAGE(When Data Entered)

measurement techniques. The results are applicable to either phased array or reflector antennas. Three analytical techniques for analyzing the in-band and out-of-band coupling between pairs of cosited antennas were studied. The three techniques are (1) the Plane Wave Spectrum (PWS), (2) the Spherical Wave Spectrum (SWS), and Geometrical Theory of Diffraction (GTD). The existing theory and equations that are applicable to selected common waveguide components under normal in-band operation were extended to describe wideband out-of-band responses. Also, the theory and equations were formulated for computing the higher-order mode coefficients at the aperture of a waveguide radiating element from a knowledge of the measured far-field electric field of the radiating element when surrounded by a large conducting ground plane. Equations for describing the effects of near-field obstacles located in the antennas' forward half-plane on the performance of a wideband cw or pulsed antenna were derived via the Plane Wave Spectrum (PWS) analysis technique. The resultant statistical average pattern versus frequency is expressed explicitly in terms of the antenna system mode excitation statistical parameters.

UNCLASSIFIED

SECURITY CLASSIFICATION OF THIS PAGE(When Data Entered)

**FINAL TECHNICAL REPORT**

**PROJECT A-2179**

**NEAR-FIELD THEORY AND TECHNIQUES FOR WIDEBAND  
RADIATING SYSTEMS AT IN-BAND AND OUT-OF-BAND FREQUENCIES**

**By**

**B. J. Cown and C. E. Ryan, Jr.**

**Contract No. DAAG29-78-C-0029**

**July 1978 through *JANUARY 1982***

**Prepared for**

**U.S. Army Research Office  
P.O. Box 12211  
Research Triangle Park, North Carolina 2709**

**Prepared by**

**Electromagnetic Effectiveness Division  
Electronics Technology Laboratory  
Engineering Experiment Station  
Georgia Institute of Technology  
Atlanta, Georgia 30332**

## FOREWORD

The research on this program was performed by personnel of the Electromagnetic Effectiveness Division of the Electronics and Computer Systems Laboratory of the Engineering Experiment Station at the Georgia Institute of Technology, Atlanta, Georgia 30332. Dr. C. E. Ryan, Jr. served as the Project Director. This program is sponsored by the Army Research Office, P.O. Box 12211, Research Triangle Park, North Carolina 27709, and is designated by Georgia Tech as Project A-2179. This Final Technical Report covers the period from July 14, 1978 through March 14, 1982. The report summarizes the key results obtained during this period and is required by the contract. Technical discussions with and suggestions of Paul Majors of the U.S. Army Communications Research and Development Command, Ft. Monmouth, New Jersey 07703, are gratefully acknowledged. The authors also cite the considerable clerical skills of Ms. Beatriz Gonzalez in preparing this report.

Respectfully submitted,

*Barry J. Cown*

Barry J. Cown  
Associate Project Director

Approved:

*Charles E. Ryan, Jr.*

Charles E. Ryan, Jr.  
Chief,  
EM Effectiveness Division

Accession For	
NTIS GRA&I	<input checked="checked" type="checkbox"/>
DTIC TAB	<input type="checkbox"/>
Unannounced	<input type="checkbox"/>
Justification	
<b>PER CALL J.C.</b>	
By	
Distribution/	
Availability Codes	
Dist	Avail and/or Special
<b>A</b>	



## TABLE OF CONTENTS

<u>Section</u>	<u>Page</u>
I. INTRODUCTION. . . . .	1
II. THEORY AND TECHNIQUES FOR WIDEBAND ANTENNA PATTERN CHARACTERIZATION. . . . .	7
A. Introduction. . . . .	7
B. Frequency Domain Analysis . . . . .	9
1. Basic Equations . . . . .	9
2. Frequency-Averaged Statistical Average Antenna Patterns. . . . .	16
3. Reduction of Data Measurement Requirements. . . . .	19
C. Near-Field Covariance Study . . . . .	22
1. Analysis of Wire Array. . . . .	24
2. Numerical Study of Wire Array . . . . .	29
3. Recovery of Covariance Functions from Measured Data . . . . .	41
D. Probability Density Functions . . . . .	46
E. Time Domain Statistics. . . . .	59
III. NEAR-FIELD ANTENNA-ANTENNA COUPLING . . . . .	65
A. Introduction. . . . .	65
B. PWS Analysis. . . . .	65
C. Spherical Wave Spectrum Coupling Analysis . . . . .	87
D. GTD Analysis. . . . .	93
IV. SYSTEM DEVICE EFFECTS . . . . .	99
A. Introduction. . . . .	99
B. Computation of Mode Coefficients From Measured Out-of-Band Pattern Data. . . . .	99
C. Summary of Out-of-Band Waveguide Device Characteristics . . . . .	105
1. Waveguide Radial Bends. . . . .	106
2. Ferrite Phase Shifter . . . . .	106
3. Study of the Coax-to-Waveguide Adapter Device. . . . .	111
V. SITE EFFECTS. . . . .	119
A. Introduction. . . . .	119
B. PWSS Formulation. . . . .	119
1. Plane Wave Spectrum Analysis Concept. . . . .	120
2. Wideband Analysis . . . . .	124
C. Time Domain Simulations . . . . .	130
VI. CONCLUDING REMARKS AND RECOMMENDATIONS. . . . .	141
A. Summary of Results. . . . .	141
B. Recommendations . . . . .	144
VII. REFERENCES. . . . .	147

# LIST OF FIGURES

<u>Figure</u>		<u>Page</u>
1-1.	Diagram depicting the allowed higher order modes versus frequency for WR-284 S-band rectangular waveguide. . . . .	2
1-2.	Sketches depicting the transverse electric fields for the indicated higher-order modes in rectangular waveguide. . . . .	3
2-1.	Sketch depicting a linear array of waveguide elements and hypothetical out-of-band amplitude and phase responses at a near-field measurement point. . . . .	10
2-2.	Out-of-band antenna patterns for a randomly-excited 20-element array of multimoding waveguide elements for the cross polarization sense for statistical average power flow of 0.2 watt each in the TE <sub>10</sub> , TE <sub>20</sub> , TE <sub>01</sub> , TE <sub>11</sub> and TM <sub>11</sub> waveguide modes. . . . .	18
2-3.	Error in the relative power level versus the nominal error-free power level for the indicated near-field measurement sample spacings for a 5.0 degree RMS phase measurement error. . . . .	20
2-4.	RMS beam pointing error as a function of RMS phase error for an antenna whose 3-dB beamwidth is nominally 0.5 degrees for the indicated sample spacings. . . . .	21
2-5.	Sketch of an array of center-fed wire elements and near-field sample points. . . . .	25
2-6.	Sketch showing array and near-field parameters for the numerical simulation, where $\lambda_0$ is the wavelength at the in-band frequency of 3.0 GHz . . . . .	31
2-7.	Non-random near-field power distribution for the in-band frequency of 3.0 GHz for the in-band scan angle of 0 degrees. . . . .	32
2-8.	Intrinsic (A) and total (B) near-field covariance function of the electric field at y=0 and the conjugate of the electric field at all other points on the near-field plane for the in-band frequency of 3 GHz for the in-band scan angle of 0 degrees. .	33

## LIST OF FIGURES

<u>Figure</u>		<u>Page</u>
2-9.	Intrinsic (A) and total (B) near-field covariance function of the electric field at $y=-20$ and the conjugate of the electric field at all other points on the near-field plane for the in-band frequency of 3 GHz for the in-band scan angle of 0 degrees. . .	34
2-10.	Analytical statistical average pattern for a nine-element dipole array of interacting (B) and non-interacting (A) elements for the in-band frequency of 3.0 GHz for the in-band scan angle of 0 degrees. .	35
2-11.	Non-random near-field power distribution for the out-of-band frequency of 9.0 GHz for the in-band scan angle of 0 degrees . . . . .	36
2-12.	Intrinsic (A) and total (B) near-field covariance function of the electric field at $y=0$ and the conjugate of the electric field at all other points on the near-field plane for the in-band frequency of 9 GHz for the in-band scan angle of 0 degrees. . .	37
2-13.	Intrinsic (A) and total (B) near-field covariance function of the electric field at $y=-20$ and the conjugate of the electric field at all other points on the near-field plane for the in-band frequency of 9 GHz for the in-band scan angle of 0 degrees. . .	38
2-14.	Analytical statistical average pattern for a nine-element dipole array of interacting (B) and non-interacting (A) elements for the in-band frequency of 9.0 GHz for the in-band scan angle of 0 degrees. .	39
2-15.	The exact and the approximate element current covariance function for the 9-element wire array for the frequency of 3.0 GHz for uncorrelated input voltages. . . . .	45
2-16.	The exact and the approximate near-field covariance function for the electric field at $y=0$ with the conjugate of the electric field at all other sample points on the measurement plane . . . . .	47
2-17.	Cumulative probability distribution for the radiated power density of a mainbeam or grating lobe for a 9-element wire array with uncorrelated random input voltages. . . . .	54



# LIST OF FIGURES

<u>Figure</u>		<u>Page</u>
2-13.	Cumulative probability distribution for the radiated power density of a low sidelobe for a 9-element wire array with uncorrelated random input voltages. . . . .	55
2-19.	Cumulative probability distribution for the radiated power density of a mainbeam or grating lobe for a 9-element wire array with uncorrelated random input voltages . . . . .	56
2-20.	Cumulative probability distribution for the radiated power density of a low sidelobe for a 9-element array with correlated random input voltages. . . . .	57
2-21.	Cumulative probability distribution for the radiated power density of the mainbeam or grating lobe for a 9-element array with uncorrelated input voltages. . . . .	60
2-22.	Cumulative probability distribution for the radiated power density of a low sidelobe for a 9-element array with correlated voltage sources . .	61
3-1.	Sketch depicting the arrangement of two antennas appropriate for the PWS analysis of coupling. . . .	67
3-2.	Sketch depicting the azimuth rotation angle $-\alpha$ and the elevation rotation angle $\beta$ associated with Antenna B of Figure 1. . . . .	68
3-3.	Sketch depicting the antenna aperture coordinates $Y_k, Z_k$ and the optical transform angle $\zeta_{lk}$ . . . . .	70
3-4.	Sketch of the near-field arrangement of Antenna A and Antenna B used in the numerical simulations . .	73
3-5.	Far-field antenna pattern for Antenna A at the in-band frequency of 5.5 GHz for waveguide feed power flow entirely in the $TE_{10}$ mode. . . . .	74
3-6.	Far-field antenna pattern for Antenna B at the in-band frequency of 5.5 GHz for waveguide feed power flow entirely in the $TE_{10}$ mode. . . . .	75

# LIST OF FIGURES

<u>Figure</u>		<u>Page</u>
3-7.	Far-field antenna pattern for Antenna A at the out-of-band frequency of 6.5 GHz for equal waveguide power flow in the TE <sub>10</sub> and TE <sub>20</sub> modes with relative phase angle of 35 degrees. . . . .	76
3-8.	Far-field antenna pattern for Antenna B at the out-of-band frequency of 6.5 GHz for equal waveguide power flow in the TE <sub>10</sub> and TE <sub>20</sub> modes with relative phase angle of -50 degrees . . . . .	77
3-9.	Mutual Gain versus rotation angle for both antennas operating in-band at 5.5 GHz for waveguide feed power flow entirely in the TE <sub>10</sub> mode for the longitudinal separation distance X = 20 feet and the transverse separation distance Y = 0 feet . . . .	79
3-10.	Mutual Gain versus rotation angle for both antennas operating in-band at 5.5 GHz for waveguide feed power flow entirely in the TE <sub>10</sub> mode for the longitudinal separation distance X = 20 feet and the transverse separation distance Y = 5 feet . . . .	80
3-11.	Mutual Gain versus rotation angle for both antennas operating out-of-band at 6.5 GHz for equal waveguide feed power flow in the TE <sub>10</sub> and TE <sub>20</sub> modes with relative phase of 35 degrees for Antenna A and -50 degrees for Antenna B for the longitudinal separation distance X = 20 feet and the transverse separation distance Y = 5 feet . . . . .	81
3-12.	Antenna-to-antenna coupling geometry with an interposed obstacle employed for the plane wave spectrum scattering analysis. . . . .	84
3-13.	Mainbeam antenna decoupling caused by 24-inch and 6-inch diameter circular cylinders located on the boresight axis between two 48-inch diameter vertically-polarized paraboloidal antennas operating at 5.5 GHz . . . . .	85
3-14.	Measured and computed mutual gain versus azimuth rotation angle of the receiving antenna with (a) a clear site between the two antennas and (b) an intervening 12.0-foot tall, 2.0-foot diameter mast located midway (X <sub>c</sub> =8.5 feet) between the two antennas for the indicated antenna separation distance R = 17.0 feet, for vertically polarized signals at 5.5 GHz. The aperture diameter of each paraboloidal reflector antenna is 4.0 feet. . . . .	86

# LIST OF FIGURES

<u>Figure</u>		<u>Page</u>
3-15.	Sketch depicting two arbitrarily oriented near-field antennas and geometric parameters. . . . .	88
3-16.	Sketch depicting the azimuth rotation angle and the elevation rotation angle associated with Antenna B of Figure 2. . . . .	89
3-17.	Sketch depicting the linear distances and the angles used in the GTD antenna coupling analysis . .	94
3-18.	Diffraction by a half-plane showing the incident ( $\theta_i$ ) and scattering ( $\theta_s$ ) angles used in the diffraction coefficient. . . . .	98
4-1.	Sketch depicting a rectangular waveguide transmission line terminating in a large "ground plane" and showing selected geometrical variables . . . . .	101
4-2.	Sketch depicting a radial bend and pertinent geometrical variables. . . . .	107
4-3.	Sketch depicting a section of rectangular waveguide containing a ferrite waveguide slab whose height equals the waveguide height. . . . .	109
4-4.	Sketch depicting a section of rectangular waveguide containing a ferrite slab whose two transverse dimensions are less than the corresponding dimensions of the waveguide. . . . .	110
4-5.	Sketch depicting a side view of a coax-to-waveguide adapter and showing selected geometrical variables .	112
5-1.	Diagram of the antenna/obstacle geometry and the plane wave spectra used in the scattering analysis .	121
5-2.	Radiated pulse envelope in the antenna boresight direction for the unobstructed 4.0-foot diameter reflector antenna for an input 2.0-nanosecond rectangular pulse with carrier frequency at the in-band frequency of 3.0 GHz . . . . .	132
5-3.	Radiated pulse envelope in the boresight direction for the 4.0-foot diameter reflector antenna partially blocked by a 2.0-foot diameter cylinder located 6.0 feet away along the 5.0-degree radial for an input 2.0-nanosecond rectangular pulse with carrier frequency at the in-band frequency of 3.0 GHz. . . .	133

## LIST OF FIGURES

<u>Figure</u>	<u>Page</u>
5-4. Radiated pulse envelope in the antenna boresight direction for the unobstructed 4.0-foot diameter reflector antenna for an input 2.0-nanosecond rectangular pulse with carrier frequency at the out-of-band frequency of 6.5 GHz. . . . .	134
5-5. Radiated pulse envelope in the boresight direction for the 4.0-foot diameter reflector antenna partially blocked by a 2.0-foot diameter cylinder located 6.0 feet away along the 5.0-degree radial for an input 2.0-nanosecond rectangular pulse with carrier frequency at the out-of-band frequency of 6.5 GHz. .	135
5-6. Radiated pulse envelope at 6.0 degrees off the antenna boresight direction for the unobstructed 4.0-foot diameter reflector antenna for an input 2.0-nanosecond rectangular pulse with carrier frequency at the out-of-band frequency of 6.5 GHz. .	136
5-7. Radiated pulse envelope at 6.0 degrees off the antenna boresight direction for the 4.0-foot diameter reflector antenna partially blocked by a 2.0-foot diameter cylinder located 6.0 feet away along the 5.0-degree radial for an input 2.0-nanosecond rectangular pulse with carrier frequency at the out-of-band frequency of 6.5 GHz. .	137

# LIST OF TABLES

<u>Table</u>		<u>Page</u>
2-1.	THE 9X9 MATRIX ARISING IN THE SOLUTION OF THE NEAR-FIELD COVARIANCE FUNCTIONS FOR A WIRE ARRAY CONSISTING OF 3 RADIATING ELEMENTS . . . . .	43
4-1.	MODAL POWER FLOW FOR THE $TM_{nm}^y$ MODES FOR THE INDICATED FREQUENCIES FOR WR-284 WAVEGUIDE EXCITED BY AN IDEALIZED COAX-TO-WAVEGUIDE ADAPTER HAVING A FILAMENTARY CURRENT PROBE . . . . .	118

## SECTION I

### INTRODUCTION

The progress and results achieved on this basic research program are summarized herein. The purpose of the research program is to study the application of near-field techniques to characterize the radiation and coupling characteristics of wideband CW or pulsed radiators. Out-of-band as well as in-band situations are of interest and both situations are included in the study.

The radiation pattern of an antenna can, in principle, be calculated by conventional deterministic analysis based on a knowledge of all system variables. The feed network, however, can support multi-mode energy propagation at out-of-band frequencies. For example, energy can be propagated in the 18 different modes delineated in Figure 1-1 in standard WR-284 S-band waveguide at the out-of-band frequency of 10.0 GHz. Furthermore, all of the modes whose second index is non-zero have an electric field component polarized orthogonal to the dominant in-band  $TE_{10}$  mode. The electric fields for the first 5 modes are depicted schematically in Figure 1-2.

Calculation of the relative phases and amplitudes of the different modes requires a detailed knowledge of the feed network. This is generally a very difficult boundary value problem. Further, the coefficients of the modes will be quite sensitive to minor electrical and mechanical variations in the feed network, especially those containing active devices, so that nominally identical systems can produce distinctly different out-of-band patterns. This characteristic out-of-band pattern sensitivity is evident from experimental and theoretical studies [1-7]. In order to account for these seemingly random effects, the out-of-band mode excitation coefficients may be treated as random variables. Treatment of these modal coefficients as random variables serves a dual purpose. First, it allows the analysis of radiation patterns to proceed independent of the feed structure (which may vary between otherwise identical antennas). Second, it leads to statistical equations that can account for variations in fabrication and excitation of the nominal antenna.

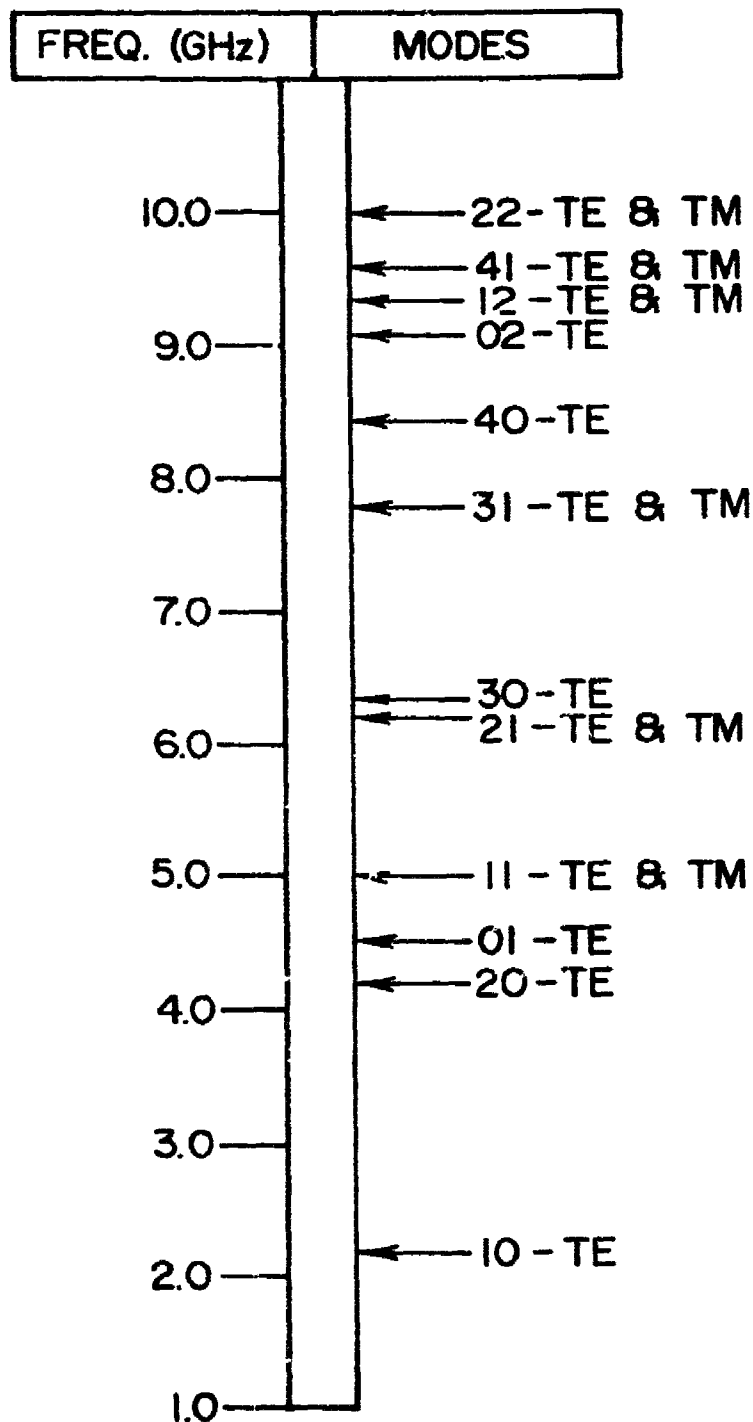
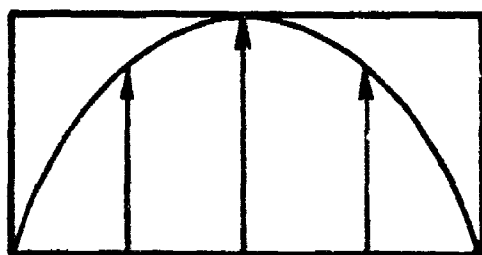
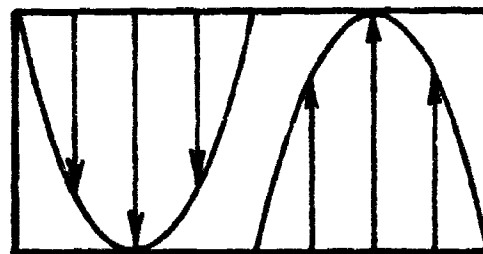


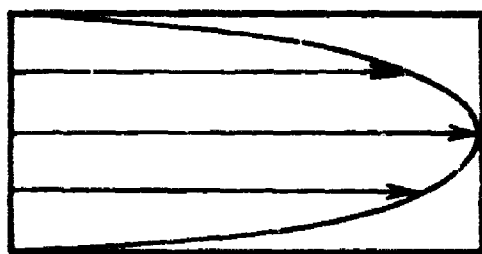
Figure 1-1. Diagram depicting the allowed higher order modes versus frequency for WK-284 S-band rectangular waveguide.



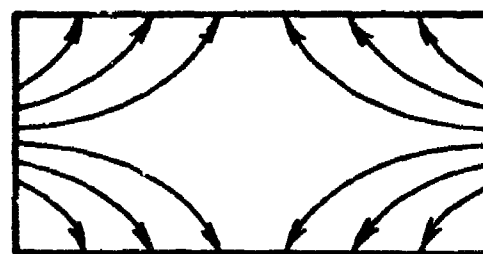
(a)  $TE_{10}$  MODE



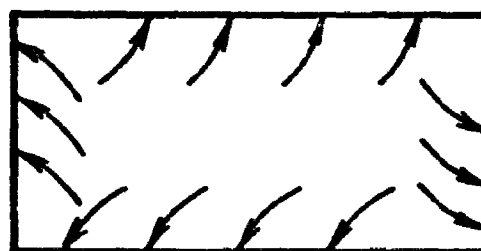
(b)  $TE_{20}$  MODE



(c)  $TE_{01}$  MODE



(d)  $TE_{11}$  MODE



(e)  $TM_{11}$  MODE



Figure 1-2. Sketches depicting the transverse electric field for the indicated higher-order modes in rectangular waveguide.



Consequently, statistical analysis techniques are needed for out-of-band characterization since it is impractical, or perhaps impossible, to solve the electromagnetic boundary value problems for the myriad reflector and phased array feed systems encountered in practice. Statistical techniques and concepts can also be employed to provide succinct EMC descriptions of essentially "deterministic" in-band wideband or pulsed radiators. Consequently, a considerable effort has been devoted to statistical characterization of wideband radiators.

The research program is divided into four major tasks. The four tasks are as follows.

Task 1. Provide a near-field methodology to characterize electromagnetic emitter radiation patterns at in-band and out-of-band frequencies for wide bandwidth radiators. The objective of this task is to develop the appropriate theory and equations based on statistical analysis techniques for efficient characterization of wideband radiators.

The objective of Task 1 was achieved via the following accomplishments:

- (a) The theory and equations were developed for both in-band and out-of-band frequencies for deriving statistical average far-field patterns from wide-band or pulsed near-field measurements.
- (b) Based upon the theoretical studies, methods of efficiently characterizing both wideband continuous-wave and pulsed radiators using near-field measurement techniques were devised.
- (c) Based upon the theoretical studies, a numerical simulation which is applicable to various antenna types, such as reflector and phased-array antennas was performed to demonstrate that valid statistical far-field pattern distributions can be obtained from near-field measurements.

Task 2. Theoretically relate the radiation pattern characterization to the basic data needed for efficient optimization analysis of electromagnetic spectrum usage. The objective of this task is to relate the near-field derived wideband antenna characterization to antenna coupling of antenna systems which co-exist in the same EM

environment. This objective was achieved by the following accomplishments:

- (a) The theory and equations were developed for analyzing the coupling between co-sited transmitting and receiving systems for combinations of wideband transmitting antennas, narrowband-harmonic transmitting antennas, and both wideband and narrowband-harmonic receiving antennas.
- (b) Based upon the theoretical studies, the near-field derived data required for efficient EM spectrum usage optimization were defined and employed in numerical simulations to demonstrate application to EM spectrum usage analysis.

Task 3. Provide the methodology to assess the effects of system devices (i.e., higher-order mode generation) on the radiation pattern.

The objectives of this task are (1) to determine a method whereby the pattern effects of higher-order modes which are generated by system devices at out-of-band frequencies can be assessed and (2) to study the feasibility of identifying the modal content of an out-of-band feed system from measured data. These objectives were achieved by the following accomplishments.

- (a) Equations were derived during Task 1 and Task 2 to permit the out-of-band radiation pattern statistics to be computed from a knowledge of the system device statistics which describe the higher-order mode generation and propagation.
- (b) Theory and equations for identifying the higher-order mode statistics of system devices through utilization of wideband or pulsed near-field measurements were derived.

Because the first objective for this task was essentially achieved as a result of the work on Tasks 1 and 2, the scope of the effort on this task was expanded to include a brief analytical study of the out-of-band characteristics of three common waveguide components. The three waveguide devices studied are (1) a coax-to-waveguide adapter, (2) radial bends, and (3) a ferrite phase shifter.

Task 4. Investigate the impact of site effects on the near-field antenna analysis technology.

The objective of this task is to extend the existing monochromatic spectrum scattering matrix analysis to study antenna siting effects on the wideband and out-of-band performance of radiating systems. This objective was achieved by the following accomplishments.

- (a) A theoretical study was performed to investigate techniques and derive the equations for extending the existing monochromatic spectrum scattering matrix theory to analyze site effects over wide frequency bandwidths.
- (b) Based upon the results of the theoretical study, a numerical simulation of the site effects on the wideband in-band and out-of-band performance of a radiating system was performed.

All of the objectives set forth in the task statements were successfully achieved. The salient results of the research work for each task are successively presented and discussed in Sections II through V. Most of the important results for Task 1 were previously presented in the Interim Technical Reports No. 1 and No. 2 [4,5]. Similarly, the main results for Task 2 were included in Interim Technical Report No. 2. Abbreviated versions of the previously reported results for Tasks 1 and 2 are contained in Section II and Section III, respectively, along with discussions of new or additional results. Results for Tasks 3 and 4 are contained in Sections IV and V, respectively. Conclusions and recommendations based on the entire research program are presented in Section VI.

SECTION II  
THEORY AND TECHNIQUES FOR WIDEBAND  
ANTENNA PATTERN CHARACTERIZATION

A. Introduction

The theory and equations were developed for characterizing the radiation patterns of wideband cw or pulsed antennas over both in-band and out-of-band frequency intervals from measured data collected via near-field measurement techniques. The results are applicable to either phased array or reflector antennas. Numerical simulations were performed for (1) a 20-element out-of-band waveguide phased array with no inter-element coupling and (2) 3-element and 9-element wire arrays with inter-element coupling. The effect of statistical correlations of the near-field data was studied and methods for handling correlation effects were derived. Useful approximations for the probability density function for the radiated power pattern statistics for correlated sources were also identified.

The key results obtained via the Task 1 efforts may be summarized as follows:

- (1) The statistical average patterns and standard deviations at selected frequencies can provide a very succinct engineering description of the important EMC characteristics of wideband CW multimoding antennas. The statistical average patterns and standard deviations are a practical alternative to the comparatively more expensive and cumbersome Monte Carlo simulations.
- (2) The statistical average pattern for a given frequency may be computed from a knowledge of the following near-field statistical parameters:
  - (a) statistical average value of the electric field at all near-field measurement points,
  - (b) the standard deviation of the electric field at all measurement points, and
  - (c) the covariance functions for the electric fields at all different near-field measurement points.
- (3) The statistical average pattern versus time for a pulsed system depends on all of the above near-field statistical parameters listed in Item 2, and the following far-field statistical parameters:

- (a) the statistical average value of the far-field electric field at all frequencies in the frequency band,
- (b) the standard deviation of the far-field electric field at all frequencies in the frequency band, and
- (c) the covariance functions of the electric field at all different frequencies in the frequency band.

However, the far-field statistical parameters listed above can be computed from the near-field statistical parameters. Thus, pulsed antennas characterization does not require knowledge of any additional statistical near-field data.

- (4) The probability density function (p.d.f.) for the far-field electric fields of correlated random sources or scatterers can be accurately approximated for most antenna or scattering problems via the use of Nakagami's p.d.f. and linear operator theory. A less accurate but relatively simple expression for the p.d.f. was also derived that is suitable for certain engineering applications.

These results imply that the fundamental technical requirement for employing near-field techniques to describe wideband CW or pulsed antenna radiation is that one be able to compute the statistical average far-field power pattern versus frequency from the measured near-field data. As stated in Item 2, this requires a knowledge of the average electric field and the standard deviation at each sample point and the covariance function at all different measurement points (cross-covariance). Only the cross-covariance function presents a significant measurement problem. The accuracy and feasibility of the near-field measurement technique for wideband out-of-band antennas depends on whether the covariance functions can be suitably determined. Accordingly, considerable effort was devoted to studying the covariance functions and their effect on accuracy, time and cost. The results of this effort are presented and discussed in subsection C. In particular, the theoretical and numerical analyses are presented for a linear array of wire elements. The theory and equations for a two dimensional array of wire elements involve no new concepts. Corresponding theoretical and numerical analyses of an array of multimoding out-of-band waveguide elements can also be performed by including intermodal correlations in the analysis.

## B. Frequency Domain Analysis

The analysis was conducted initially for the linear array of waveguide elements depicted in Figure 2-1. The array is assumed to be either pulsed or operated over a finite frequency band. The frequency spectrum is assumed to contain some components which can be propagated in higher-order mode field configurations in the waveguide elements. A convenient starting point in the analysis is to first write down the appropriate equations for a non-random antenna measurement situation. The analysis of randomly-excited antennas can then subsequently be conducted based on the initially deterministic equations and statistical analysis techniques.

### 1. Basic Equations

The electric field produced on the near-field measurement plane is written as the superposition of the radiation fields of the individual element radiators. It is assumed that the measurement plane is located at a distance  $x$  that is  $\geq$  the far-field distance of each element radiator. A transverse field component, say the vertically polarized component  $E_q(\omega)$ , produced at the measurement point  $q$  is then

$$E_q(\omega) = \sum_{\ell} \sum_{\kappa} a_{\ell}^{\kappa}(\omega) h_{\ell}^{\kappa}(\omega, \phi_{\ell q}) \frac{\exp \left[ -j \frac{\omega}{c} r_{\ell q} \right]}{r_{\ell q}}, \quad (2-1)$$

where  $c$  is the speed of light in vacuum,  $\omega = 2\pi f$ , and where

- $a_{\ell}^{\kappa}$  = complex mode coefficient for the  $\kappa^{\text{th}}$  mode in the  $\ell^{\text{th}}$  element,
- $h_{\ell}^{\kappa}$  = vertically polarized far-field electric field pattern of the  $\kappa^{\text{th}}$  mode of the  $\ell^{\text{th}}$  element,
- $\phi_{\ell q}$  = angular location of the  $q^{\text{th}}$  measurement point with respect to the center of the  $\ell^{\text{th}}$  element,
- $r_{\ell q}$  = magnitude of the radius vector from the center of the  $\ell^{\text{th}}$  element to the  $q^{\text{th}}$  measurement point.

The plots of amplitude and phase shown near the bottom of Figure 1 depict either (1) the electric field versus frequency as the array input signal is swept over a specified frequency band or (2) the complex frequency spectrum of a radiated pulse. In either case, different results would be obtained at different measurement points.

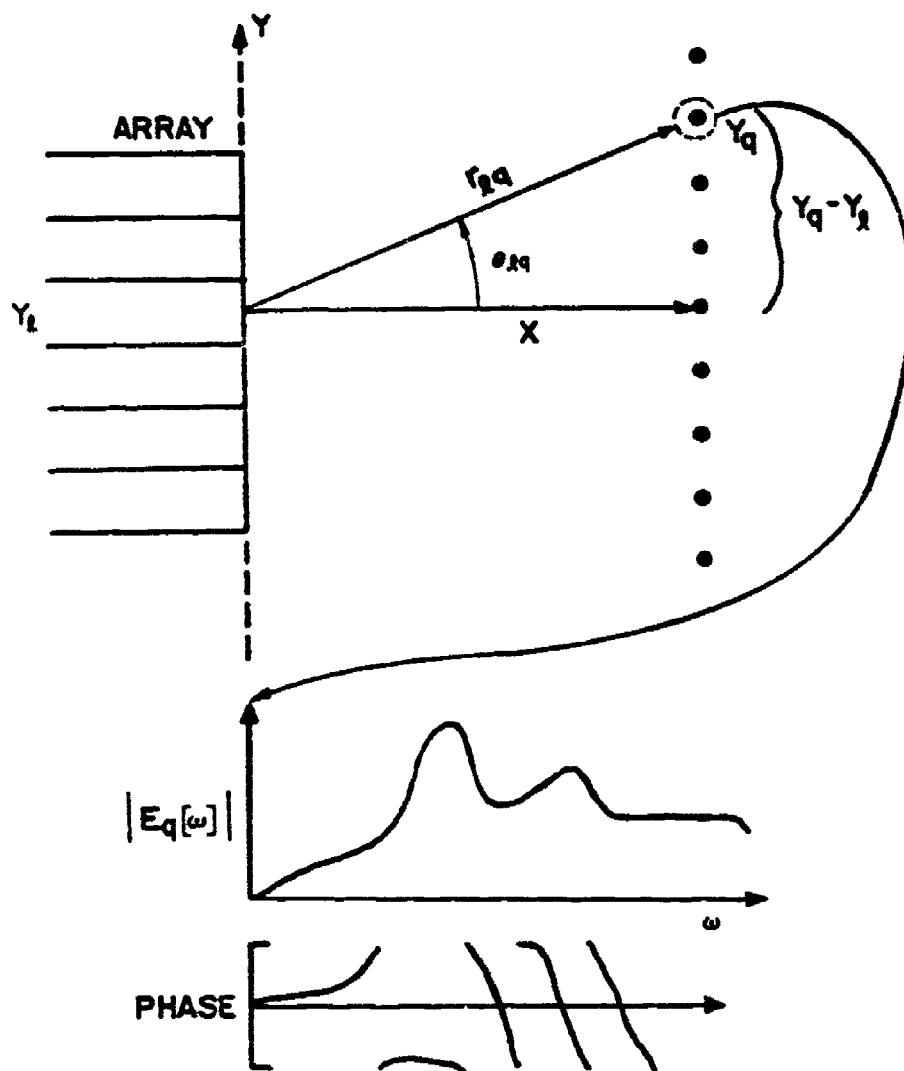


Figure 2-1. Sketch depicting a linear array of waveguide elements and hypothetical out-of-band amplitude and phase responses at a near-field measurement point.

The frequency spectrum of the time pulse is obtained via the Fourier transform of the pulse, which is

$$E_q(\omega) = \sum_n E_q(t_n) \exp \left[ -j\omega t_n \right] , \quad (2-2)$$

where  $E_q(t_n)$  is the time-domain response.

The far-field electric field is obtained as the discrete Fourier transform of the near-field electric field. Thus, the far-field electric field is given as

$$E(\omega, \phi) = \sum_q E_q(\omega) \exp \left[ -j \frac{\omega}{c} \sin(\phi) Y_q \right] , \quad (2-3)$$

where  $Y_q$  is the y-coordinate of the  $q^{\text{th}}$  measurement point,  $\phi$  is the azimuth angle of the far-field observation point, and where  $E_q$  is a previously defined by Equation (2-1). A factor  $(1/r)$ , where  $r$  is the distance from the center of the measurement plane to the far-field observation point, has been suppressed in Equation (2-3) and subsequent equations.

The power density in the far-field of the antenna is obtained by multiplying Equation (2-3) by its complex conjugate. The resulting equation for the power density  $P(\omega, \phi)$  is thence

$$P(\omega, \phi) \equiv E^*(\omega, \phi) E(\omega, \phi) = \sum_q \sum_{q'} E_{q'}^*(\omega) E_q(\omega) \exp \left[ j \frac{\omega}{c} \sin(\phi) (Y_{q'} - Y_q) \right] \quad (2-4)$$

Equations (2-1) through (2-4) are the well-known basic equations for analyzing deterministic (non-random) antenna patterns utilizing the frequency domain approach. The temporal (time) behavior of the electric field is obtained via the Fourier transform with respect to frequency. The corresponding analysis of a randomly-excited array antenna primarily involves the application of certain mathematical operations to these same equations, as described in the following paragraphs.

The plots shown in Figure 2-1 can be interpreted as representing the measured response obtained from one experiment involving a



randomly-excited antenna. Successive experiments would yield different responses. Consequently, a randomly excited antenna has many possible near-field distributions, spectral responses, and far-field patterns. Thus the amount of data required to characterize a randomly excited antenna will be much greater than the amount of data required for a comparable deterministic antenna unless a suitable statistical analysis can be devised to reduce the data requirements.

The statistical average value of the far-field power density is written as

$$\langle P(\omega, \phi) \rangle =$$

$$\sum_q \sum_q \langle E_q^*(\omega, \phi) E_q(\omega, \phi) \rangle \exp \left[ j \frac{\omega}{c} \sin(\phi) (Y_q - Y_q) \right],$$

(2-5)

where the angular brackets denote the statistical average value [8]. The angular brackets are shorthand notation for integrals of the type

$$\langle W(\chi) \rangle = \int \int_{\zeta_1 \dots \zeta_n} [W(\chi) | (\zeta_1 \dots \zeta_n)] f(\zeta_1 \dots \zeta_n) d\zeta_1 \dots d\zeta_n, \quad (2-6)$$

where  $\chi$  = a non-random variable,

$\zeta$  = random variables, and

$f(\zeta)$  = probability density for the random variables.

Similarly, the statistical average value of the (complex) electric field is

$$E(\omega, \phi) = \sum_q \langle E_q(\omega) \rangle \exp \left[ -j \frac{\omega}{c} \sin(\phi) Y_q \right]. \quad (2-7)$$

The electric field is, of course, a complex valued function and is therefore not an observable quantity. However, the statistical average

value and higher-order statistical moments are well defined quantities [5]. In particular, the statistical average value of the complex electric field  $E_q$  is defined as

$$\langle E_q(\omega) \rangle = \langle U_q(\omega) \rangle - j \langle V_q(\omega) \rangle . \quad (2-8)$$

where  $U_q$  and  $V_q$  denote the real and imaginary parts, respectively, of  $E_q$ .  $U_q$  and  $V_q$  are defined in the conventional manner as

$$U_q(\omega) = A_q(\omega) \cos [\alpha_q(\omega)] , \text{ and} \quad (2-9)$$

$$V_q(\omega) = A_q(\omega) \sin [\alpha_q(\omega)] , \quad (2-10)$$

where  $A_q(\omega)$  = relative amplitude (real number) of the electric field at  $q$ , and

$\alpha_q(\omega)$  = relative phase of the electric field at  $q$ .

Thus, a knowledge of the average values of the real and imaginary parts of the near-field electric field over the measurement plane permits the computation of the average far-field electric field as the Fourier transform of the average near-field electric field.

The average power density is related to the product  $\langle E^* \rangle \langle E \rangle$ , where the symbol  $*$  denotes complex conjugation, as

$$\langle P(\omega, \phi) \rangle = \langle E^*(\omega, \phi) \rangle \langle E(\omega, \phi) \rangle + C_{E^*, E}(\omega, \phi) . \quad (2-11)$$

The symbol  $C_{E^*, E}$  denotes the covariance function and is defined as

$$C_{E^*, E}(\omega, \phi) = \langle E^*(\omega, \phi) E(\omega, \phi) \rangle - \langle E^*(\omega, \phi) \rangle \langle E(\omega, \phi) \rangle \quad (2-12)$$

The equation for the far-field covariance function can be derived for the linear array via straightforward algebraic manipulations. The

resulting equation is

$$C_{E^*, E}(\omega, \phi) = \sum_q \gamma_q^2(\omega, \phi) + \sum_{\substack{q, q' \\ (q' \neq q)}} \gamma_{q'}(\omega) \gamma_q(\omega) R_{q', q}(\omega) \exp \left[ j \frac{\omega}{c} \sin(\omega) (Y_{q'} - Y_q) \right], \quad (2-13)$$

where  $\gamma_q$  denotes the standard deviation of the near-field electric field at  $q$  and  $R_{q', q}$  denotes the cross-correlation coefficient for the electric field at  $q$  and the conjugate of the electric field at  $q'$ .

The standard deviation  $\gamma_q$  is a real number and is equal to the square root of the sum of the variances of the real and imaginary parts of  $E_q$ . Accordingly,  $\gamma_q$  is written as

$$\gamma_q(\omega) = \sqrt{[\sigma_u(\omega)]_q^2 + [\sigma_v(\omega)]_q^2}, \quad (2-14)$$

where  $[\sigma_u(\omega)]_q$  = standard deviation of the real part of  $E_q$ , and  $[\sigma_v(\omega)]_q$  = standard deviation of the imaginary part of  $E_q$ .

The cross-correlation coefficients  $R_{q', q}$  are defined as the complex numbers obtained via the equation

$$R_{q', q}(\omega) = \frac{C_{q', q}(\omega)}{\gamma_{q'}(\omega) \gamma_q(\omega)}, \quad (2-15)$$

where the numerator of Equation (2-15) is referred to as the cross-covariance function. The cross-covariance of the electric fields at  $q$  and  $q'$  is

$$\begin{aligned}
C_{q,q}(\omega) = & \left\{ \left[ \langle U_{q,}(\omega) U_{q,}(\omega) \rangle - \langle U_{q,}(\omega) \rangle \langle U_{q,}(\omega) \rangle \right] \right. \\
& + \left[ \langle V_{q,}(\omega) V_{q,}(\omega) \rangle - \langle V_{q,}(\omega) \rangle \langle V_{q,}(\omega) \rangle \right] \Big\} \\
& + j \left\{ \left[ \langle V_{q,}(\omega) U_{q,}(\omega) \rangle - \langle V_{q,}(\omega) \rangle \langle U_{q,}(\omega) \rangle \right] \right. \\
& - \left. \left[ \langle U_{q,}(\omega) V_{q,}(\omega) \rangle - \langle U_{q,}(\omega) \rangle \langle V_{q,}(\omega) \rangle \right] \right\}.
\end{aligned} \tag{2-16}$$

The rigorous analysis of the far-field statistical average power pattern for a given frequency is seen from Equation (2-7) through (2-16) to require computation of the following near-field statistical quantities:

- (1) statistical average value of the real and imaginary parts of the near-field electric field at all measurement points,
- (2) the standard deviation of the real and imaginary parts of the near-field electric field at all measurement points, and
- (3) the cross-polarization coefficients of the near-field electric field at all different measurement points.

In a near-field measurement situation, the first two quantities can be determined by computing the "sample" average values and standard deviations obtained from repeated trials. The sample average value [8] of a random variable  $W$  is defined as

$$\langle W \rangle = \frac{1}{N} \sum_n W_n, \tag{2-17}$$

where  $W_n$  is the value of  $W$  obtained in the  $n^{\text{th}}$  trial, and  $N$  is the number of trials. Similarly, the sample standard deviation  $\sigma_W$  is defined as

$$\sigma_W = \sqrt{\frac{1}{N} \sum_n [W_n - \langle W \rangle]^2} \quad (2-18)$$

The extraction of the cross correlation data is not straightforward and this problem area is discussed in Part C.

## 2. Frequency-Averaged Statistical Average Antenna Patterns

The preceding discussions have addressed statistical averaging over randomly-varying variables. It may be meaningful to also average over frequency in some applications involving a CW radiating system of moderate bandwidth. The purpose of averaging over frequency is to obtain a single average pattern plus standard deviation that adequately describes the general radiation characteristics of the antenna. The single average pattern plus standard deviation replaces the large collection of patterns versus frequency that would otherwise be needed to characterize the antenna.

Two different methods for obtaining the frequency-averaged statistical pattern have been formulated. The most direct method for obtaining the frequency-averaged statistical average pattern is to first compute the statistical average pattern at selected frequencies and then arithmetically average the statistical average patterns. This process is described mathematically as

$$\langle\langle P(\omega, \phi) \rangle\rangle_\omega = \frac{1}{N} \sum_n P(\omega_n, \phi) \quad , \quad (2-19)$$

where N is the total number of selected frequencies and where frequency averaging is denoted by subscript  $\omega$  on the outermost right-hand angular bracket. It is also possible to obtain the frequency-averaged statistical average pattern by first computing the deterministic frequency average and then computing the statistical average. This process is described mathematically as

$$\langle\langle P(\omega, \phi) \rangle\rangle_\omega = \sum_q \sum_q \langle D_{q,q} \rangle \exp[-jd_{q,q}\omega] \quad (2-20)$$

where

$$d_{q,q} = \frac{\sin(\phi)}{c} (Y_{q'} - Y_q), \text{ and} \quad (2-21)$$

$$\langle D_{q,q} \rangle = \frac{1}{2\pi N} \sum_{q'} \sum_q \langle E_{q'}^*(\omega_n, \phi) E_q(\omega_n) \rangle \exp[jd_{q,q} \omega_n] . \quad (2-22)$$

The amount of computational labor required to compute frequency-average statistical average patterns is roughly equivalent for the two methods.

The out-of-band radiation patterns of a 20-element multimoding array were studied numerically via both direct Monte Carlo simulations and Equations (2-1) through (2-19). For this array, whose in-band design frequency is 9.0 GHz, Monte Carlo patterns as well as the statistical average patterns and standard deviations were computed for selected frequencies up to 19 GHz for various in-band scan conditions. Experimentally-derived out-of-band phase shift and attenuation statistical parameters for a waveguide element containing a ferrite phase shifter were used as inputs. Accordingly, the modal phase variations follow a Gaussian distribution and the modal power variations follow a uniform distribution to good approximation.

It was found that for small in-band scan angles the statistical average pattern and standard deviation at frequencies of 14 GHz, 15.7 GHz, and 18 GHz could provide a good EMC description of the radiation characteristics over portions of the frequency band for which energy can propagate in the first two modes, the first three modes, and the first five modes, respectively. Figure 2-2 shows the calculated average pattern and standard deviation at 18 GHz for broadside scan superimposed on calculated Monte Carlo patterns for 16-19 GHz region for the cross polarized component of the radiated power for propagation in the first 5 waveguide modes. For in-band scan angles of about 30 degrees or more, a better EMC description is obtained by including at

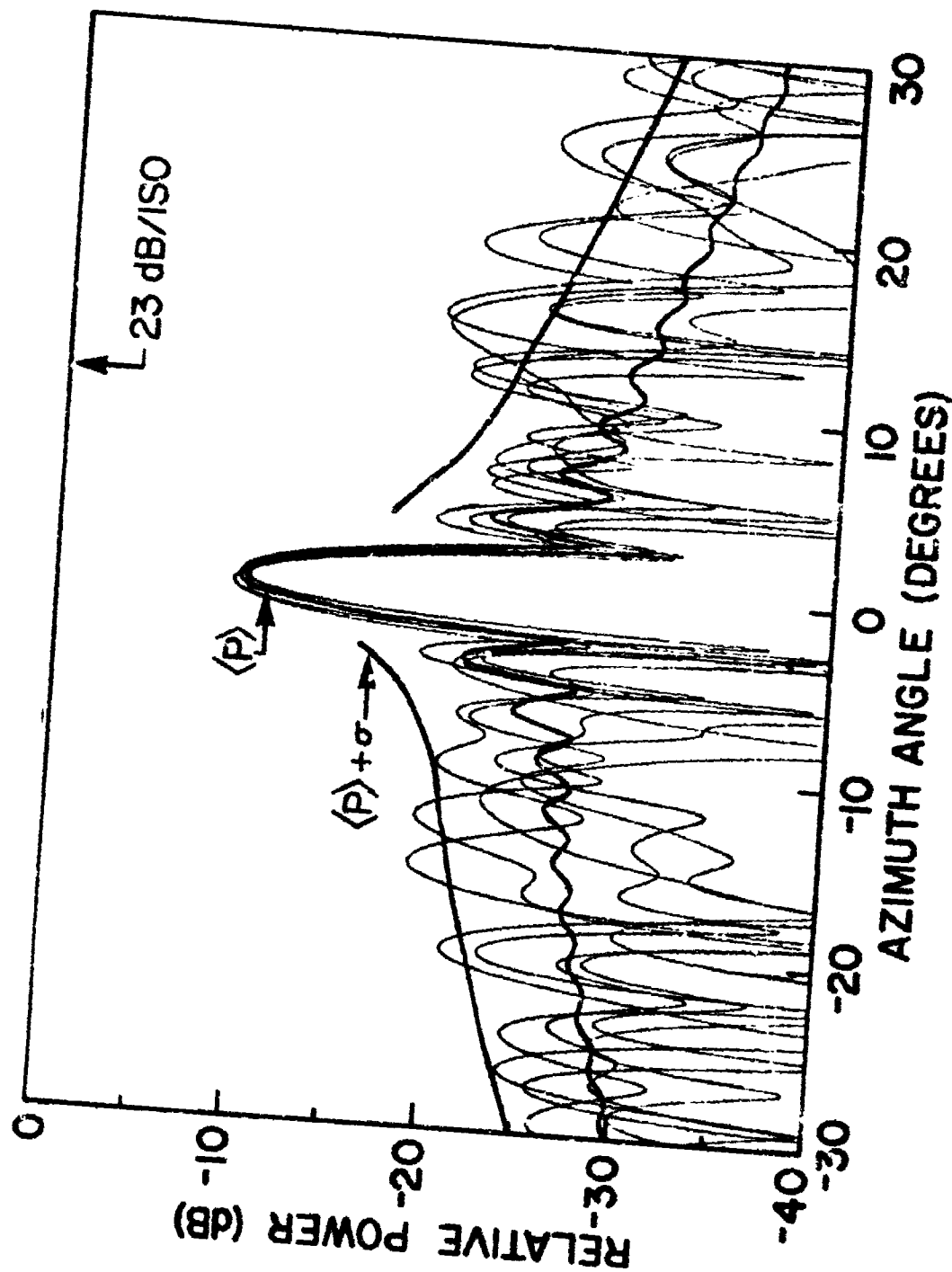


Figure 2-2. Out-of-band antenna patterns for a randomly-excited 20-element array of multimoding waveguide elements for the cross polarization sense for statistical average power flow of 0.2 watt each in the  $TE_{20}$ ,  $TE_{01}$ ,  $TE_{11}$  and  $TM_{11}$  waveguide modes.

least the statistical average patterns for frequencies near the edges of the frequency sub-interval because the patterns at different out-of-band frequencies scan through unequal amounts for a given in-band scan angle [9]. The spatial regions corresponding to the superimposed main beams and grating lobes clearly delineate areas of particular concern in EMC applications.

The statistical average patterns and standard deviations at selected frequencies can provide a very succinct engineering description of the important EMC characteristics of wideband CW multimoding antennas. The statistical average patterns and standard deviations are a practical alternative to the comparatively more expensive and cumbersome Monte Carlo simulations.

### 3. Reduction of Data Measurement Requirements

A reduction in the near-field data measurement requirements can be achieved at the expense of a nominal reduction in the accuracy of the far-field pattern details. Specifically, reducing the amount of measured data either by increasing sample spacing or by truncating the size of the transverse measurement plane will generally cause errors in the calculated far-field patterns. The magnitude of the far-field pattern errors is a function of the sample spacing, the relative power level at the edges of the truncated near-field measurement plane, and the accuracy of the measured amplitude and phase recorded at each sample point [10]. The effects of number of sample points and phase measurement accuracy on the calculated far-field power pattern levels is displayed in Figure 2-3. The effect of the number of sample points on the beam pointing error are displayed in Figure 2-4 for a specified phase measurement error. It was assumed that the relative power at the edges of the measurement plane is -25 dB with respect to the highest recorded near-field amplitude. The analysis and equations employed to obtain these results are summarized in Reference [10].

Figure 2-3 is a plot of the error in the calculated far-field power pattern versus the "no-error" power pattern level for an R.M.S. wave measurement error of 5.0 degree for sample spacings of  $1\lambda$  and  $2\lambda$ , where  $\lambda$  is the operating wavelength. The "no-error" power pattern



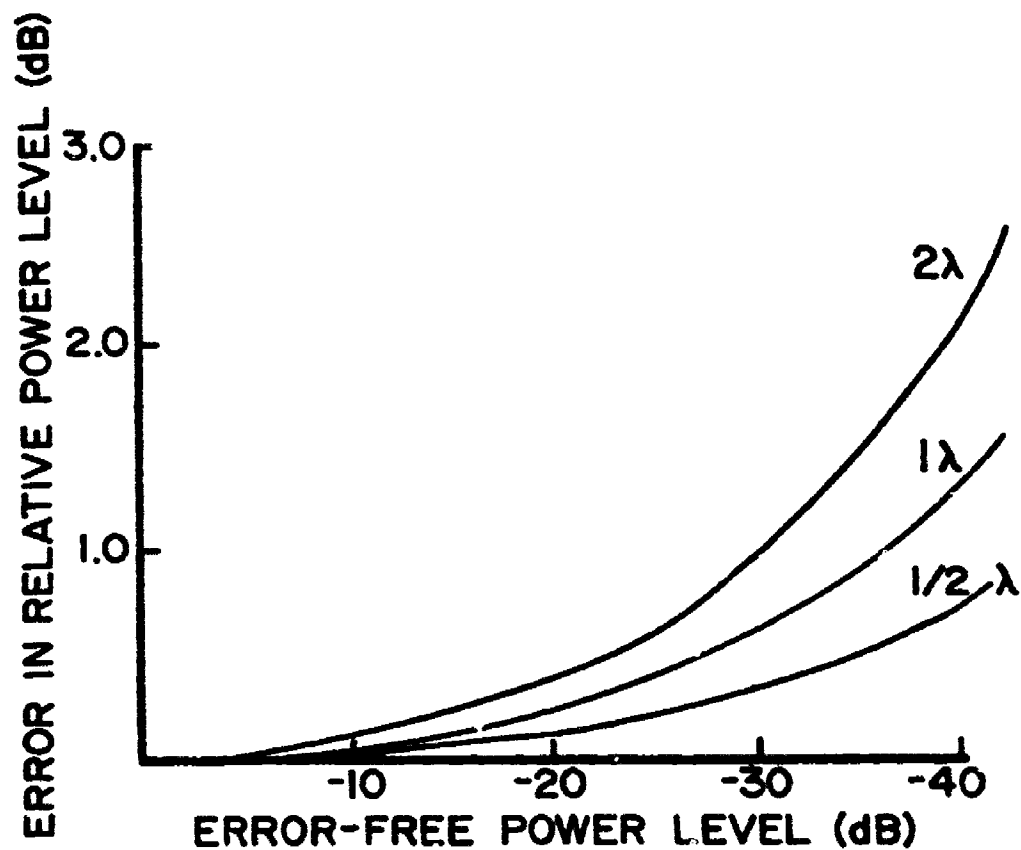


Figure 2-3. Error in the relative power level versus the nominal error-free power level for the indicated near-field measurement sample spacings for a 5.0 degree RMS phase measurement error.

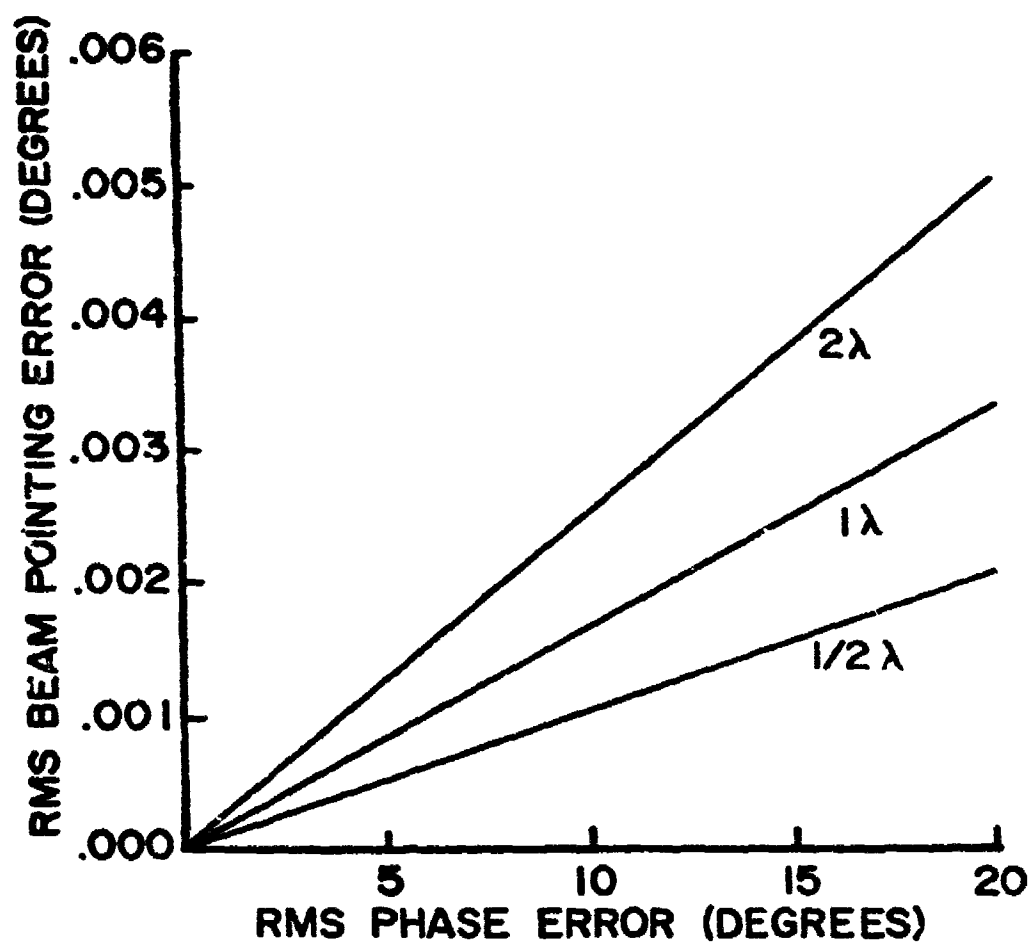


Figure 2-4. RMS beam pointing error as a function of RMS phase error for an antenna whose 3-dB beamwidth is nominally 0.5 degrees for the indicated sample spacings.

level along the abscissa is the power pattern level calculated from  $\lambda/2$  spacing for a near-field measurement plane which extends to the -40 dB level. Figure 2-4 is a plot of pointing error versus R.M.S. phase measurement error for sample spacings of  $\lambda/2$ ,  $1\lambda$ , and  $2\lambda$ .

Clearly, the accuracy of the calculated power pattern is degraded by large sample spacings, truncated measurement planes, and near-field measurement errors. It is also true that smaller near-field measurement errors permit the use of larger sample spacings and/or more severely truncated measurement planes. Of course, the advantages of reduced data recording requirements must be weighed against the accuracy requirements for the antenna under test. However, it appears that substantial reductions can be achieved for many engineering applications where the main interest is in obtaining valid estimates of mainbeam and grating lobe power levels and pointing directions and where moderate over-estimates of the average sidelobe level are acceptable.

#### C. Near-Field Covariance Study

The fact that the electric fields at different near-field sample points are correlated has an effect on the measurement time, accuracy and cost which can be appreciated by considering two different measurements using a single probe to measure a wideband phased array antenna. The two measurement schemes will be denoted for convenience as Method I and Method II.

In Method I, data are recorded as the probe is moved over the measurement plane in a raster scan. The operating frequency and array scan condition are assumed to be constant while the probe scans the entire measurement plane. This takes about two hours of elapsed time. The probe is then returned to its starting point, and the array phase shifters are "cycled" and returned to the initial scan condition. Data are recorded at the same frequency as the probe again traverses the measurement plane. This sequence of events is repeated, say, 50 times for a given frequency and array scan condition. The total measurement time required to record data for 100 frequencies and 30 array scan conditions is about 300,000 hours. The measurement time is clearly excessive. Additionally, it is very unlikely that an out-of-band array

antenna under test can be kept stable, i.e., no variation in modal content in any element, for the two-hours needed to record data for each selected out-of-band frequency and array scan condition. However, if the array element signals could be kept stable the near-field covariance functions could be computed directly from the measured data.

In Method II, the probe is held stationary at a preselected sample point while the signal source is scanned through the entire frequency spectrum of interest for a given array scan condition. The phase shifters are then cycled and returned to the selected scan condition. This procedure is repeated 50 times. A new scan condition is selected and the foregoing sequence of events is repeated. Finally, the entire sequence of events is repeated for all of the preselected sample measurement points on the near-field plane. Total measurement time for 100 frequencies and 30 array scan conditions is estimated to be about 120 hours. This measurement time is reasonable for a thorough characterization of a randomly-excited, out-of-band, wide-band phased array antenna. The average value and standard deviation of the electric field at each near-field sample point can be computed directly from the recorded data for each frequency and scan condition. However, the covariance function for the electric fields at different near-field sample points is more difficult to extract from the recorded data.

The covariance functions for the near-field electric field of a given array can be computed in a straightforward manner in terms of the covariance function for the electric fields on the array aperture. Of course, the aperture covariance function is not known in practice. If it were known, there would be no need for near-field measurements. However, an analysis of a specified array antenna can be used to study the general nature of the near-field covariance functions and their impact on the accuracy of the far-field average power pattern calculations. Furthermore, near-field covariance functions computed in this manner provide baseline data that can be used to check the validity and accuracy of near-field covariance functions obtained from analysis of simulated measured data obtained from a simulated Method II measurement. Accordingly, the near-field covariance functions for a

linear array of wire dipoles have been studied analytically and numerically. A corresponding study for an array of multimoding waveguide elements would be beneficial but is beyond the scope of the current efforts.

### 1. Analysis of Wire Array

The linear array of vertically-oriented, center-fed wire elements shown in Figure 2-5 is analyzed in the following paragraphs. It is assumed in the analysis that each element is fed by a constant voltage source.

The electric field  $E_q$  at measurement point  $q$  on the line defined by  $Z=0$ ,  $X=X_0$  is  $Z$ -directed and may be written as

$$E_q = C_0 \times \sum_{\ell} I_{\ell} \frac{\exp[-jk\sqrt{X_0^2 + (Y_q - Y_{\ell})^2}]}{\sqrt{X_0^2 + (Y_q - Y_{\ell})^2}} \quad (2-23)$$

where

$I_{\ell}$  = complex current at the current amplitude maximum on the  $\ell^{\text{th}}$  element,

$Y_q$  = the  $Y$  coordinate of the  $q^{\text{th}}$  measurement sample point,

$Y_{\ell}$  = the  $Y$  coordinate of the  $\ell^{\text{th}}$  element,

$k = 2\pi/\lambda$  where  $\lambda$  is the wavelength, and

$$C_0 = \frac{j\omega\mu}{4\pi} \int_{-h/2}^{+h/2} \zeta(z') e^{-jk_z z'} dz'.$$

The integral appearing in the definition of  $C_0$  is the same for each element at a given frequency and is just the Fourier Transform of the current distribution  $\zeta(z')$  along the length of the element, where  $\zeta(z')$  is normalized to have a maximum amplitude of 1.0.  $C_0$  will be suppressed in most of the remaining equations.

The statistical average far-field power density  $P(\phi)$  at azimuth angle  $\phi$  can be computed as previously stated, to wit:

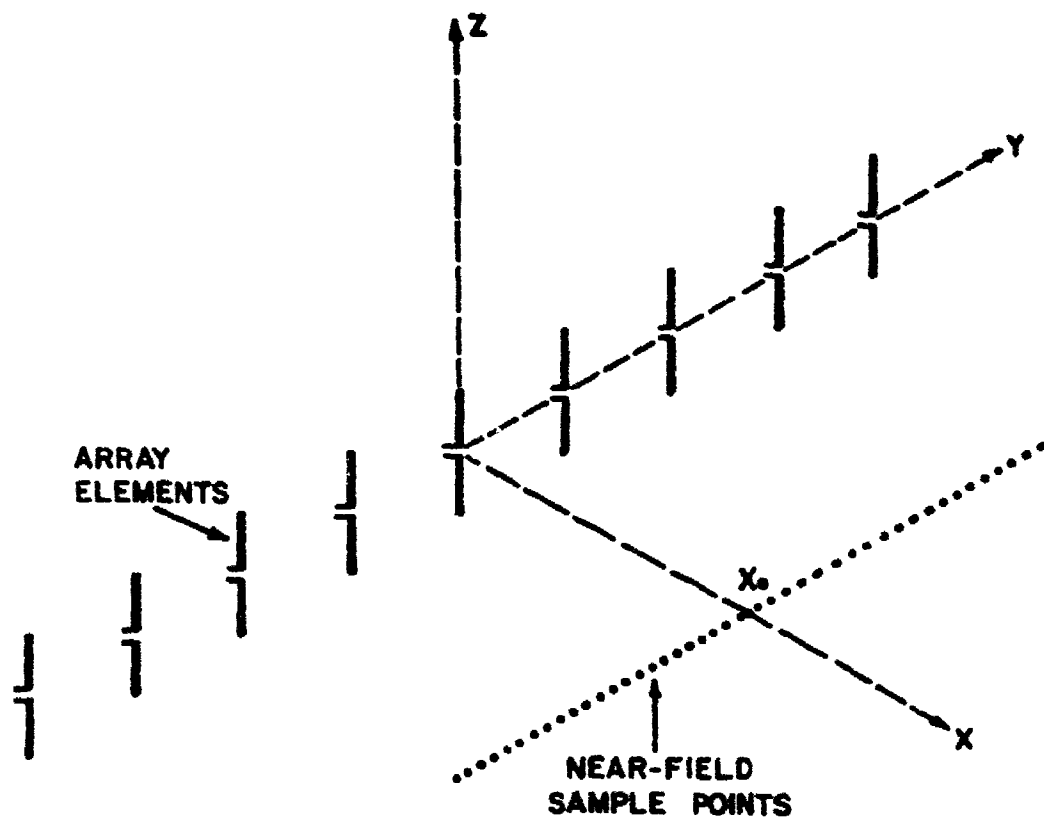


Figure 2-5. Sketch of an array of center-fed wire elements and near-field sample points.

$$\langle P(\phi) \rangle = \langle E^*(\phi) \rangle \langle E(\phi) \rangle + \sum_{q, \ell} C_{q'q} \exp [ (jk \sin \phi) (Y_{q'} - Y_q) ] \quad (2-24)$$

where  $\langle E(\phi) \rangle$  is the Fourier Transform of the average near-field electric field,  $\langle E^*(\phi) \rangle$  is its complex conjugate, and  $C_{q'q}$  is the near-field covariance function defined as

$$C_{q'q} = \langle E_{q'}^* E_q \rangle - \langle E_{q'}^* \rangle \langle E_q \rangle \quad (2-25)$$

where the symbol \* denotes complex conjugation.

The near-field covariance function  $C_{q'q}$  obtained from Equations (2-23) and (2-25) is then explicitly computed as

$$C_{q'q} = \sum_{\ell, \ell'} C_{\ell'\ell} G_{\ell'q}^* G_{\ell q} \quad (2-26)$$

where

$C_{\ell'\ell}$  = the covariance function for the current on element  $\ell$  and the conjugate of the current on element  $\ell'$ , and

$$G_{\ell'q}^* G_{\ell q} = \frac{\exp \left\{ jk_o \left[ \sqrt{x_o^2 + (Y_{q'} - Y_{\ell'})^2} - \sqrt{x_o^2 + (Y_q - Y_\ell)^2} \right] \right\}}{\sqrt{x_o^2 + (Y_{q'} - Y_{\ell'})^2} \sqrt{x_o^2 + (Y_q - Y_\ell)^2}} \quad (2-27)$$

The current covariance function  $C_{\ell'\ell}$  is by definition

$$C_{\ell'\ell} = \langle I_{\ell'}^* I_\ell \rangle - \langle I_{\ell'}^* \rangle \langle I_\ell \rangle \quad (2-28)$$

Equations (2-26) and (2-28) express the fact that the near-field covariance function can be computed from the current covariance function.

The current covariance function  $C_{l,l}$  is a function of the mutual admittance matrix for the array and the statistical parameters of the input voltage sources. In particular, the current at the  $l^{\text{th}}$  element is computed as

$$I_l = \sum_k \Gamma_{lk} V_k \quad (2-29)$$

where

$\Gamma_{lk}$  = elements of the complex admittance matrix [11], and  
 $V_k$  = complex voltage of the  $k^{\text{th}}$  voltage source.

It follows then that  $C_{l',l}$  is computed as

$$C_{l',l} = \sum_{k'} \sum_k \Gamma_{l'k'} \Gamma_{lk} C_{k',k} \quad (2-30)$$

where  $C_{k',k}$  is the voltage covariance function.

The current covariance function has zero magnitude in two different special cases. First, the current covariance function is zero when all of the voltage covariance functions are zero. This occurs when the voltages are deterministic (non-random). The currents are then perfectly correlated with correlation coefficient  $R_{l',l} = 1.0$  as can be discerned from the equation

$$R_{l',l} = \frac{C_{l',l}}{\xi_l^* \xi_l} \quad (2-31)$$

where  $\xi_l$  = standard deviation of the complex current, by taking the limit as the numerator and denominator approach zero. Second, the current covariance function for  $l \neq l'$  is zero when, simultaneously, the voltages are uncorrelated and the mutual coupling between current elements is zero. In this case the voltage covariance  $C_{k',k} = \delta_{k',k} (\gamma_v^2)_k$  and  $\Gamma_{lk} = \delta_{lk} \Gamma_l$ , i.e., the voltage covariance matrix and the



mutual admittance matrix both contain non-zero matrix elements only along the diagonal. This second case, where  $C_{l'l} = 0$  for  $l \neq l'$ , corresponds to the situation where the currents on different elements are uncorrelated and hence  $C_{l'l} = \delta_{l'l} \xi_l^2$ .

It will be assumed in the rest of the analysis that the voltage sources are statistically independent and are therefore uncorrelated. The behavior of the near-field covariance function will be examined for the case involving isolated current elements ( $\Gamma_{lk} = \delta_{lk} \Gamma_l$ ) and the case involving mutual coupling among the current elements.

The near-field covariance function may be written as

$$C_{q'q} = \sum_l |\Gamma_{ll}|^2 (\gamma_v^2)_l G_{lq}^* G_{lq} + \sum_{\substack{l, l' \\ (l' \neq l)}} \sum_k \Gamma_{l'k}^* \Gamma_{lk} (\gamma_v^2)_k (1 - \delta_{l'k} \delta_{lk}) G_{l'q}^* G_{lq} \quad (2-32)$$

for the realistic situation when the currents are coupled and as

$$C_{q'q} = \sum_l |\Gamma_{ll}|^2 (\gamma_v^2)_l G_{lq}^* G_{lq} \quad (2-33)$$

when the element currents are not coupled. Equation (2-33) is obtained from Equation (2-32) by setting  $\Gamma_{lk}^* \Gamma_{lk} = \delta_{lk} \delta_{lk}$  so that the off-diagonal elements of the mutual admittance matrix are zero. Equation (2-33) shows that the near-field covariance function is non-zero even if the near-field electric field is produced by isolated, statistically independent currents. This covariance will be denoted for convenience as intrinsic covariance. It is always present in stochastic antenna problems. Equation (2-32) shows that the total near-field covariance function in the realistic situation involving coupled radiating elements consists of two components, namely the intrinsic covariance and a second component denoted herein as the interactive covariance. The interactive covariance is present only when the radiating elements "interact", i.e., are electromagnetically coupled. A third component of the near-field covariance function, denoted as the intra-element

covariance, occurs for multimoding waveguide antennas due to correlation among the modes propagating within each separate waveguide element proper. This covariance contribution is absent for the wire array under consideration.

It should be noted that the near-field covariance function for the wire array given by Equation (2-32) is scan-invariant. This result follows from the fact that the mutual admittances are scan-invariant. Of course, the statistical average amplitudes and relative phases of the electric field at each sample point do change with scan angle. The near-field covariance functions for a multimoding out-of-band waveguide array may change with scan angle due to changes in average mode excitations with scan angle.

## 2. Numerical Study of Wire Array

Numerical simulations were conducted to study both the near-field and far-field radiation characteristics of a linear array of nine center-fed wire elements. The array elements have length  $\lambda_0/2$ , where  $\lambda_0$  is the free-space wavelength at the design in-band frequency of 3.0 GHz, and are spaced  $\lambda_0/2$  apart along the y axis. Each wire element is assumed to be fed by a constant amplitude voltage source, and each source is assumed to be matched to a 50-Ohm at both in-band and out-of-band frequencies.

The following data were computed for an array of coupled elements and an array of "isolated" elements for both the in-band frequency of 3.0 GHz and the out-of-band frequency of 9.0 GHz:

- (1) Non-random (deterministic) near-field power distributions and far-field power patterns,
- (2) Random (Monte Carlo) near-field power distributions and far-field power patterns,
- (3) Analytical statistical average near-field power distribution and analytical statistical average far-field power pattern,
- (4) Numerical average far-field pattern and its associated standard deviation based on 50 Monte Carlo random far-field patterns, and
- (5) Near-field covariance functions.

The data for Items (1) through (4) were computed for in-band scan-angles of zero degrees and 30 degrees. The near-field covariance functions for the wire array are scan-invariant and, hence, they were explicitly computed only for the broadside (zero-degree) scan condition.

The near-field covariance functions and their effects on the statistical average power patterns are the topics of paramount interest and only these data will be presented and discussed herein. A sketch of the simulated near-field measurement situation is shown in Figure 2-6. The near-field data were computed for 65 sample points centered on the near-field sample line. The near-field sample line was chosen to be  $8\lambda$  wide and is located  $2\lambda$  from the array.

The key results of the numerical studies can be summarized with the aid of the data plotted in the group of Figures 2-7 through 2-10 for the in-band frequency of 3.0 GHz and the group of Figures 2-11 through 2-14 for the out-of-band frequency of 9.0 GHz. The data are sequenced in the same order within each group. The first figure in each group is a plot of the near-field power distribution for deterministic (non-random) excitation of an array of coupled current elements for broadside scan. This plot is followed by plots of the scan-invariant, near-field statistical covariance functions and plots of the corresponding statistical average far-field power patterns for broadside scan. The statistical data in each figure are displayed for interacting (coupled) array elements and non-interacting (isolated) array elements by the plots labeled B and A, respectively. All of the near-field plots in Figures 2-7 through 2-14 are normalized with respect to the peak magnitude of the non-random, in-band, near-field power distribution shown in Figure 2-7.

The general behavior of the near-field covariance functions may be discerned from Figures 2-8 and 2-9 for the in-band frequency and Figures 2-12 and 2-13 for the out-of-band frequency. The covariance functions for the center sample point with all other points are symmetric about the center point, while the covariance functions for a sample point opposite the edge of the array with all other sample points are asymmetrical. This behavior is expected because the array

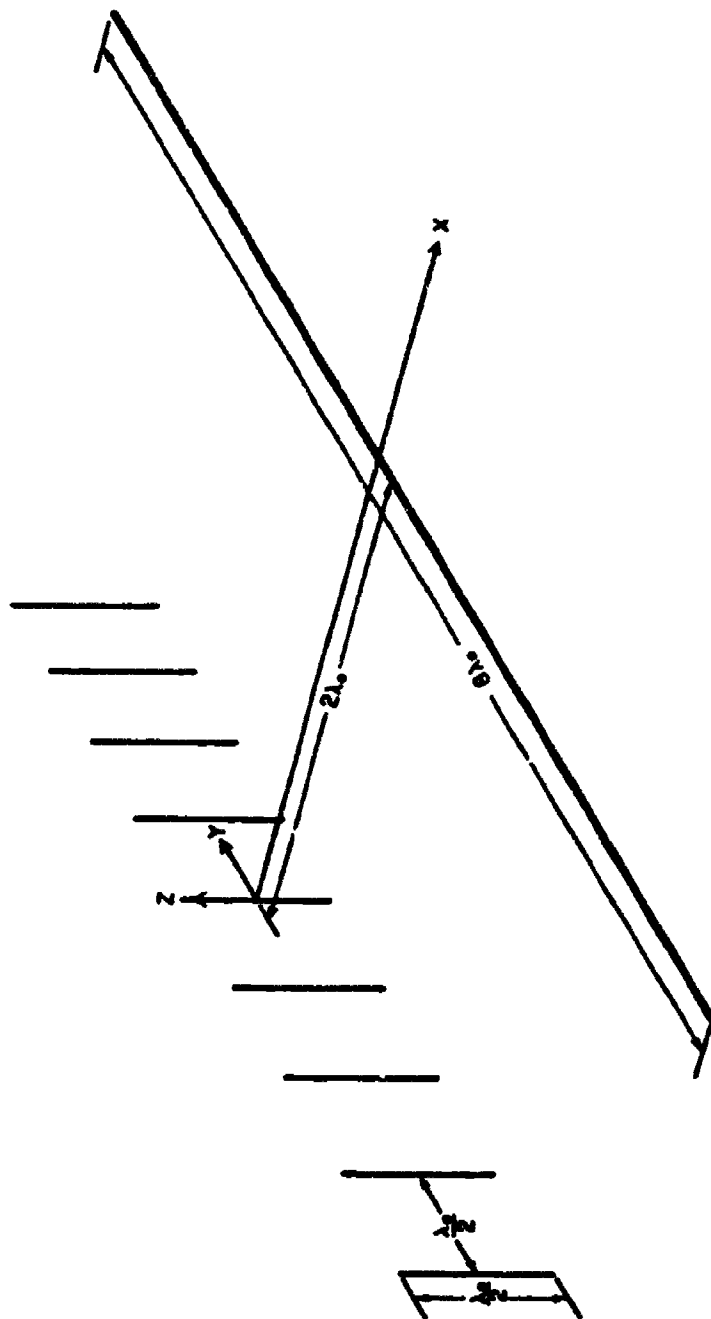


Figure 2-6. Sketch showing array and near-field parameters for the numerical simulation, where  $\lambda_0$  is the wavelength at the in-band frequency of 3.0 GHz.

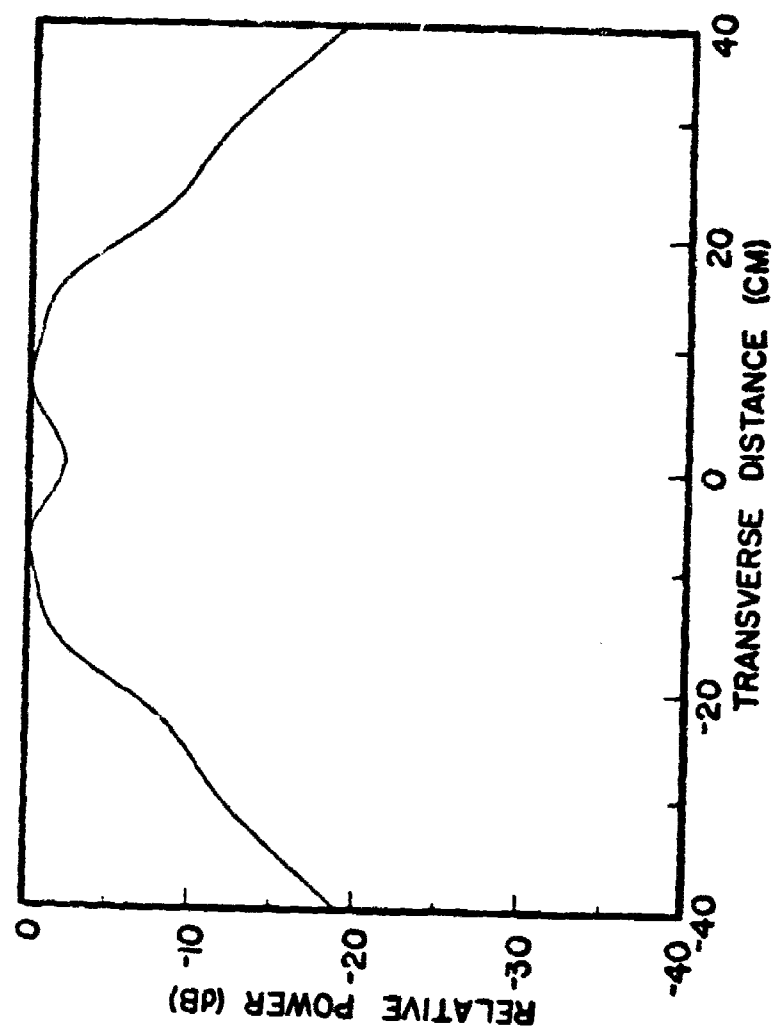


Figure 2-7. Non-random near-field power distribution for the in-band frequency of 3.0 GHz for the in-band scan angle of 0 degrees.

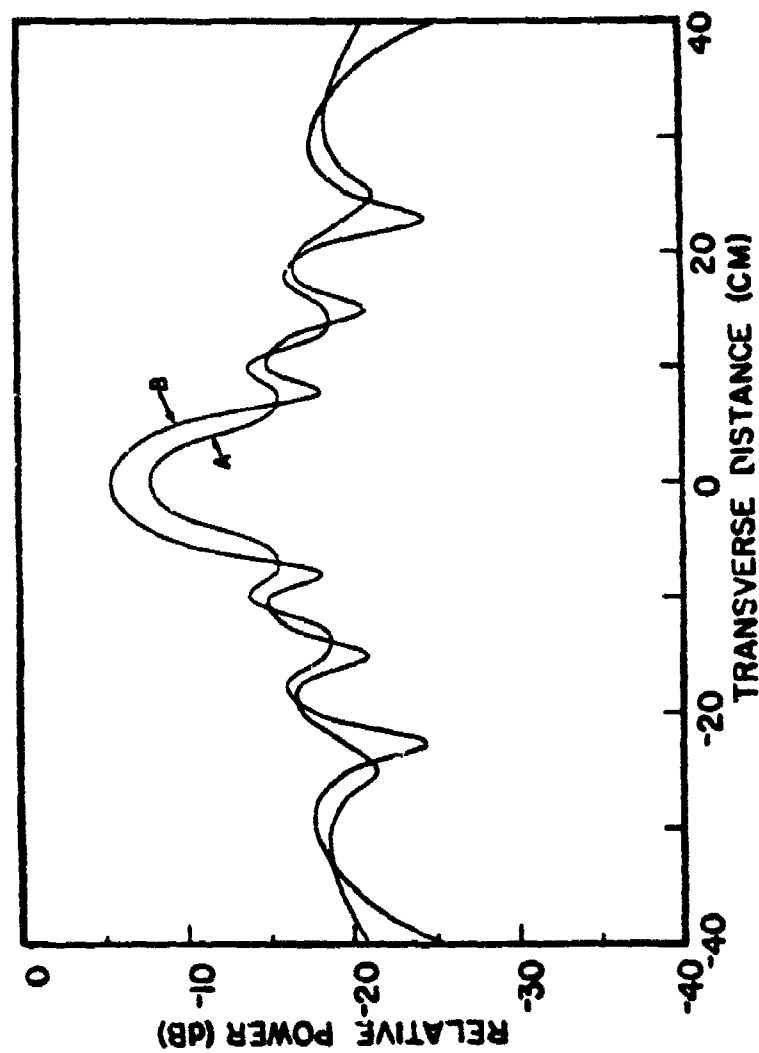


Figure 2-8. Intrinsic (A) and total (B) near-field covariance function of the electric field at  $y=0$  and the conjugate of the electric field at all other points on the near-field plane for the in-band frequency of 3 GHz for the in-band scan angle of 0 degrees.

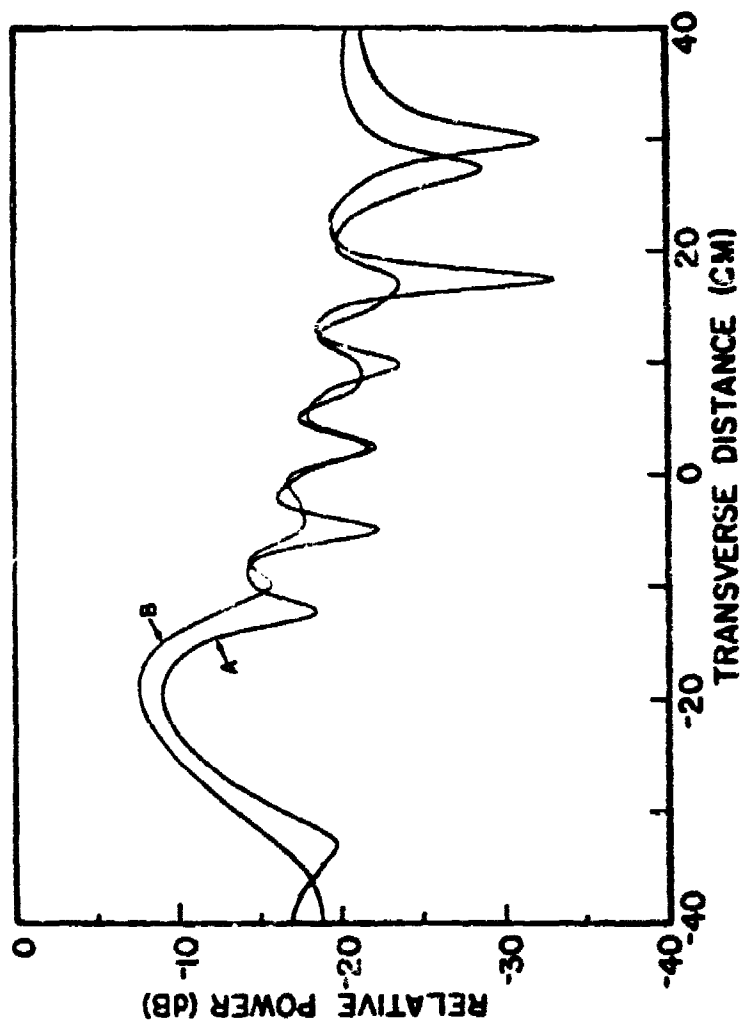


Figure 2-9. Intrinsic (A) and total (B) near-field covariance function of the electric field at  $y=-20$  and the conjugate of the electric field at all other points on the near-field plane for the in-band frequency of 3 GHz for the in-band scan angle of 0 degrees.

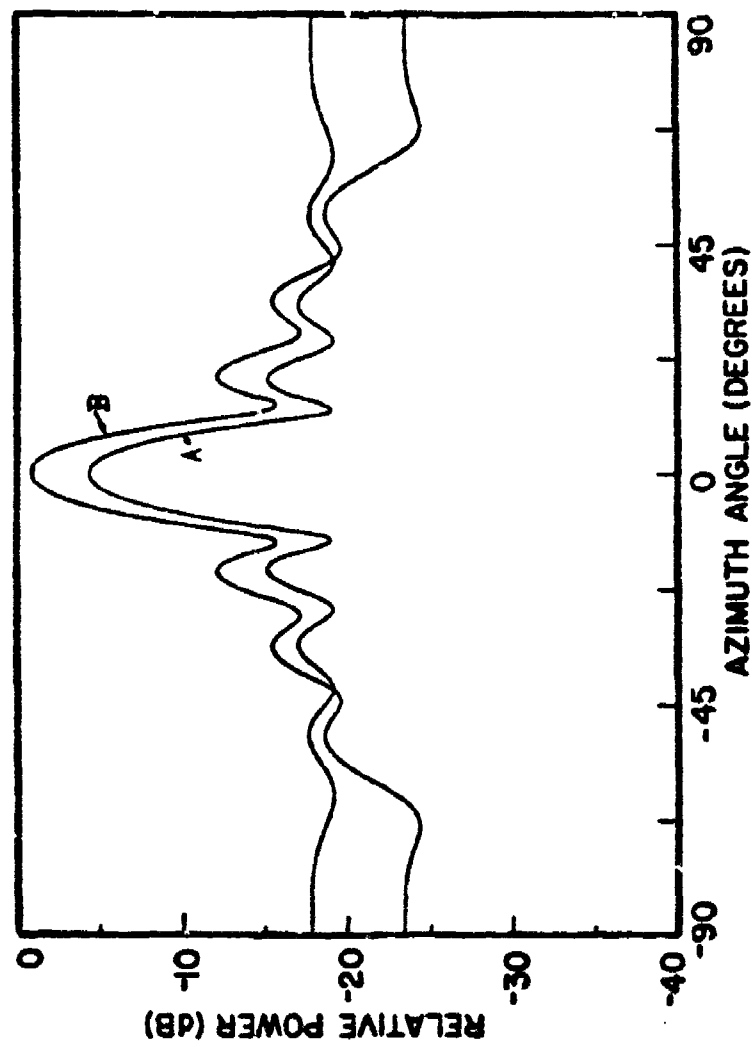


Figure 2-10. Analytical statistical average pattern for a nine-element dipole array of interacting (B) and non-interacting (A) elements for the in-band frequency of 3.0 GHz for the in-band scan angle of 0 degrees.



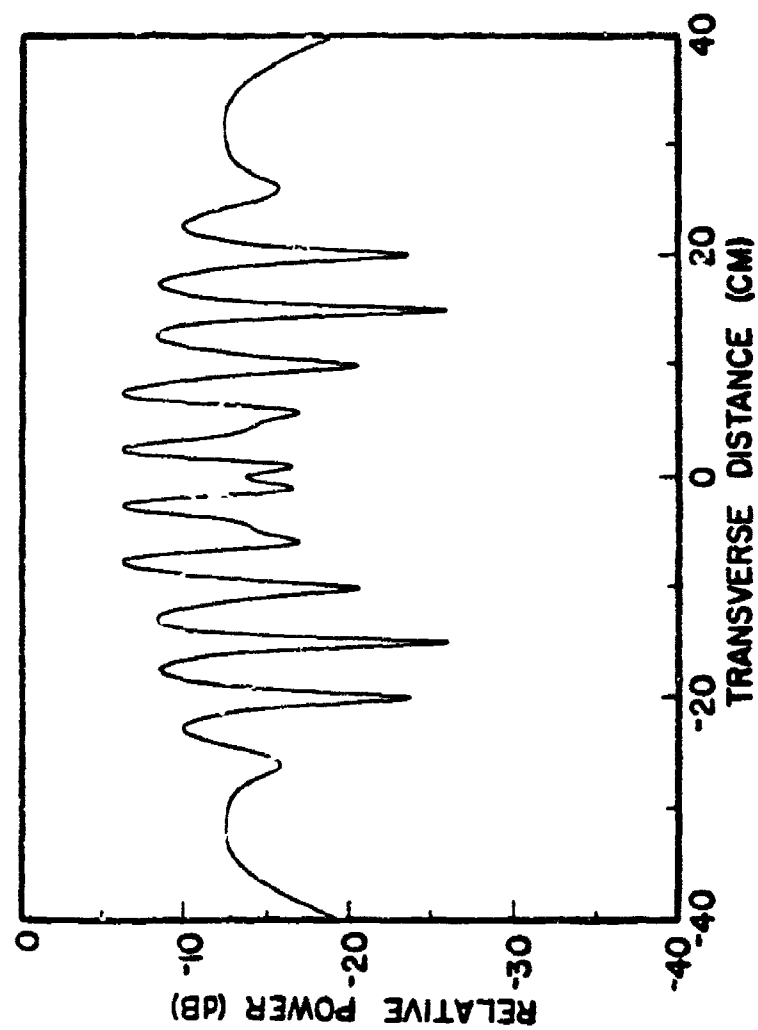


Figure 2-11. Non-random near-field power distribution for the out-of-band frequency of 9.0 GHz for the in-band scan angle of 0 degrees.

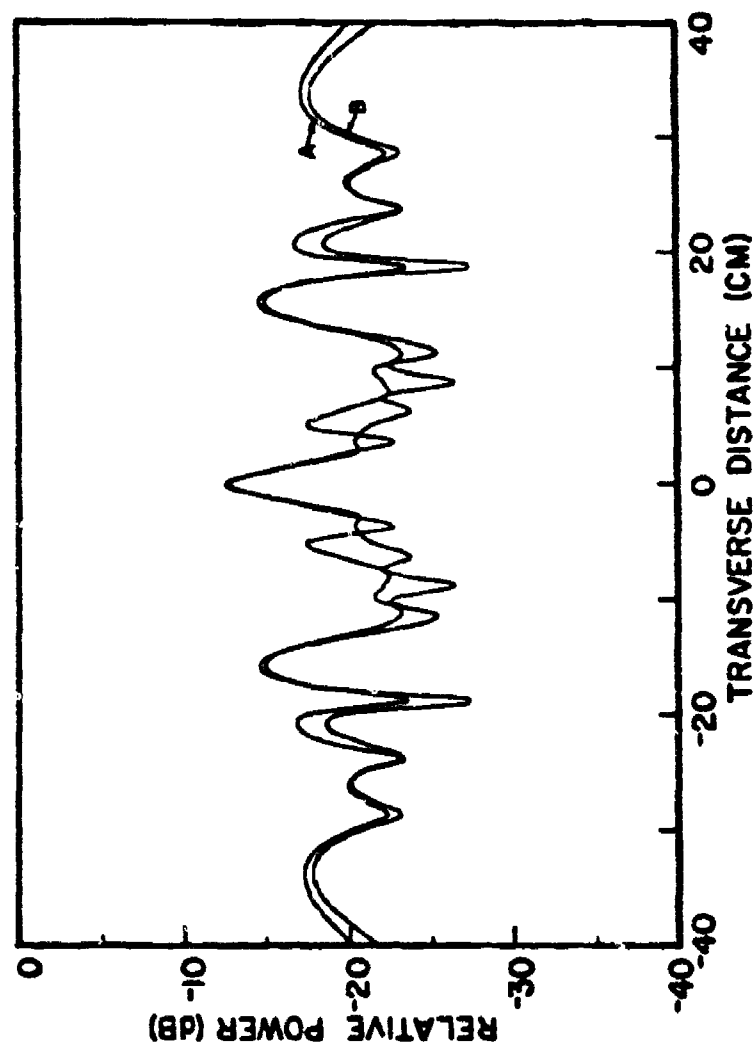


Figure 2-12. Intrinsic (A) and total (B) near-field covariance function of the electric field at  $y=0$  and the conjugate of the electric field at all other points on the near-field plane for the out-of-band frequency of 9 GHz for the in-band scan angle of 0 degrees.

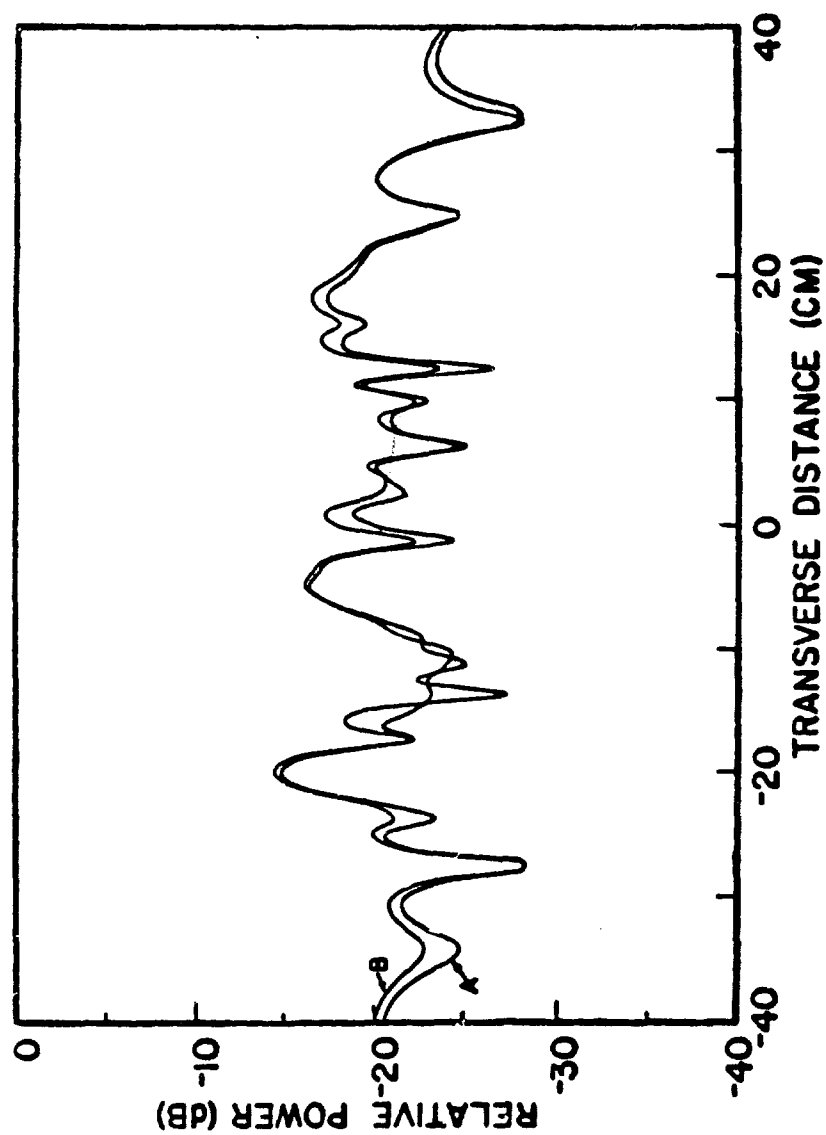


Figure 2-13. Intrinsic (A) and total (B) near-field covariance function of the electric field at  $y=-20$  and the conjugate of the electric field at all other points on the near-field plane for the out-of-band frequency of 9 GHz for the in-band scan angle of 0 degrees.

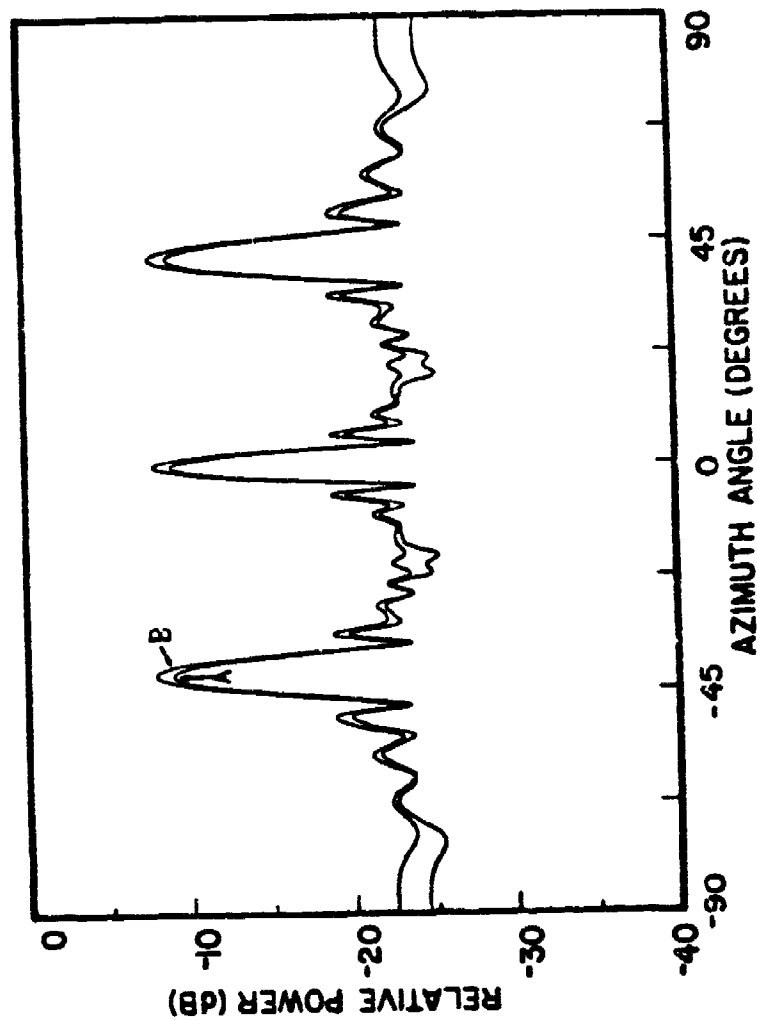


Figure 2-14. Analytical statistical average pattern for a nine-element dipole array of interacting (B) and non-interacting (A) elements for the out-of-band frequency of 9.0 GHz for the in-band scan angle of 0 degrees.

is finite. An infinite array would everywhere have a symmetric covariance function. The total covariance function has greater peak magnitude than the intrinsic covariance, and also has broader lobes. These differences are more pronounced for the in-band frequency. This is reasonable because the current elements are only weakly coupled at 9 GHz. Accordingly, the interactive covariance component of the total covariance is much smaller than the intrinsic covariance component and hence the total and intrinsic covariances do not differ markedly at 9.0 GHz.

The behavior of the statistical average far-field power patterns may be examined via the plots shown in Figure 2-10 for 3.0 GHz and Figure 2-14 for 9.0 GHz. The statistical average patterns for the array of interacting current elements have greater peak magnitude and decrease more rapidly versus azimuth angle than the average patterns for the array of non-interacting current elements. The difference in the average patterns for interacting and non-interacting elements is more pronounced for the in-band frequency than for the out-of-band frequency. This result could have been anticipated from the near-field covariance functions because the total and intrinsic near-field covariances are significantly different for 3.0 GHz but are only slightly different for 9.0 GHz. The results for other scan angles not displayed herein are entirely consistent with the results for the broadside scan angle.

It can be inferred from these results that the intrinsic covariance function is a "good" engineering approximation to the total covariance function if the inter-element coupling is sufficiently weak. Further numerical studies or, preferably, measured data are needed to determine if the inter-element coupling of multimoding out-of-band waveguide phased arrays is sufficiently weak to permit valid estimates of the average far-field power patterns to be obtained in this manner. Of course, it is preferable to determine the total covariance functions from the measured data. This possibility is addressed in the following subsection.

### 3. Recovery of Covariance Functions from Measured Data

In principle, the covariance functions can be recovered from the measured statistical data via matrix algebra, as follows. The near-field covariance function  $C_{q',q}$  is related to the current covariance function  $C_{l',l}$  via Equation (2-26), to wit:

$$C_{q',q} = \sum_{l'} \sum_l C_{l',l} G_{l',q}^* G_{l,q} \quad (2-34)$$

where  $G_{l,q}$  and  $G_{l',q}^*$  are the Green's function and its conjugate, as previously defined by Equation (2-27). This equation is equivalent to the matrix equation

$$\tilde{A} D = B \quad (2-35)$$

where  $D$  and  $B$  are column vectors corresponding to the element current covariances and the near-field covariances, respectively, and where  $\tilde{A}$  is the matrix formed from the product of the Green function and the appropriate conjugate Green function. Equation (2-35) may be written in terms of the matrix elements  $A_{ij}$  and the column vector components  $D_j$  and  $B_i$  as

$$\sum_j A_{ij} D_j = B_i \quad (2-36)$$

where the indices  $i$  and  $j$  are related to the  $(l',l)$  indices and  $(q',q)$  indices as

$$i = q, \quad (2-37)$$

where  $q'$  is fixed, and

$$j = l + (l' - 1) L. \quad (2-38)$$

If  $\tilde{A}$  is square and non-singular and the right hand column vector  $B$  is known from measurement, the unique solution for  $D$  can be obtained by solving the set of linear equations obtained from Equation (2-36). The index  $j$  must vary from 1 to  $L^2$ , where  $L$  is the number of radiating elements, and we choose  $i=1$  to  $L^2$  so that  $A$  will be a square matrix. This choice of maximum  $i=L^2$  means that measured values of the selected near-field covariance function must be supplied for  $L^2$  sample points on the near-field plane.

The matrix  $\tilde{A}$  will be non-singular if its determinant is non-zero [12]. Computer calculations of the determinants for 3-element array and for a 9-element array were performed using double precision arithmetic. These computations were conducted for several different near-field distances and for several different sets of sample point spacings for each near-field distance. It was found that the computed determinants for the 3-element array ranged from  $10^{-5}$  to  $10^{-8}$ . The computed determinants for the 9-element array ranged from  $10^{-12}$  to  $10^{-14}$ . These results imply that the matrix  $\tilde{A}$  is "nearly" singular. These numerical results do not prove that the matrix is non-singular because the computations are subject to non-negligible errors despite the use of double precision arithmetic. However, inspection of the matrix elements further supports the notion that the matrix is non-singular but that it is nearly singular. The elements of the  $9 \times 9$  matrix for the 3-element array are shown in Table 2-1. It can be discerned that the matrix elements do not differ markedly from each other. However, inspection of the full matrix shows that no two rows are the same nor are any two rows related by a constant. Similarly, no two columns are the same nor are any two columns related by a constant. Thus, one may conclude that the matrix is non-singular. One may also conclude from the determinant computations and from the fact that the matrix elements are so similar that the matrix is "nearly" singular.

One anticipates trouble in numerical computations involving a nearly singular matrix. Most computer programs designed to numerically perform matrix inversions or to solve systems of equations work well for a diagonally dominant matrix, but they can fail badly for a matrix

TABLE 2-1

THE 9X9 MATRIX ARISING IN THE SOLUTION OF THE  
NEAR-FIELD COVARIANCE FUNCTIONS FOR A WIRE ARRAY  
CONSISTING OF 3 RADIATING ELEMENTS\*

	1	2	3	4	5	6	7	8	9
1	0.01558559, 0.00000000	0.01517848, -0.00252555	0.01410401, -0.00551536	0.01517848, 0.00252555	0.0159125, 0.00000000	0.01462533, -0.00308582	0.014104017, 0.00551536	0.01462933, 0.00308581	0.01471503, 0.00000000
2	0.01588786, 0.00000000	0.0562785, -0.00187253	0.01492117, -0.00434272	0.01562785, 0.00187253	0.01559280, 0.00000000	0.0151882, -0.00251305	0.01492117, 0.00434272	0.01518982, 0.00251305	0.01520032, 0.00000000
3	0.01607594, 0.00000000	0.01554238, -0.00115464	0.01554935, -0.00300002	0.01594238, 0.00115464	0.01589286, 0.00000000	0.01563566, -0.00185851	0.01554935, 0.003000026	0.01563566, 0.00185851	0.01559996, 0.00000000
4	0.01641330, 0.00000000	0.01610505, -0.00039498	0.01594557, -0.00153316	0.01610505, 0.00039498	0.01607851, 0.00000000	0.01594724, -0.00113952	0.01594557, 0.00153316	0.01594724, 0.00113952	0.01589781, 0.00000000
5	0.01608103, 0.00000000	0.01610670, 0.00037928	0.01608103, 0.00000000	0.01610670, -0.00037928	0.01614136, 0.00000000	0.01610670, -0.00037928	0.0168103, 0.00000000	0.0161067, 0.00037928	0.01608103, 0.00000000
6	0.01589781, 0.00000000	0.01594724, 0.00113952	0.01594557, 0.00153316	0.01594724, -0.00113952	0.01607851, 0.00000000	0.01610505, 0.0039498	0.01594557, -0.00153316	0.01610505, -0.00039498	0.01607594, 0.00000000
7	0.01559996, 0.00000000	0.01563566, 0.00185851	0.01554935, 0.00300026	0.01563566, -0.00185851	0.01589286, 0.00000000	0.01594238, 0.00115464	0.01554935, -0.00300026	0.01594238, -0.00115464	0.01607594, 0.00000000
8	0.01520032, 0.00000000	0.01518882, 0.00251305	0.01492117, 0.00434272	0.01518882, -0.00251305	0.01559280, 0.00000000	0.01562785, 0.00187253	0.01492117, -0.00434272	0.01562785, -0.00187253	0.01588786, 0.00000000
9	0.01471503, 0.00000000	0.01462933, 0.00308581	0.01410401, 0.00551536	0.01462933, -0.00308581	0.01519125, 0.00000000	0.01517848, 0.00252555	0.01410401, -0.00551536	0.01517848, -0.00252555	0.01558559, 0.00000000

\*The upper and lower numbers for each entry are the real and imaginary parts, respectively,  
of complex number  $G_{pq}$  computed from Equation (2-27).



that departs "too much" from the diagonally dominant situation. The matrix A is certainly "ill conditioned" in comparison to a diagonally dominant matrix. Consequently, the more common methods such as Gaussian elimination with iterative improvement or the iterative Gauss-Seidel and Jacobi techniques [13] failed to converge to accurate, or even sensible, answers for the 9-element array. A straightforward row reduction technique written for this problem gave good results for 3-element and 5-element arrays, but produced grossly erroneous results for 7-element and 9-element arrays.

Acceptable numerical results were finally obtained with an algorithm based on a projection method for solving singular or nearly-singular systems of equations [14]. This same method has been employed in the analysis of probe compensation errors conducted under this same contract and is well documented in Reference [15]. The basic method of solution can be summarized by considering the expression for the (m+1)th iterate,

$$D^{(m+1)} = D^m - \frac{[D^{(m)}, a_m] - B_m}{[a_m, a_m]} a_m \quad (2-39)$$

where  $D^{(m)}$  is the solution after m iterations of this equation,  $a_m$  is the mth column vector of the transpose conjugate matrix of A,  $B_m$  is the mth element of B, and where the square brackets denote the inner product of the enclosed quantities. A formal proof that this sequence converges for any A, B, and initial guess  $D^{(0)}$  is presented in Reference [14]. If the system of equations is consistent, it then follows that the limit point is a solution of the system.

The real parts of the exact values of the normalized current covariances and the values computed from the projection algorithm are plotted in Figure 2-15 for a 9-element wire array operating at 3.0 GHz. The plotted data are normalized to the largest value of the exact current covariance. The data are symmetrical about the center point (5,5) and, hence, only the data for (1,1) through (5,5) are plotted. The magnitudes of the imaginary parts of the exact and estimated covariances are  $\leq 0.012$  and  $\leq 0.04$ , respectively, and are therefore not plotted. The computed values plotted in Figure 2-15 were obtained

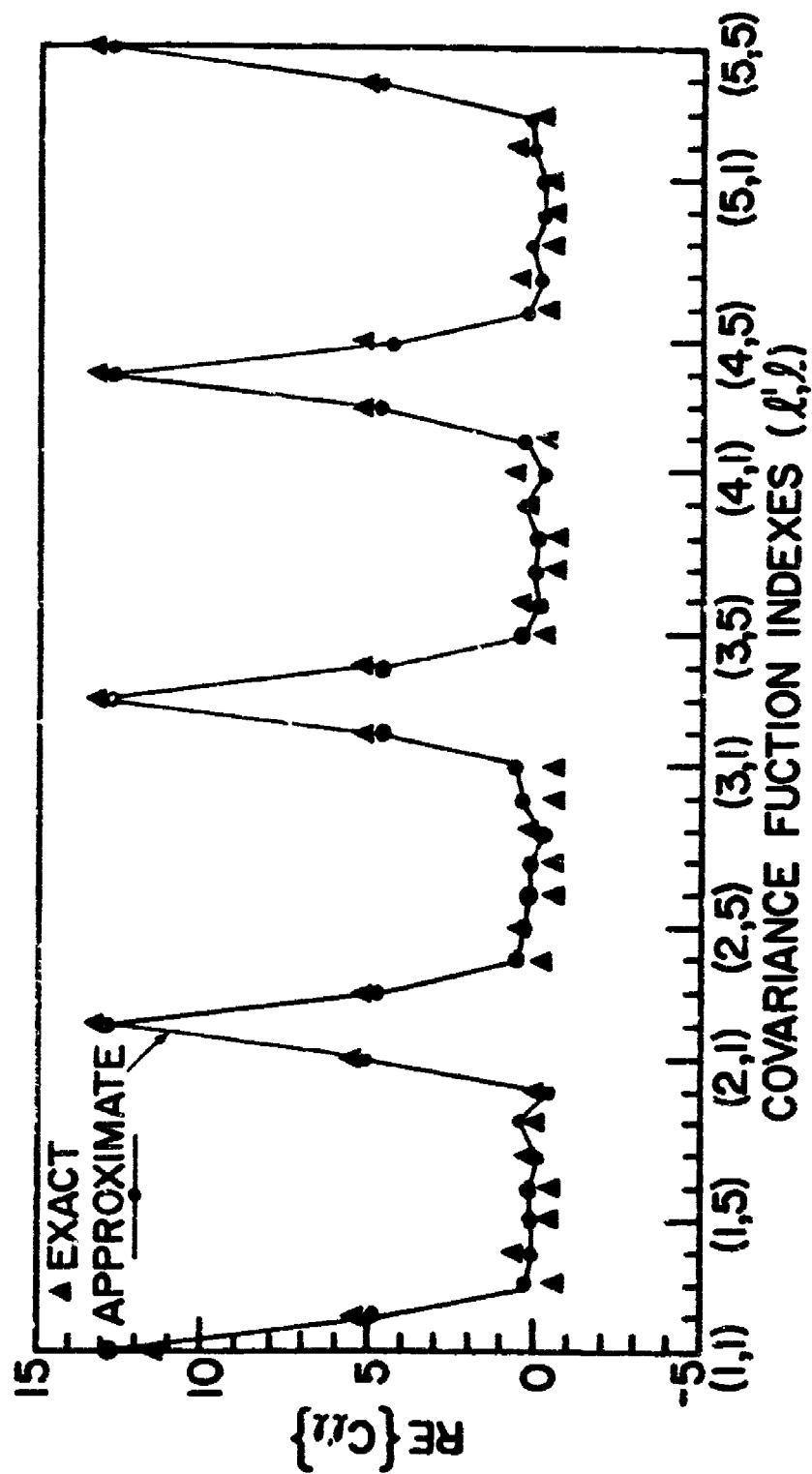


Figure 2-15. The exact and the approximate element current covariance function for the 9-element wire array for the frequency of 3.0 GHz for uncorrelated input voltages.

by iterating Equation (2-39) 100 times, which took 57 seconds of cpu time. Additional iterations produce negligible improvement of the data. The initial starting value for the iterations was

$$D_j \rightarrow C_{\ell', \ell} = (L + \sqrt{L}) \exp[-.693(\ell' - \ell)^2] \quad (2-40)$$

The right hand column vector B for this computation was the self covariance function  $C_{qq}$ , which is just the variance of the electric field on the near-field measurement plane. (Similar results are obtained if a measured cross covariance function is used as the known right hand column vector). The computed element covariances generally replicate the prominent "lobes" of the exact element covariances.

Plots of the magnitude of the exact and computed near-field cross covariance function  $C_{41q}$  (for  $q=1,81$ ) are presented in Figure 2-16. The computed curve in the figure agrees closely with the exact curve over the portions of the graph where  $C_{41q}$  is large. The close agreement is attributed to the fact that functions obtained by summing or integrating over a large number of complex quantities are usually insensitive to small errors in the summand or integrand.

The results just discussed indicate that useful estimates of the near-field covariance functions can be obtained from a knowledge of the self covariance function on the measurement plane. Knowledge of at least one cross covariance function is also needed in order to provide a good check of computational accuracy. Additional research is needed in order to determine the feasibility and accuracy of this method of recovering the covariance functions for arrays comprised of hundreds or even thousands of elements.

#### D. Probability Density Functions

A thorough characterization of the radiation pattern statistics can be obtained if the probability density function (p.d.f.) for either the radiated field amplitude or the radiated power density can be discerned. Once the p.d.f. is known, the standard deviation or any other higher order statistical moment can be computed. Similarly, the cumulative probability distribution (c.p.d.) is readily computed by integrating the p.d.f. Of course, the computations of the statistical

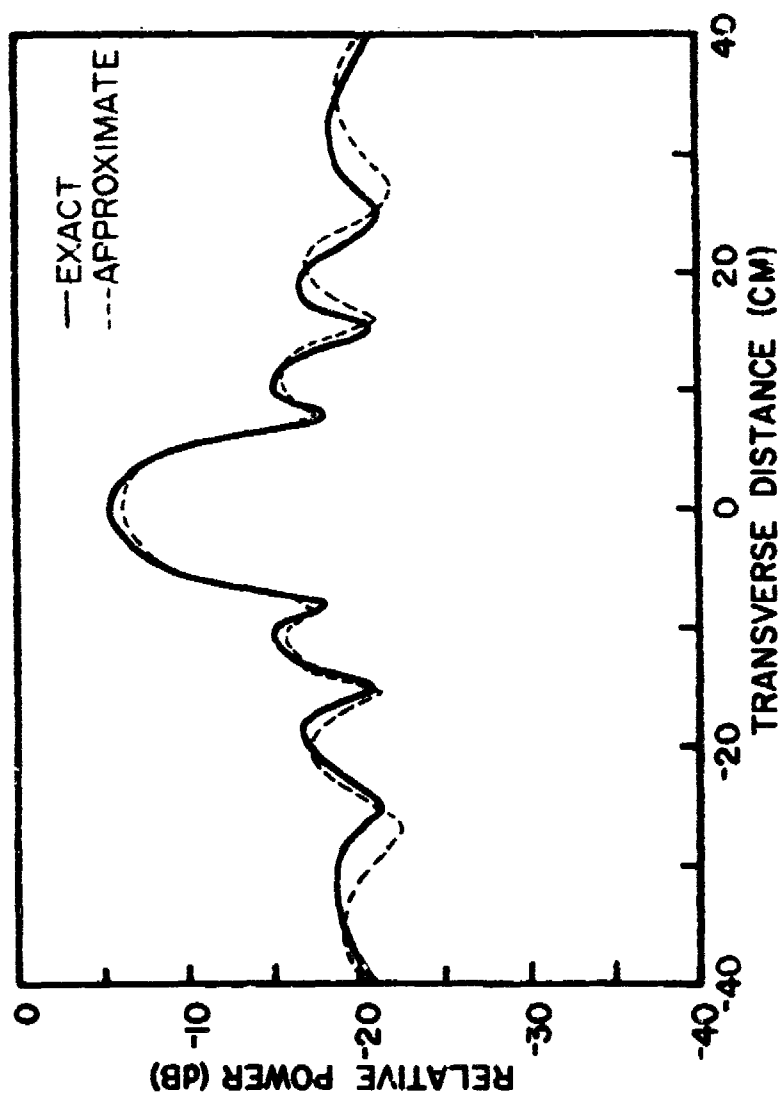


Figure 2-16. The exact and the approximate near-field covariance function for the electric field at  $y=0$  with the conjugate of the electric field at all other sample points on the measurement plane.

moments or the c.p.d. may have to be performed numerically because closed-form analytical expressions consisting of a finite sum of elementary functions for the integrals involving the p.d.f. may not be available. Nevertheless, it is usually more efficient to compute radiation pattern statistical data via the use of a reasonably accurate p.d.f. than to compute radiation pattern statistical data directly in terms of the near-field statistical data as was done for the average radiated far field power density.

A study of the modern literature concerning electromagnetic scattering and radiation statistics indicates that the p.d.f. derived by M. Nakagami [16] in 1954, and that also was independently derived by P. Beckman [17] in 1961, is the most general one. Other p.d.f.'s for radiation/scattering, such as those due to S.O. Rice, Hoyt, and Lord Rayleigh [18-20] may be derived from the Nakagami p.d.f.

The key assumption in the derivation of the Nakagami p.d.f. is that the real and imaginary parts of the randomly varying electromagnetic field both follow a Gaussian p.d.f.. The Gaussian p.d.f. is an excellent approximation to the true p.d.f. if the electric field is produced by a large number of statistically independent sources. In practice, about 7 or more statistically independent sources are sufficient to yield closely Gaussian p.d.f.'s for the real and imaginary parts of the radiated field.

It may appear at first sight that the Nakagami p.d.f. is not applicable to the randomly excited wire array studied in subsection C because the element currents, as well as the measured near-field electric fields, are definitely correlated. However, the radiated electric fields at any point in the near-field or the far-field of the antenna can be expressed as a sum of terms involving non random matrix elements multiplied by the statistically independent random input voltages. Specifically, the electric field  $E_q$  is related to the input voltages  $V_k$  as

$$E_q = \sum_l \sum_k G_{lk} \Gamma_{lk} V_k \quad (2-41)$$

where all other symbols are as previously defined. The real part  $X_q$  of  $E_q$  and the imaginary part  $Y_q$  of  $E_q$  are then

$$X_q = \sum_p [ (H_r)_{qp} (V_r)_p - (H_i)_{qp} (V_i)_p ] \quad \text{and} \quad (2-42)$$

$$Y_q = \sum_p [ (H_i)_{qp} (V_r)_p + (H_r)_{qp} (V_i)_p ] \quad (2-43)$$

where

$(V_r)_p$  = the real part of the complex random input voltage  $V_p$ ,

$(V_i)_p$  = the imaginary part of the complex random input voltage  $V_p$ , and

where the coefficients of  $(V_r)_p$  and  $(V_i)_p$  are

$$(H_r)_{qp} = \text{Re} \{ \sum_l G_{lq} \Gamma_{pl} \}, \quad \text{and} \quad (2-44)$$

$$(H_i)_{qp} = \text{Im} \{ \sum_l G_{lq} \Gamma_{pl} \} \quad (2-45)$$

The real part of  $E_q$  given by Equation (2-42) and the imaginary part of  $E_q$  given by Equation (2-43) are each just the sum of statistically independent random variables, and if the number of voltages is  $\geq 7$ , the p.d.f. for  $X$  and the p.d.f. for  $Y$  will both be Gaussian [17] to good approximation. Hence, the amplitude of the radiated field will follow the Nakagami p.d.f. This is true for both the (radiating) near-field amplitude and the far-field amplitude.

The derivation of the Nakagami p.d.f. involves the use of the joint probability density of  $X$  and  $Y$ . The joint p.d.f. for two Gaussian random variables  $X$  and  $Y$  is known to be [8].

$$\begin{aligned} f(X,Y) = \frac{1}{2\pi\sigma_1\sigma_2\gamma} \left\{ \exp \left[ -\frac{(X-\langle X \rangle)^2}{2\gamma^2\sigma_1^2} - \frac{(Y-\langle Y \rangle)^2}{2\gamma^2\sigma_2^2} \right] \right. \\ \left. \exp \left\{ \frac{2\rho[X-\langle X \rangle][Y-\langle Y \rangle]}{2\gamma^2\sigma_1\sigma_2} \right\} \right\} \end{aligned} \quad (2-46)$$

where  $X$  and  $Y$  are the average values of  $X$  and  $Y$ , and  $\sigma_1$  and  $\sigma_2$  are the standard deviations of  $X$  and  $Y$ , respectively.  $\rho$  is the correlation coefficient for  $X$  and  $Y$ , and  $\gamma = \sqrt{1-\rho^2}$ . We have omitted the subscript  $q$  from  $X$  and  $Y$  for convenience.

The Nakagami p.d.f.  $f(P)$  for the power density  $P$  is preferred here and is obtained as follows. First, the joint p.d.f. for  $X$  and  $Y$  is expressed in polar coordinates by replacing  $X$  and  $Y$  by

$$X = \sqrt{P} \cos(\phi) \quad \text{and} \quad (2-47)$$

$$Y = \sqrt{P} \sin(\phi) \quad , \quad (2-48)$$

where  $P = X^2 + Y^2$ , and integrated over the annular ring of thickness  $dS$  from  $0$  to  $2\pi$ , to wit:

$$f(P) = \frac{dP}{4\pi\sigma_1\sigma_2\gamma} \int_0^{2\pi} \exp \left\{ -\frac{1}{2\gamma^2} \left[ \frac{(\sqrt{P} \cos(\phi) - \langle X \rangle)^2}{\sigma_1^2} + \frac{(\sqrt{P} \sin(\phi) - \langle Y \rangle)^2}{\sigma_2^2} \right] \right. \\ \left. \times \exp \left[ \frac{2\rho[\sqrt{P} \cos(\phi) - \langle X \rangle][\sqrt{P} \sin(\phi) - \langle Y \rangle]}{2\gamma^2\sigma_1\sigma_2} \right] \right\} d\phi \quad (2-49)$$

Next, the integral is expressed as an infinite sum involving modified Bessel functions of the first kind and integer order. The resulting expression for  $f(P)$  is then

$$f(P) = \frac{1}{\sqrt{\alpha\beta}} \exp [gP + hA^2] \\ \times \sum_n \epsilon_n I_n \left[ \frac{P}{2} \left( \frac{1}{\beta} - \frac{1}{\alpha} \right) \right] I_{2n} \left[ 2\sqrt{P} \cdot \sqrt{a^2 + b^2} \right] \cos(n\xi) \quad (2-50)$$

where  $\epsilon_n$  is Neumann's factor ( $\epsilon_n=1$  for  $n=0$  and  $\epsilon_n=2$  otherwise) and where the other symbols are defined as follows:

$$g = \frac{1}{2} \left( \frac{1}{\alpha} + \frac{1}{\beta} \right), \quad (2-51)$$

$$\alpha = \sigma_1 + \sigma_2 + [4\rho^2 + (\sigma_1^2 - \sigma_2^2)]^{1/2}, \quad (2-52)$$

$$\beta = \sigma_1 + \sigma_2 - [4\rho^2 + (\sigma_1^2 - \sigma_2^2)]^{1/2}, \quad (2-53)$$

$$A = \langle X \rangle^2 + \langle Y \rangle^2, \quad (2-54)$$

$$a = \frac{A}{\alpha} \cos(\delta_1 - \delta_2), \quad (2-55)$$

$$b = \frac{A}{\beta} \sin(\delta_1 - \delta_2), \quad (2-56)$$

$$\delta_1 = \frac{1}{2} \tan^{-1} \left[ \frac{\langle X \rangle}{\langle Y \rangle} \right], \quad (2-57)$$

$$\delta_2 = \frac{1}{2} \tan^{-1} \left[ \frac{2\rho}{\sigma_1 - \sigma_2} \right], \quad (2-58)$$

$$h = a^2 \alpha + b^2 \beta, \text{ and} \quad (2-59)$$

$$\xi = \tan^{-1} \left[ \frac{\alpha}{\beta} [\tan(\delta_1 - \delta_2)] \right]. \quad (2-60)$$

All of the new quantities for this expression for  $f(p)$  are computed solely in terms of the same variables that are needed to define the joint p.d.f. for  $X$  and  $Y$ . These are (1) the average values of  $X$  and  $Y$ , (2) the standard deviations of  $X$  and  $Y$ , and (3) the correlation coefficient for  $X$  and  $Y$ . It should be noted that these variables generally depend on frequency, array scan angle and the coordinates of the field point under consideration. In particular, the far-field power density  $P = P(\omega, \phi)$  depends on frequency, the azimuth angle of the field point, and the array scan angle.

The average values and standard deviations of  $X$  and  $Y$  as well as their correlation coefficient  $\rho$  can be computed with the aid of Equations (2-42) and (2-43) when the statistics of the input voltages are specified from theory or experiment. The equations for  $X$ ,



$Y$  ,  $\sigma_1$  ,  $\sigma_2$  and  $\rho$  can be computed directly in terms of the input voltage statistical parameters.

The average values and standard deviations of  $X$  and  $Y$  are also readily obtained from a Type II near-field measurement as described in subsection C. The computation of the correlation coefficient  $\rho$  from the measured data for arbitrary random excitations involves problems similar to those encountered for the covariance functions that were discussed in the preceeding subsection. However, it is possible to obtain valid estimates of  $\rho$  by assuming that the random voltage variations have the same variance at each element.

Numerical analyses were conducted to assess the validity of the Nakagami p.d.f. for computing the far-field amplitude p.d.f. for the nine element wire array described previously in subsection C. The computations of the Nakagami p.d.f. were accomplished by numerically integrating the expression for  $f(P)$  given by Equation (2-49) rather than by summing the series expression given by Equation (2-50). These computations were performed for two different sets of input parameters

$X$  ,  $Y$  ,  $\sigma_1$  ,  $\sigma_2$ , and  $\rho$  to the Equation (2-49). The first set of input parameter values were the values of  $X$  ,  $Y$  ,  $\sigma_1$  ,  $\sigma_2$ , and computed by specifying the input voltage statistics for statistically independent input voltages. This set forms a proper set of input parameters for the Nakagami p.d.f. The second set of values for  $X$  ,  $Y$  ,  $\sigma_1$  ,  $\sigma_2$ , and  $\rho$  were computed directly from simulated correlated voltages with an assumed Gaussian correlation function. This set of input parameters involves correlated "sources" and therefore violates the strict criteria for obtaining the Nakagami p.d.f. The input voltages for both situations had Gaussian phase distributions with zero mean value and standard deviation of 57 degrees on all elements. The Gaussian correlation for the correlated voltages was

$$C_{\kappa, \kappa'} = \exp \left[ -[.693 (\kappa - \kappa')^2] \right] \quad (2-61)$$

where  $\kappa$  and  $\kappa'$  are element numbers.

Monte Carlo calculations were performed to produce data for constructing the cumulative probability distribution for the far-field

amplitude in the boresight direction along the nose of the mainbeam and in a direction of a low sidelobe. The cumulative distributions were obtained from 50 Monte Carlo runs. The cumulative distributions based on the Nakagami p.d.f. were obtained by numerically integrating  $f(P)$ .

Plots of the cumulative distributions are shown in Figures 2-17 through 2-20. Each figure is a plot of the probability that the field amplitude is "less than or equal to" the abscissa. The abscissa in Figures 2-17 and 2-19 is the relative amplitude in real numbers while the abscissa in Figures 2-18 and 2-20 is the relative amplitude in decibels. The abscissas were scaled in this manner to display the interesting fact that the cumulative distribution resemble Gaussian cumulative distributions when plotted this way, in agreement with theory for the mainbeam and low sidelobe regions [2]. Each figure contains two cumulative distribution curves. These are (1) the curve constructed from Monte Carlo data, (2) the curve obtained from  $f(P)$ . The distributions in Figures 2-17 and 2-18 correspond to the statistically independent voltage sources, and distributions in Figures 2-19 and 2-20 correspond to the correlated input voltages.

Inspection of the plots contained in Figures 2-17 through 2-20 shows that the Nakagami curve obtained for statistically independent sources is in very good agreement with the Monte Carlo curve. Exact agreement is not expected because the Monte Carlo curve is constructed from "only" 50 runs. The Nakagami curve obtained for correlated sources is slightly less accurate but it is a reasonable approximation to the Monte Carlo curve.

These results serve to verify Nakagami's p.d.f. for statistically independent sources and they also indicate that it may be a useful engineering approximation for certain classes of moderately correlated sources. Namely, it may be applicable for near-field measurements involving randomly excited waveguide arrays for situations where the envelope of the near-field covariance function  $C_{q'q}$  decreases at least as rapidly as  $(1/q-q')$  as the difference between  $q$  and  $q'$  becomes "large." This condition appears to be true for the near-field data for the wire arrays considered in this study. However, further studies are needed to establish the range of applications for which the Nakagami

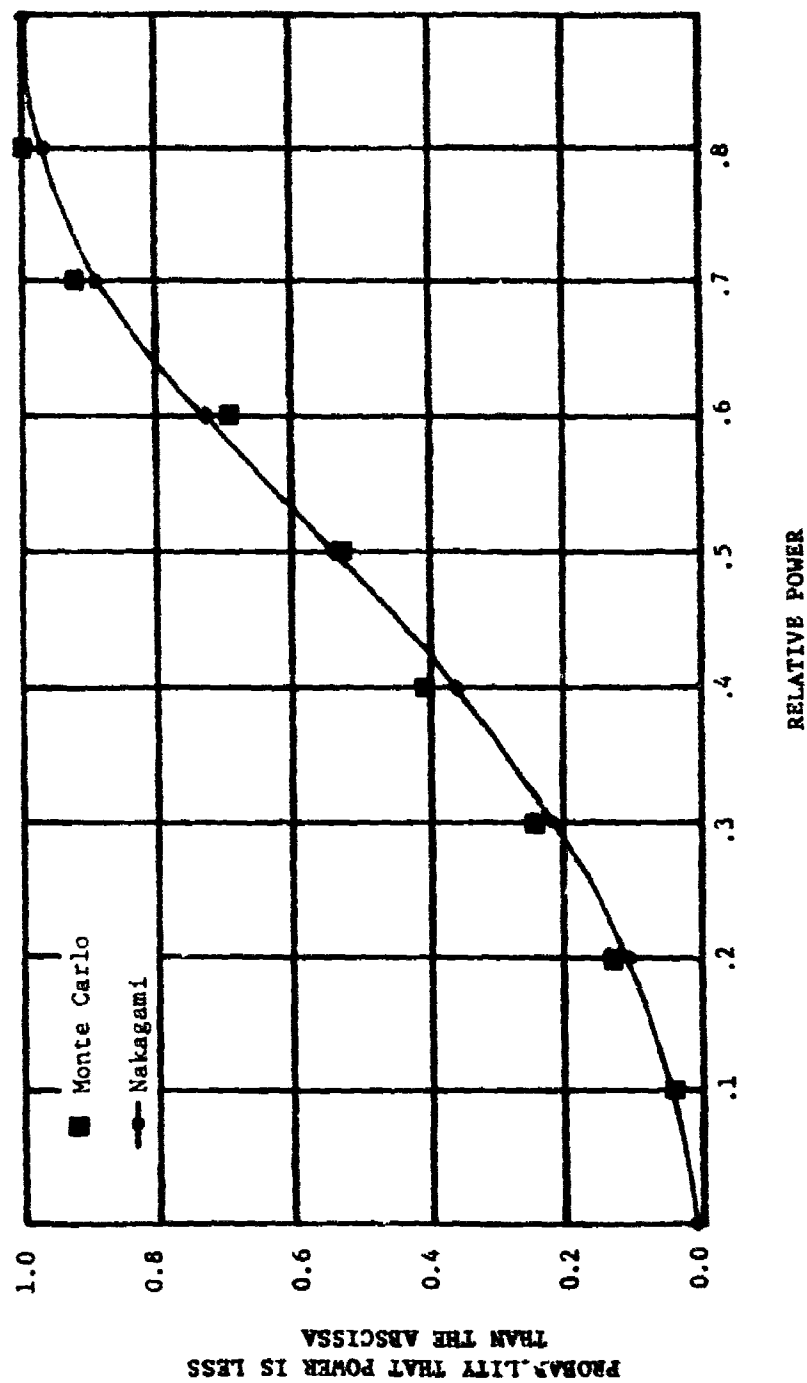


Figure 2-17. Cumulative probability distribution for the radiated power density of a mainbeam or grating lobe for a 9-element wire array with uncorrelated random input voltages.

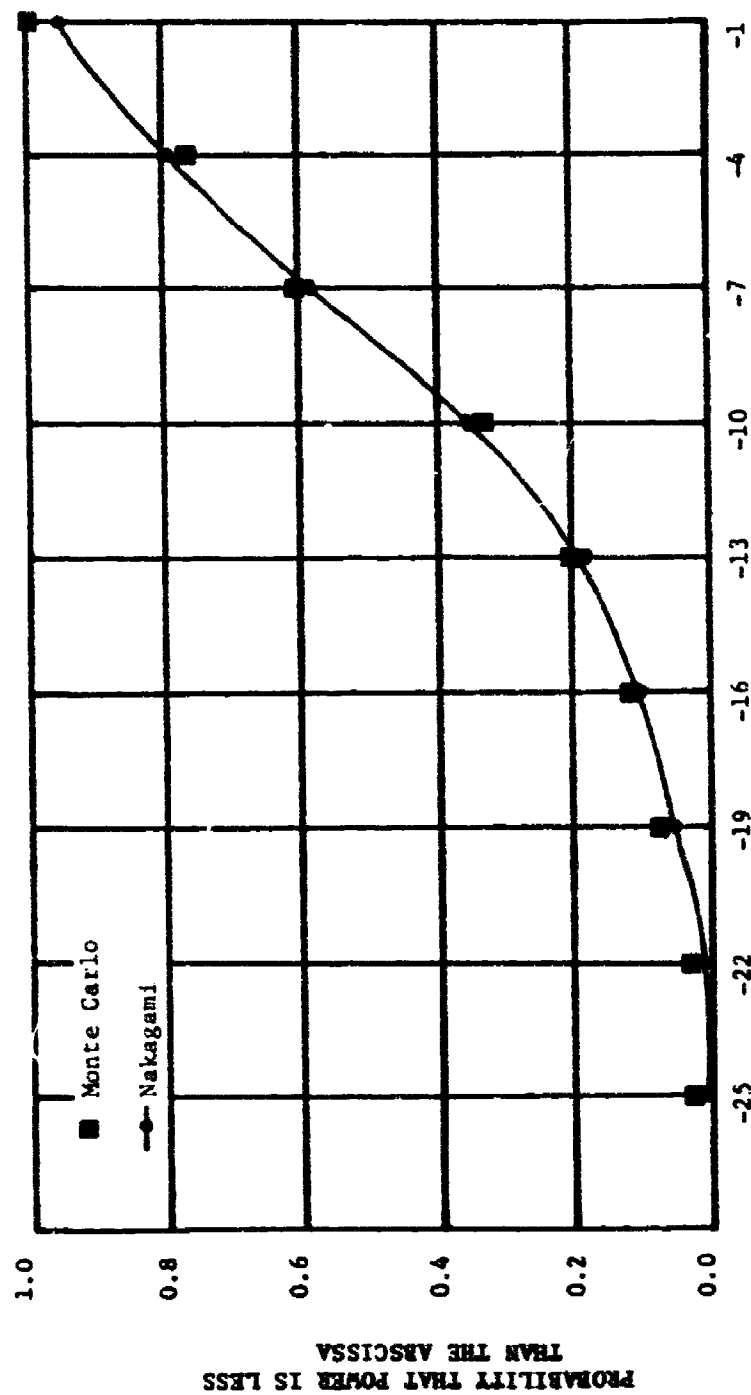


Figure 2-18. Cumulative probability distribution for the radiated power density of a low sidelobe for a 9-element wire array with uncorrelated random input voltages.

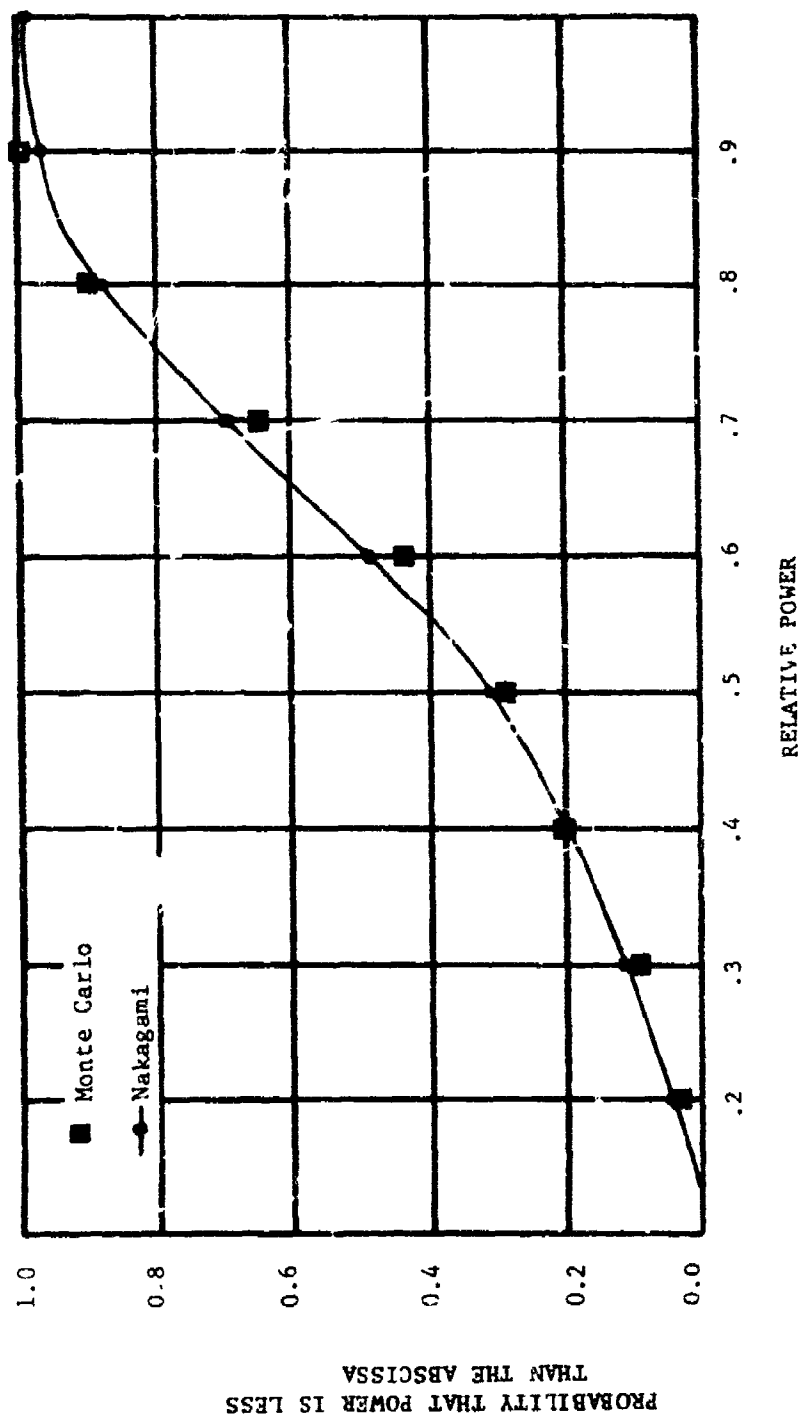


Figure 2-19. Cumulative probability distribution for the radiated power density of a mainbeam or grating lobe for a 9-element wire array with correlated random input voltages.

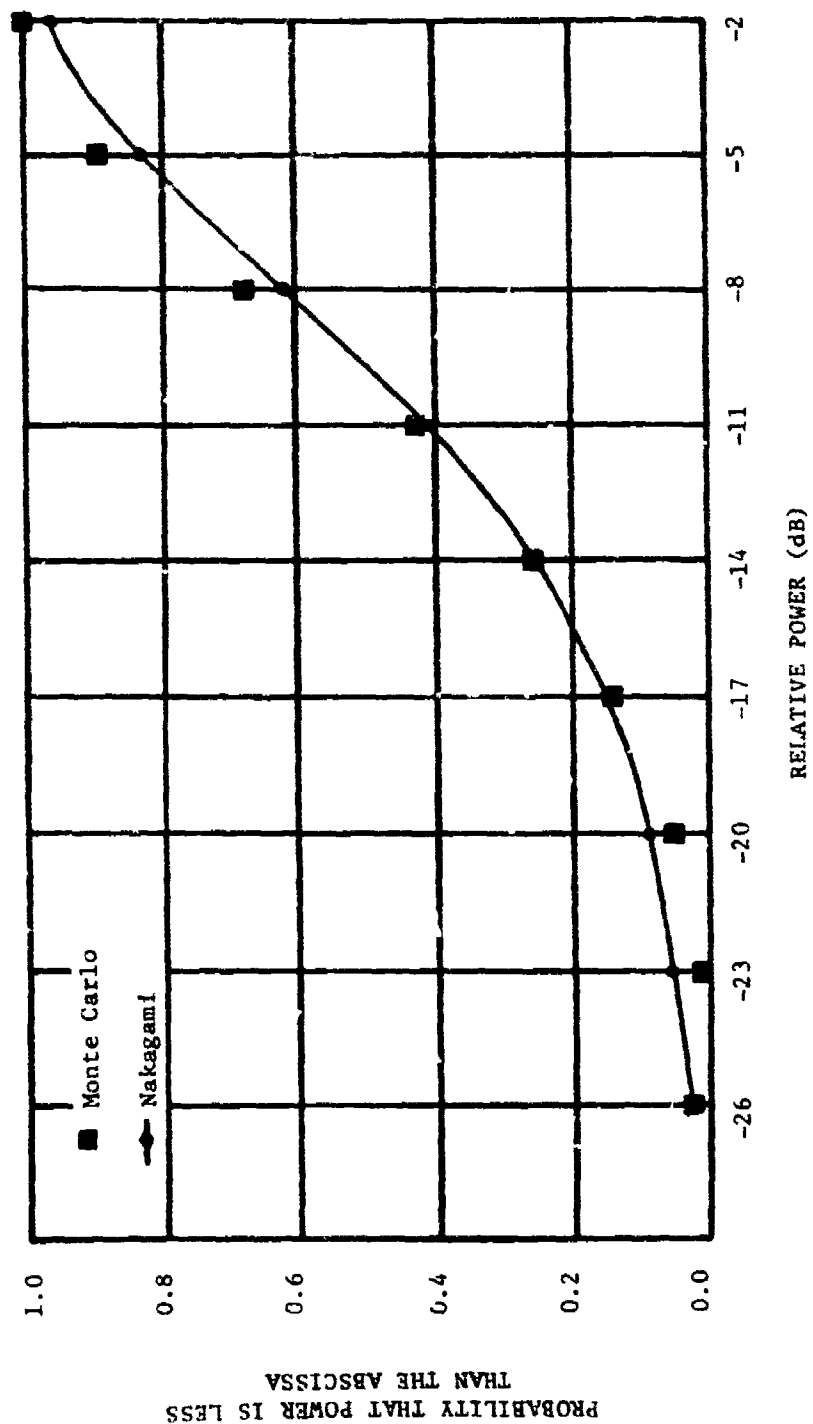


Figure 2-20. Cumulative probability distribution for the radiated power density of a low sidelobe for a 9-element array with correlated random input voltages.

p.d.f. can furnish valid engineering estimates of radiation statistics for correlated sources in general and for out-of-band waveguide arrays in particular.

A simpler but less accurate approximate expression for the radiation amplitude can be obtained that is nevertheless potentially useful for some engineering applications where less accuracy can be tolerated. The expression is derived by first ignoring the correlation between the real and imaginary parts of the radiated field. The effects of near-field source correlation are then incorporated as part of a parameter that appears naturally in the expression that was derived by ignoring the correlation between the real and imaginary parts of the radiated field. The approximate expression for the radiated power density obtained in this manner is

$$f[P(\omega, \phi)] = \frac{1}{\tau(\omega, \phi)} \exp \left[ - \frac{P(\omega, \phi) + \eta^2(\omega, \phi)}{\tau(\omega)} \right] \cdot I_0[B(\omega, \phi)] , \quad (2-62)$$

where  $f[P(\omega, \phi)]$  = probability density function for the far-field power density,

$$\eta^2(\omega, \phi) = \langle E^*(\omega, \phi) \rangle \langle E(\omega, \phi) \rangle , \quad (2-63)$$

$$\tau(\omega) = \sum_q \sum_q C_{q,q} \exp[j \frac{\omega}{c} \sin(\phi) (Y_q - Y_q)] , \quad (2-64)$$

$$I_0 [\cdot] = \text{Modified Bessel function of the first kind and order zero, and} \quad (2-65)$$

$$B(\omega, \phi) = \frac{\eta(\omega, \phi) P(\omega, \phi)}{\frac{1}{2} \tau(\omega)} . \quad (2-66)$$

Plots of the cumulative distribution computed from this equation are compared with the cumulative distribution obtained from the Monte Carlo data are shown in Figures 2-21 and 2-22. Reasonably good agreement is obtained between the Monte Carlo curves and the curves computed from Equation (2-62). However, additional testing is needed to properly define the limits of applicability of this relatively crude p.d.f. for antenna problems.

#### E. Time Domain Statistics

It is a well known fact that the time domain response of a deterministic radiating system can be analyzed conveniently from a knowledge of the complex frequency response via the Fourier transform technique. The same procedure can also be employed to obtain the statistical average time domain response of a randomly excited radiating system. The probability density function (p.d.f.) for the time domain response can also be discerned from the stochastic equations obtained in this manner.

The behavior of the far-field electric field as a function of time  $t$  is obtained from Fourier analysis of the frequency response as

$$E(t, \phi) = \frac{1}{2\pi} \sum_n E(\omega_n, \phi) \exp[j\omega_n t] \quad (2-67)$$

where

$E(t, \phi)$  = complex electric field at azimuth angle  $\phi$  versus time,  
and

$E(\omega_n, \phi)$  = the complex electric field at azimuth angle  $\phi$  for  
radian frequency  $\omega = 2\pi f$ , where  $f$  is the frequency in  
Hertz.

$E(\omega_n, \phi)$  is the product of the input pulse spectrum  $H(\omega_n)$  and the frequency response  $E^0(\omega_n, \phi)$  obtained from a uniformly weighted input frequency spectrum of width exceeding at least twice the bandwidth of  $H(\omega_n)$ . Hence,

$$E(\omega_n, \phi) = E^0(\omega_n, \phi) \cdot H(\omega_n) \quad (2-68)$$



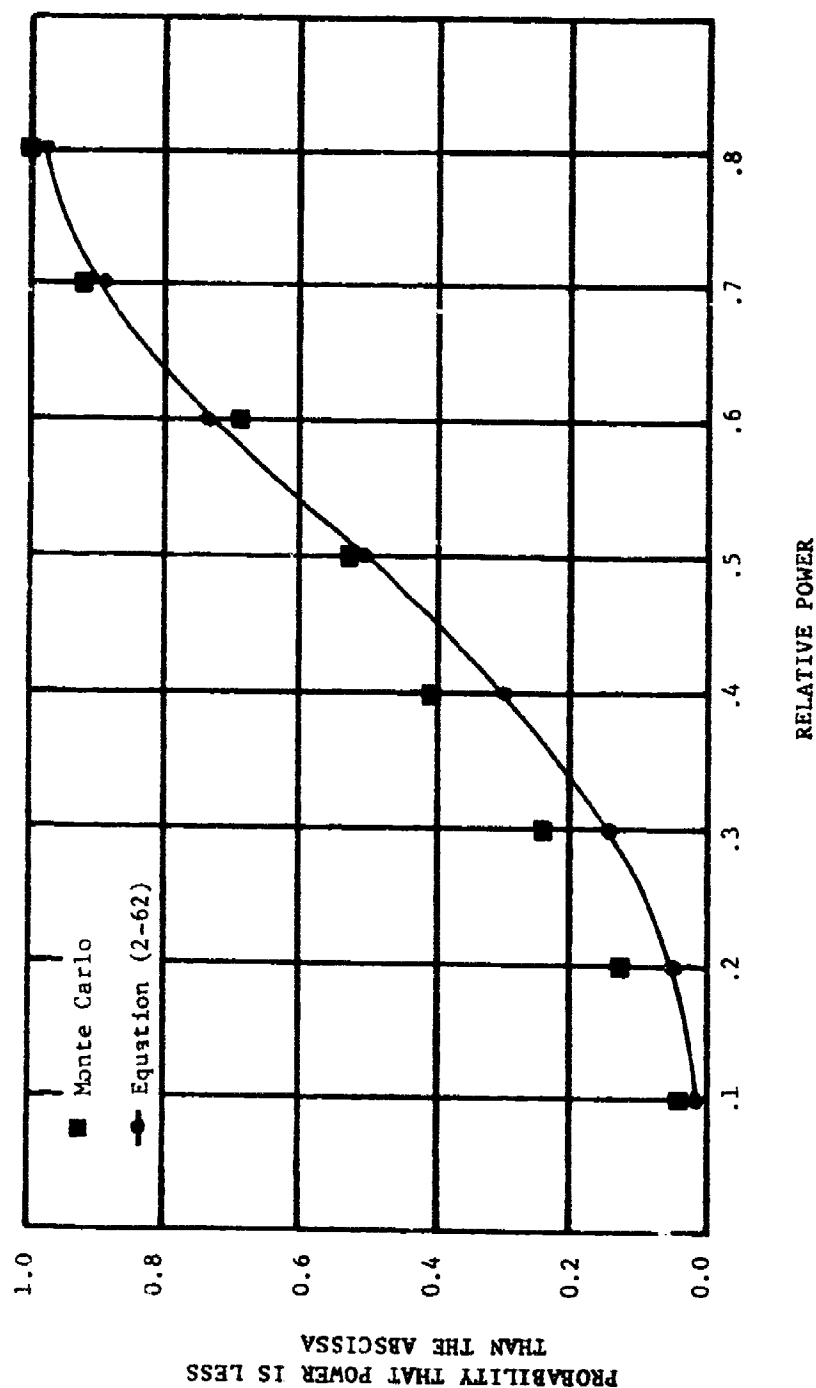


Figure 2-21. Cumulative probability distribution for the radiated power density of the mainbeam or grating lobe for a 9-element array with uncorrelated input voltages.

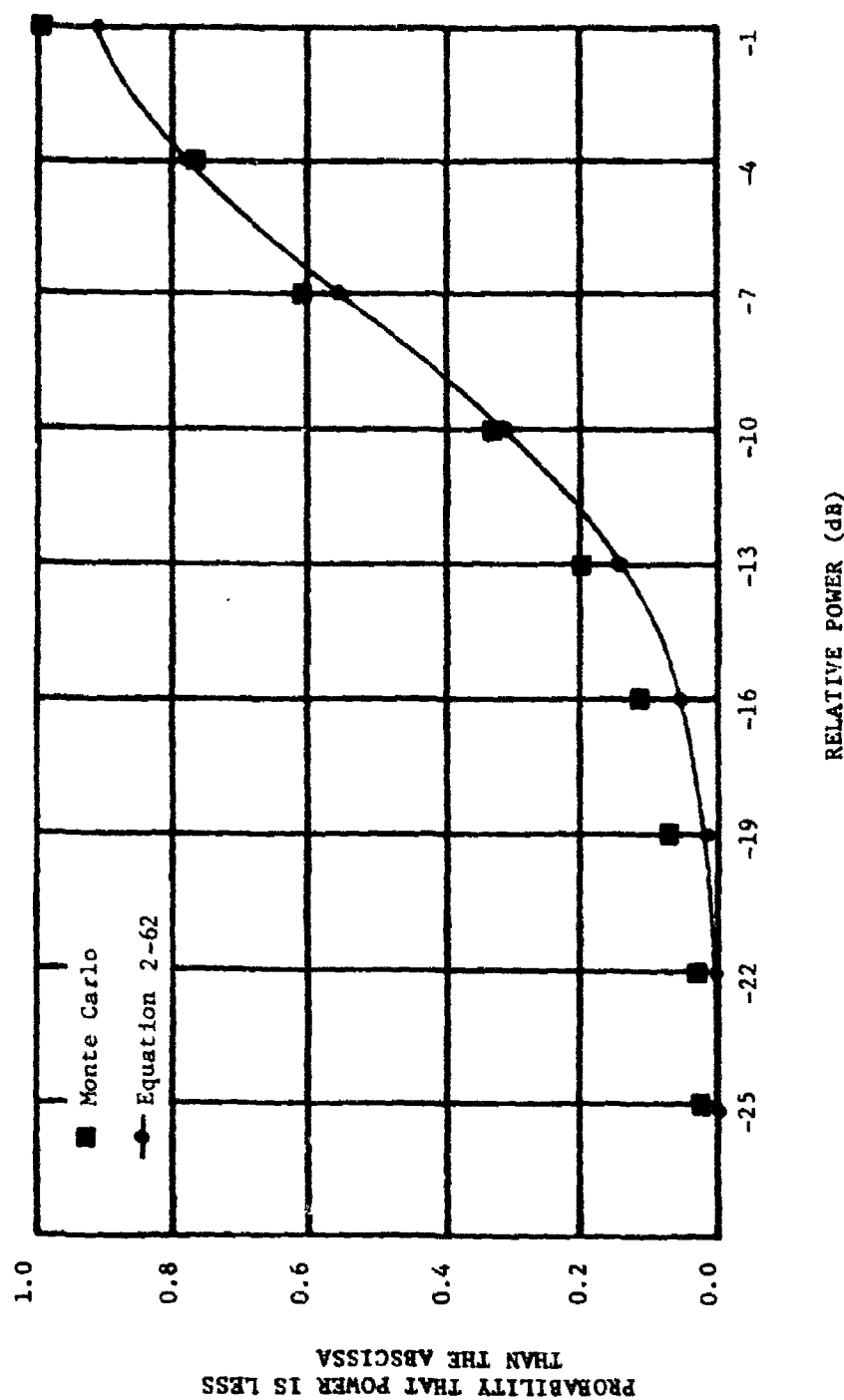


Figure 2-22 . Cumulative probability distribution for the radiated power density of a low sidelobe for a 9-element array with uncorrelated voltage sources.

The power density  $P(t, \phi)$  is then computed as  $E^*(t, \phi) \cdot E(t, \phi)$  and is written explicitly as the double sum

$$P(t, \phi) = \sum_{n'} \sum_n E^*(\omega_{n'}, \phi) E(\omega_n, \phi) \exp [j(\omega_{n'} - \omega_n)t] \quad (2-68)$$

The time domain behavior of a pulsed stochastic antenna system can be obtained with the aid of the preceding frequency-domain equations and the Fourier transform with respect to frequency. In particular, the time dependent statistical average complex far-field electric field may be written as

$$\langle E(t, \phi) \rangle = \frac{1}{2\pi} \sum_n \langle E(\omega_n, \phi) \rangle \exp [j\omega_n t] \quad (2-69)$$

In analogy with the techniques described previously for computing average power density, the statistical average time dependent power density is written as

$$\begin{aligned} \langle P(t, \phi) \rangle &= \langle E^*(t, \phi) \rangle \cdot \langle E(t, \phi) \rangle \\ &+ \sum_n \xi_n^2 + \sum_{n'} \sum_n \xi_{n'} \xi_n R_{n'n}(\omega) \exp [j(\omega_{n'} - \omega_n)t], \\ &\quad (n' \neq n) \end{aligned} \quad (2-70)$$

where  $\xi_n$  = standard deviation of  $E(\omega_n, \phi)$ ,

$\xi_{n'}$  = standard deviation of  $E^*(\omega_{n'}, \phi)$ , and

$R_{n'n}(\omega)$  = cross-correlation function of  $E(\omega_n, \phi)$  and  $E^*(\omega_{n'}, \phi)$ .

The cross-correlation function  $R_{n'n}(\omega)$  appearing here is not a time correlation function but rather is a frequency-dependent correlation function for the electric field and its conjugate at different unless the radiating system contains non-linear devices that have pronounced hysteresis or contains devices whose characteristic response time is commensurate with the input pulse width.

The p.d.f.  $f\{P(t, \phi)\}$  of the time domain power density  $P(t, \phi)$  is the Nakagami p.d.f. when the field and its conjugate at different frequencies are uncorrelated. This can be deduced at once by recognizing that the real and imaginary parts of the electric field  $E(t, \phi)$  each consist only of sums of statistically independent terms when the  $R_{n,n}$  are zero. The input parameters for the Nakagami p.d.f. are the average values of the real and imaginary parts of  $E(t, \phi)$ , their standard deviations, and the correlation coefficient for the real and imaginary parts of  $E(t, \phi)$ . The correlation coefficient for the real and imaginary parts of  $E(t, \phi)$  is, of course, non-zero even when the frequency cross correlation coefficients  $R_{n,n}$  are zero.

A numerical simulation of the pulse distortion suffered by a rectangular pulse radiated by a reflector antenna for both in-band and out-of-band frequencies for deterministic conditions is presented and discussed in Section V.

### SECTION III

#### NEAR-FIELD ANTENNA-ANTENNA COUPLING

##### A. Introduction

An exact analysis of the coupling between real-world cosited antennas would be extremely difficult or perhaps impossible to achieve. Accordingly, the efforts on this task were devoted to deriving approximate but accurate coupling prediction equations. Three different techniques for coupling analysis were considered. These three techniques are denoted respectively as (1) Plane Wave Spectrum (PWS), (2) Spherical Spectrum Wave (SWS), and (3) the Geometrical Theory of Diffraction (GTD). Most of the research efforts were devoted toward development of the PWS technique. Multiple scattering effects are not addressed in the analysis. However, multiple scattering effects can be approximately analyzed if the scattering matrix of each antenna is specified from theory or measurements. Theory and equations for the PWS and SWS approaches are presented and discussed in Subsection B and C, respectively. Some results of numerical simulations for PWS approach are also presented in Subsection B. The GTD technique for deterministic antenna analysis has been adapted to yield comparatively simple equations for certain classes of antenna coupling problems. Discussions of the GTD technique are contained in subsection D.

The analyses presented in this section were conducted in the frequency domain. The primary goal was to obtain equations valid over wide frequency bandwidths. The time domain response can then be obtained by numerically computing the Fourier Transform of the frequency domain equations. The wideband frequency response of swept CW radiating systems can be characterized by numerically computing the frequency-averaged pattern and standard deviation, as described in the previous section.

##### B. PWS Analysis

The general plane wave spectrum scattering matrix theory was originally formulated to treat antenna coupling problems and it is well documented in Reference [21]. The theory and equations are directly

applicable to antenna coupling situations shown in Figure 3-1 where one antenna is in the forward half-plane of the other antenna and the relative rotation angles  $\alpha$  and  $\beta$  defined in Figure 3-2 are less than about 70 degrees in magnitude. The application of the PWS analysis to other arrangements that do not obey these criteria depends on the ability to select suitably "canted" reference planes with appropriate spatial filters. This is a recommended area for future research. The PWS analysis for the canonical situation depicted in Figure 3-1 is discussed in the following paragraphs.

The complex voltage  $V(R, \alpha_p, \beta_q)$  induced in Antenna B when illuminated by Antenna A is derived from PWS analysis as

$$V(\bar{R}, \alpha_p, \beta_q) = c_0 \sum_m \sum_n \bar{A}(k_{ym}, k_{zn}) \cdot \bar{B}(k_{ym} - \zeta_{yp}, k_{zn} - \zeta_{zq}) \cdot \exp[-j\bar{k}_{mn} \cdot \bar{R}] \quad (3-1)$$

where

$A(k_{ym}, k_{zn})$  = transverse vectorial plane wave spectra of Antenna A,

$B(k_{ym} - \zeta_{yp}, k_{zn} - \zeta_{zq})$  = shifted transverse vectorial plane wave spectra of Antenna B,

$k_{ym}$  =  $m$ th value of  $k_y$  in the range  $-k_0 \leq k_y \leq k_0$ ,

$k_{zn}$  =  $n$ th value of  $k_z$  in the range  $-k_0 \leq k_z \leq k_0$ ,

$\zeta_{yp} = k_0 \sin(\alpha_p)$ , evaluated at the specified azimuth rotation angle  $\alpha_p$ ,

$\zeta_{zq} = k_0 \sin(\beta_q)$ , evaluated at the specified elevation rotation angle  $\beta_q$ ,

$\bar{k}_{mn} = k_{xmn} \hat{x} + k_{ym} \hat{y} + k_{zn} \hat{z}$ , where  $k_{xmn} = (k_0^2 - k_{ym}^2 - k_{zn}^2)^{1/2}$

and the  $\hat{x}$ ,  $\hat{y}$  and  $\hat{z}$  are unit vectors,

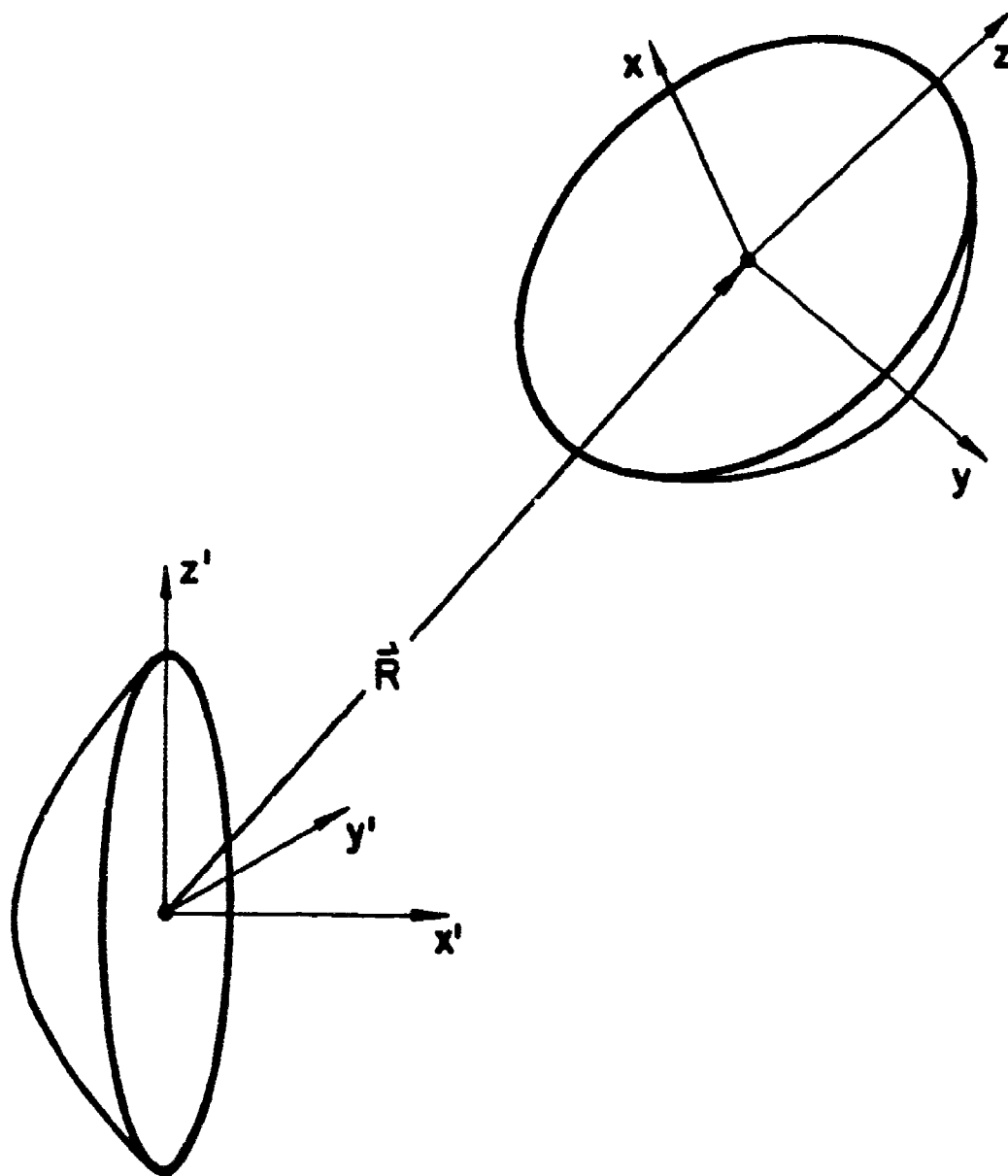


Figure 3-1. Sketch depicting the arrangement of two antennas appropriate for the PWS analysis of coupling.

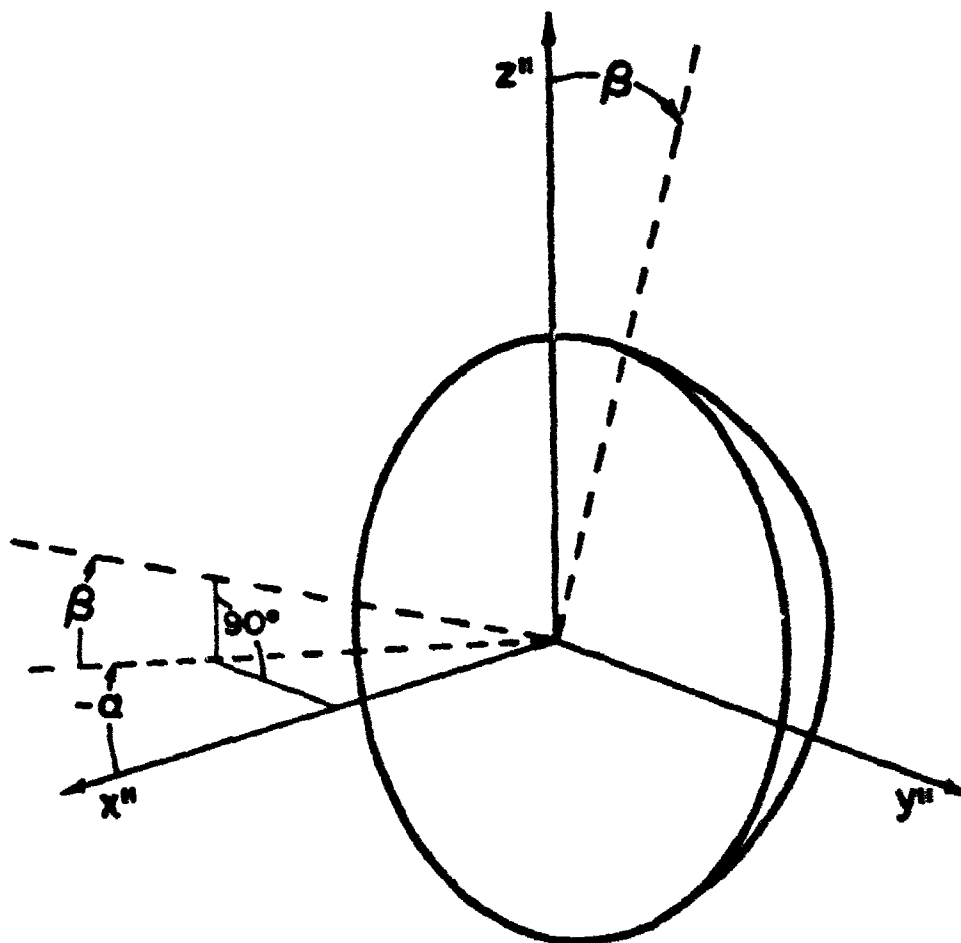


Figure 3-2. Sketch depicting the azimuth rotation angle  $-\alpha$  and the elevation rotation angle  $\beta$  associated with Antenna B of Figure 1.



$\bar{R} = X \hat{x} + Y \hat{y} + Z \hat{z}$  where X, Y, and Z are the cartesian coordinates of the center of rotation of Antenna B relative to the center of rotation of Antenna A, and

$c_0$  = a frequency-dependent proportionality factor.

The proportionality factor  $c_0$  is independent of antenna arrangements and orientations and will be suppressed in the remaining equations. The power coupled in Antenna B is

$$P(\bar{R}, \alpha_p, \beta_q) = |V(\bar{R}, \alpha_p, \beta_q)|^2 \cdot [(0.5) \cdot \Gamma_r] \quad (3-2)$$

where  $\Gamma_r$  is the real part of the complex admittance at the output port.

The PWS of Antenna A may be expressed in terms of the propagating modes in the waveguide feed as

$$\bar{A}(k_{ym}, k_{zn}) = \sum_{\ell} \sum_{\kappa} \sum_{\mu} a_{\mu} T(\zeta_{\ell\kappa}) \bar{H}_{\mu}(\zeta_{\ell\kappa}) \exp[-j(k_{ym} Y_{\ell} + k_{zn} Z_{\kappa})] \quad (3-3)$$

where

$a_{\mu}$  = the complex excitation coefficient of the  $\mu$ th waveguide propagating mode,

$T(\zeta_{\ell\kappa})$  = optical transform, computed as  $(1/2) \cdot [1 + \cos(\zeta_{\ell\kappa})]$ ,

$\bar{H}_{\mu}(\zeta_{\ell\kappa})$  = the far-field vectorial pattern of the feed horn when only the  $\mu$ th mode propagates,

$Y_{\ell}, Z_{\kappa}$  = points on the reflector aperture.

The angle  $\zeta_{\ell\kappa}$  and the reflector aperture coordinates are depicted in Figure 3-3. Equation (3-3) can be rewritten as the sum of the reflector transverse vectorial spectra  $\bar{A}_{\mu}(k_{ym}, k_{zn})$ ,

$$\bar{A}(k_{ym}, k_{zn}) = \sum_{\mu} a_{\mu} \bar{A}_{\mu}(k_{ym}, k_{zn}) \quad (3-4)$$

The corresponding equations for the PWS of Antenna B are

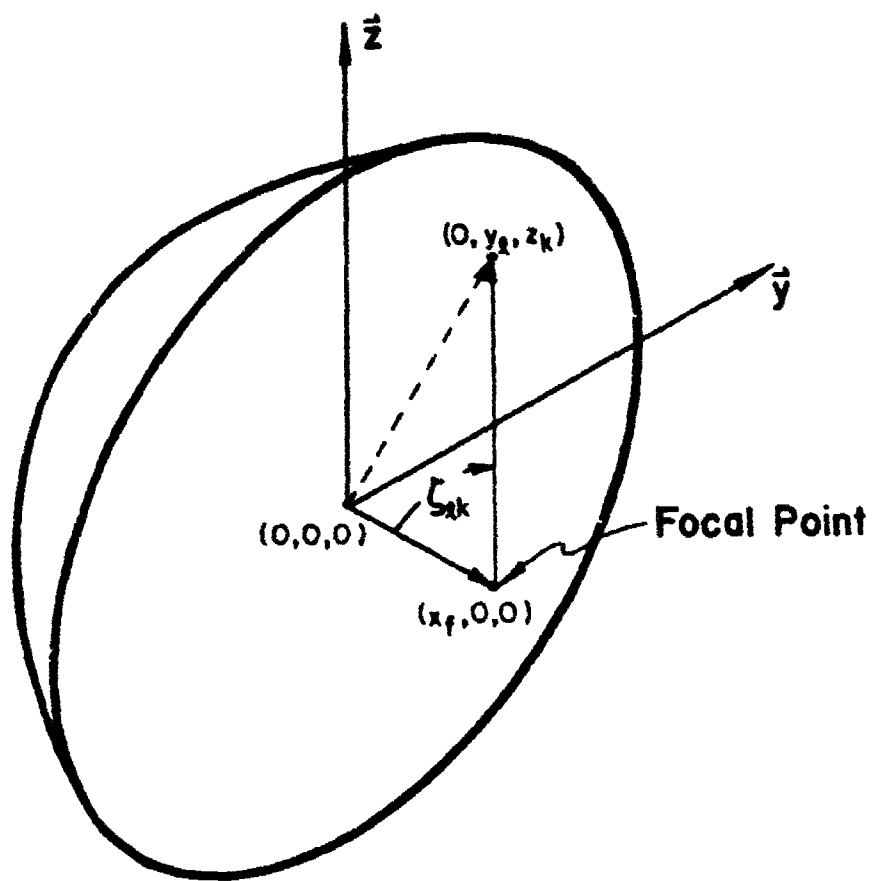


Figure 3-3. Sketch depicting the antenna aperture coordinates  $y_k, z_k$  and the optical transform angle  $\zeta_{fk}$ .

$$\bar{B}(k_{ym}, k_{zn}) = \sum_{\ell} Y_{\ell} \sum_{\mu} b_{\mu} T(\ell_{\ell\kappa}) \bar{H}(\ell_{\ell\kappa}) \exp[-j(k_{ym} Y_{\ell} + k_{zn} Z_{\ell\kappa})] \text{ and } (3-5)$$

the alternative form,

$$\bar{B}(k_{ym}, k_{zn}) = \sum_{\mu} b_{\mu} \bar{B}_{\mu}(k_{ym}, k_{zn}) \quad (3-6)$$

where

$b_{\mu}$  = the complex excitation coefficient of the  $\mu^{\text{th}}$  waveguide propagating mode, and

all other symbols are as previously defined.

The equation for the statistical average power  $P(\bar{R}, \alpha_p, \beta_q)$  coupled to Antenna B when illuminated by Antenna A is derived as

$$\begin{aligned} \langle P(\bar{R}, \alpha_p, \beta_q) \rangle &= \sum_m \sum_n \sum_m \sum_n \sum_{\mu} \sum_{\mu} \left\{ \left[ \langle a_{\mu}^* \rangle \langle a_{\mu} \rangle + C_{\mu, \mu}^a \right] \left[ \langle b_{\mu}^* \rangle \langle b_{\mu} \rangle + C_{\mu, \mu}^b \right] \right. \\ &\quad \times \bar{A}_{\mu}^*(k_{ym}, k_{zn}) \cdot \bar{B}_{\mu}^*(k_{ym}, -k_{yp}, k_{zn}, -k_{zq}) \exp \left[ j \bar{k}_{m'n'} \cdot \bar{R} \right] \\ &\quad \left. \times \bar{A}_{\mu}(k_{ym}, k_{zn}) \cdot \bar{B}_{\mu}(k_{yn} - k_{yp}, k_{zn} - k_{zq}) \exp \left[ -j \bar{k}_{mn} \cdot \bar{R} \right] \right\} \end{aligned} \quad (3-7)$$

where the statistical quantities are defined as

$\langle a_{\mu} \rangle$  = average value of the complex mode excitation coefficient  $a_{\mu}$ ,

$\langle b_{\mu} \rangle$  = average value of the complex mode excitation coefficient  $b_{\mu}$ ,

$C_{\mu, \mu}^a$  = covariance function for  $a_{\mu}^*$  and  $a_{\mu}$ , and

$C_{\mu, \mu}^b$  = covariance function of  $b_{\mu}^*$  and  $b_{\mu}$ .

The wavevector  $\bar{k}_{mn}$  is defined as  $\bar{k}_{mn} = k_{xm} \hat{x} + k_{yn} \hat{y} + k_{zn} \hat{z}$ . Similarly,  $\bar{k}_{m'n'}$  is defined as  $\bar{k}_{m'n'} = k_{xm'n'} \hat{x} + k_{ym'n'} \hat{y} + k_{zn} \hat{z}$ .

Numerical simulations were conducted to compute the power coupled between a pair of cosited antennas. The antenna arrangement is shown in Figure 3-4. Antenna B is displaced a longitudinal distance X and lateral distance Y from Antenna A. The antennas are not displaced in the vertical Z direction. The power coupled to Antenna B versus the rotation angle was computed for selected values of x and y for rotation angles in the range -30 degrees to +30 degrees. Only the azimuth Plane Wave Spectrums of the antennas were used in the calculations.

The apertures of Antenna A and Antenna B are 24 inches and 48 inches, respectively. The antennas are fed by WR-187 waveguide whose cutoff frequency for the TE<sub>20</sub> mode is 6.309 GHz. The in-band operating frequency of each antenna is 5.5 GHz. Calculations were made for the in-band frequency of 5.5 GHz and the out-of-band frequency of 6.5 GHz. The power flow in each waveguide feed is entirely in the TE<sub>10</sub> mode at 5.5 GHz. The TE<sub>10</sub> and TE<sub>20</sub> modes can both propagate at 6.5 GHz.

Antenna coupling can be conveniently described in terms of the mutual gain M(R, α) relative to a pair of isotropic radiators. M(R, α) is computed as

$$M(\bar{R}, \alpha) = \left( \frac{4\pi R}{\lambda} \right)^2 \frac{P(\bar{R}, \alpha)}{P_a}, \quad (3-8)$$

where  $\lambda$  is the operating wavelength and  $P_a$  is the power input to Antenna A. For the purpose of this study, a power transfer efficiency factor of 1.0 is assumed for Antenna A and, hence, the total power radiated by Antenna A is assumed to equal the input power.

The in-band, far-field antenna patterns of Antenna A and Antenna B are plotted in Figures 3-5 and 3-6, respectively. The estimated theoretical gain relative to an isotropic radiator is indicated at the top of each plot. The antennas were regarded as linear apertures with an "aperture efficiency" of 0.9 relative to comparable uniformly illuminated apertures for purposes of estimating the gain.

Out-of-band antenna patterns for the two antennas are shown in Figures 3-7 and 3-8. Figure 3-7 shows the out-of-band pattern for Antenna A for equal power flow in both modes with the phase of the TE<sub>20</sub> mode +35°

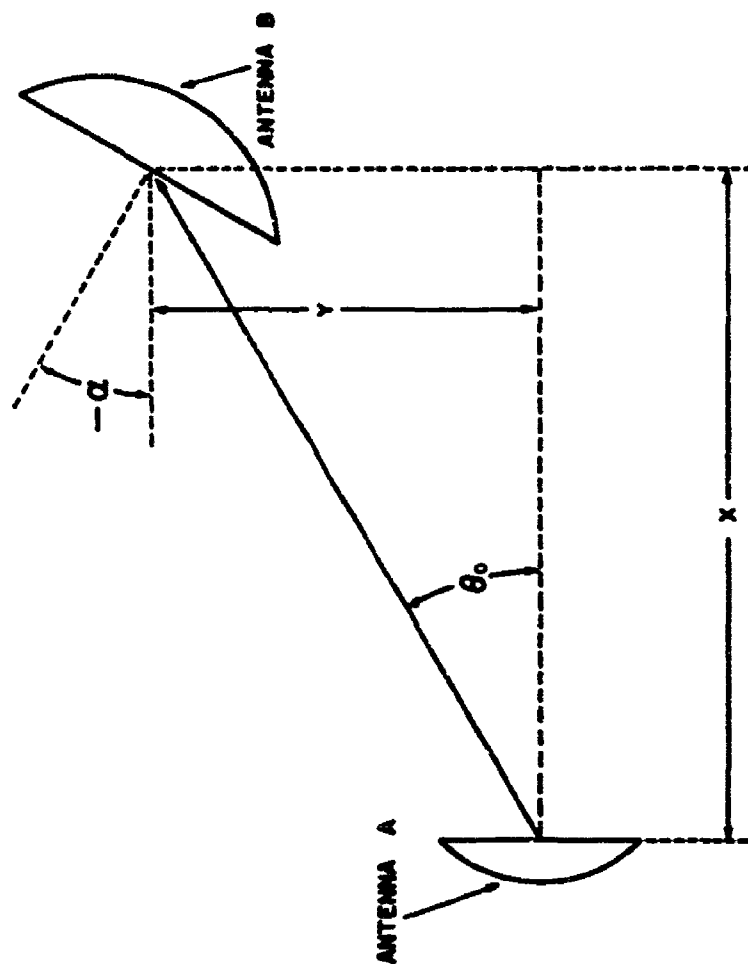


Figure 3-4. Sketch of the near-field arrangement of Antenna A and Antenna B used in the numerical simulations.

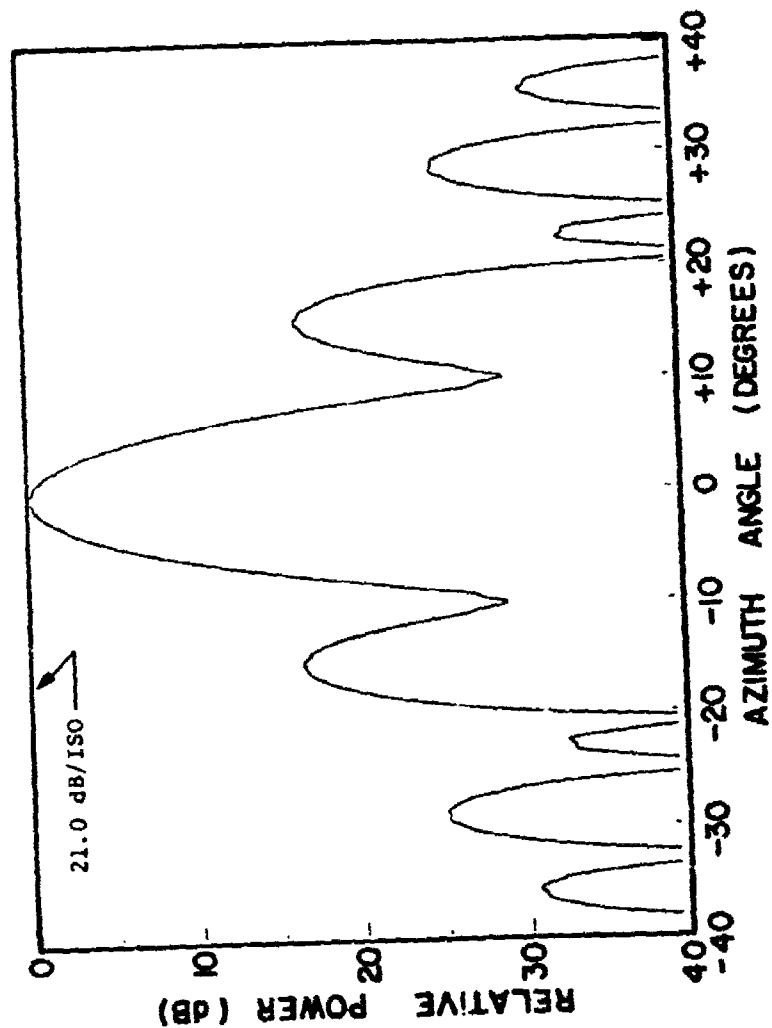


Figure 3-5. Far-field antenna pattern for Antenna A at the in-band frequency of 5.5 GHz for waveguide feed power flow entirely in the  $TE_{10}$  mode.

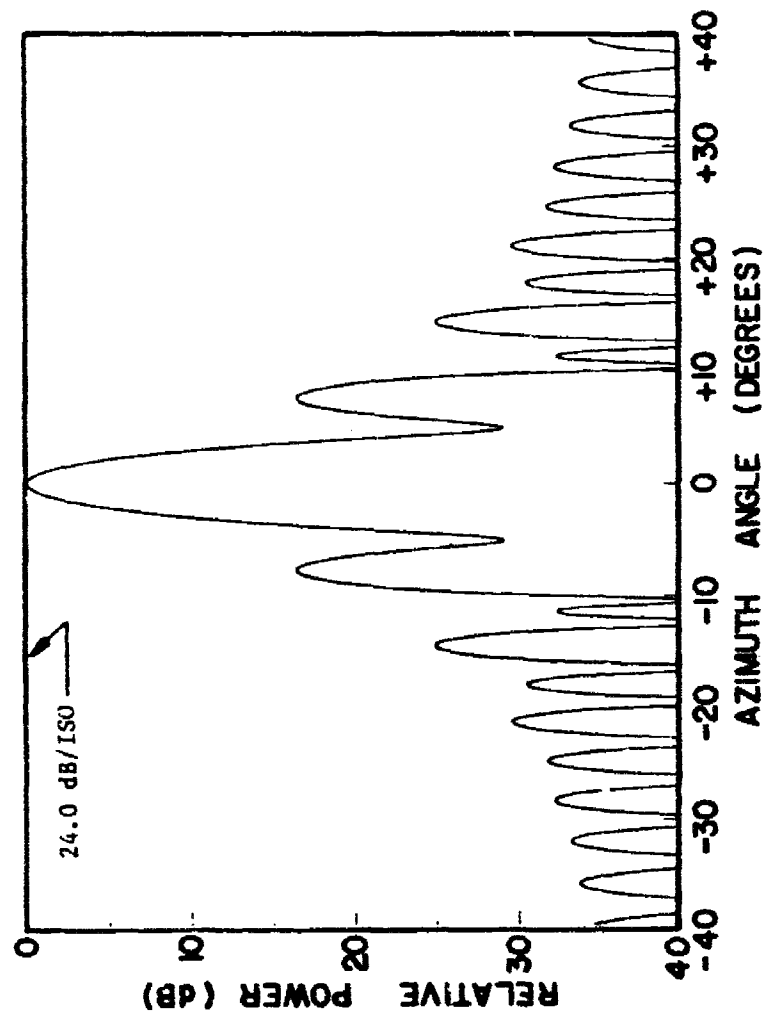


Figure 3-6. Far-field antenna pattern for Antenna B at the in-band frequency of 5.5 GHz for waveguide feed power flow entirely in the  $TE_{10}$  mode.

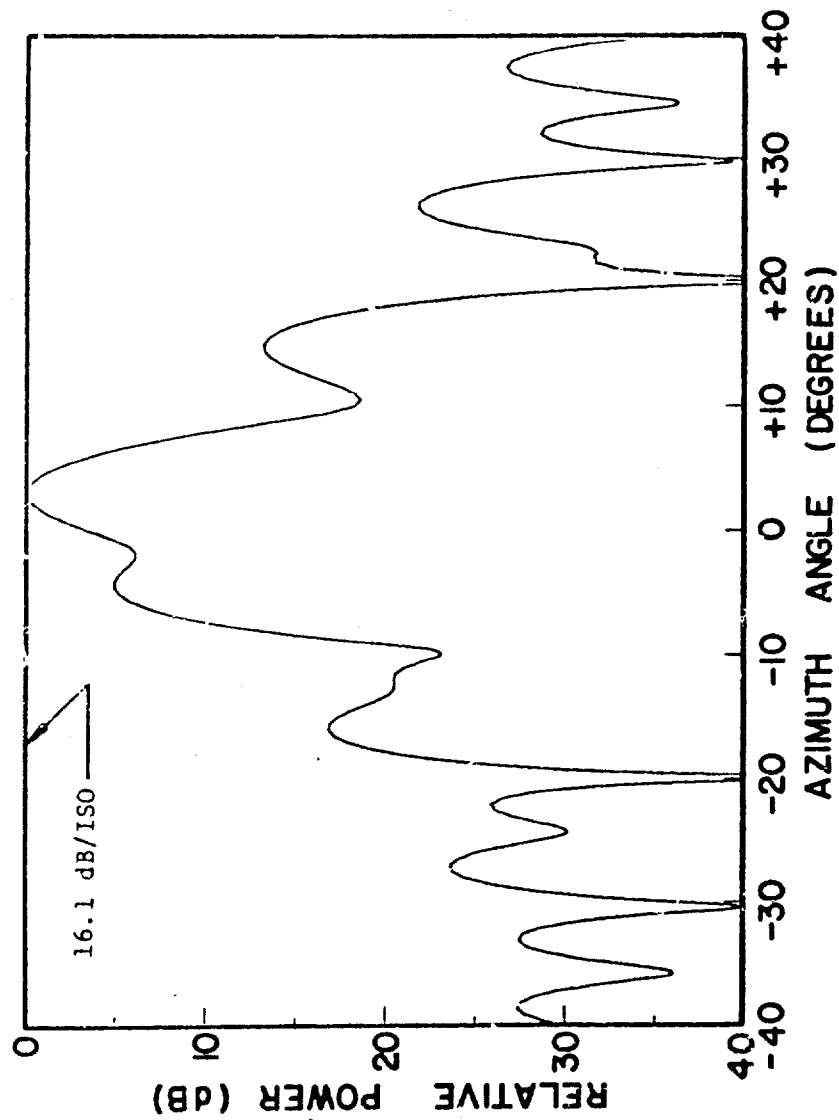


Figure 3-7. Far-field antenna pattern for Antenna A at the out-of-band frequency of 6.5 GHz for equal waveguide power flow in the  $TE_{10}$  and  $TE_{20}$  modes with relative phase angle of 35 degrees.



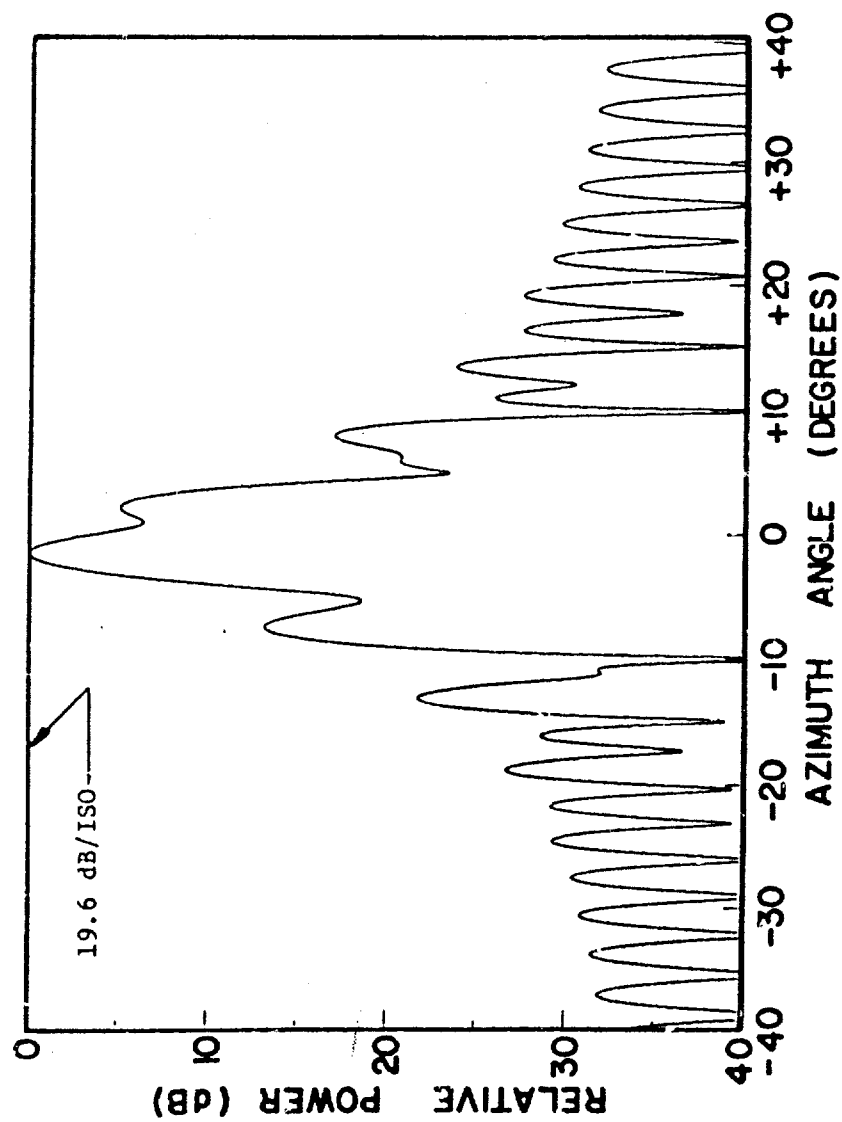


Figure 3-8. Far-field antenna pattern for Antenna B at the cut-of-band frequency of 6.5 GHz for equal waveguide power flow in the  $TE_{10}$  and  $TE_{20}$  modes with relative phase angle of -50 degrees.

relative to the  $TE_{10}$  mode. Similarly, Figure 3-8 shows the out-of-band pattern for Antenna B for equal power flow in both modes with the phase of the  $TE_{20}$  mode  $-50^\circ$  relative to the  $TE_{10}$  mode.

The in-band to in-band mutual gain of the antenna pair is shown in Figures 3-9 and 3-10. Each figure shows a plot of the mutual gain expressed in decibels versus the rotation angle  $\alpha$  in degrees for the indicated values of longitudinal separation distance  $X$  and transverse separation distance  $Y$ . The mutual gain relative to a pair of isotropic antennas is displayed at the top of each plot.

The out-of-band to out-of-band mutual gain of the antenna pair is shown in Figure 3-11 for the indicated out-of-phase modal propagation for the longitudinal separation distance of 20 feet and lateral displacement of 5 feet.

Two general trends common to the in-band to in-band and the out-of-band to out-of-band situations may be discerned from inspection of the plots shown in Figures 3-9 through 3-11 and from additional plots contained in Reference [5]. First, the peak value of the mutual gain decreases with increasing lateral displacements for a fixed longitudinal displacement. Second, the peak value of the mutual gain increases with increasing longitudinal displacement for a fixed lateral displacement. Both of these trends are consistent with theory. However, the peak mutual gain may exhibit "peaks" and "valleys" if the computation were made for a "finely-grained" set of coordinates. Nevertheless, the "envelope" of the peak mutual gain would exhibit the cited trends.

The peak mutual gain for the in-band to in-band situations always occurs at, or very near to, the rotation angle at which Antenna B points at the center of Antenna A, whereas the peak mutual gain for the out-of-band to out-of-band situations is shifted a few degrees. The direction and magnitude of the angular shift depends on the mode excitation in the feeds of the two antennas. The magnitude of the peak mutual gain also varies with mode excitations. All of these trends are consistent with theory in the sense of "coarse-grained" behavior mentioned previously.

Next, consider the situation depicted in Figure 3-12 where the transmitting antenna illuminates a cylindrical obstacle located between the transmitting and receiving antennas. In order to determine the effect of

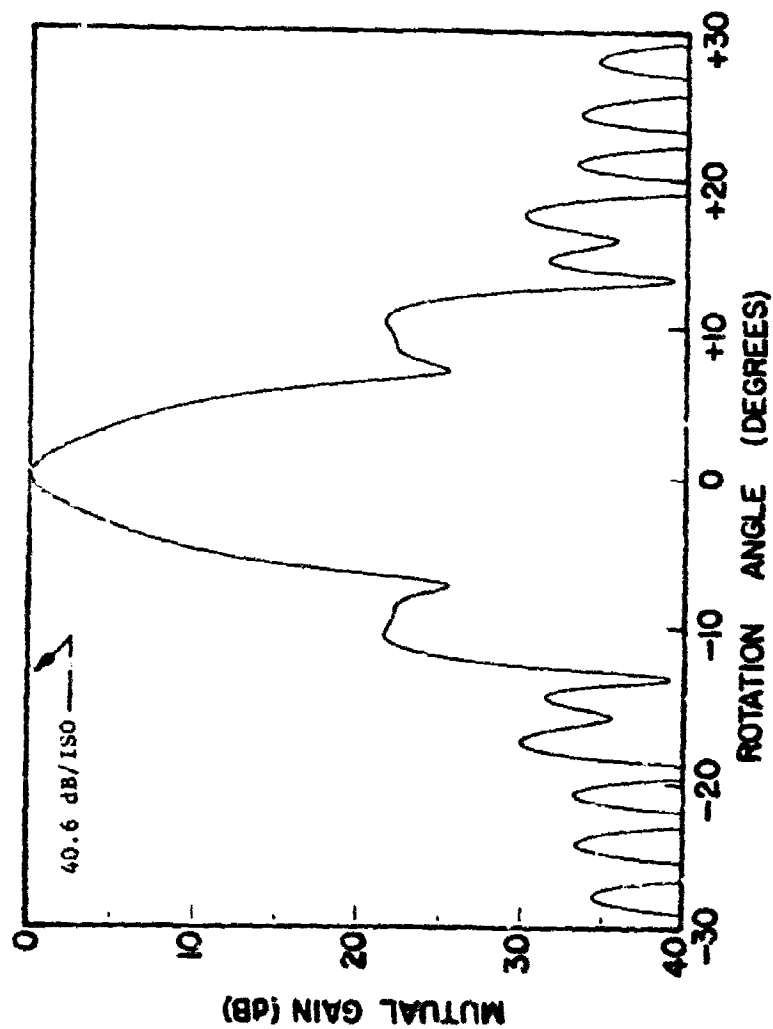


Figure 3-9. Mutual Gain versus rotation angle for both antennas operating in-band at 5.5 GHz for waveguide feed power flow entirely in the  $TE_{10}$  mode for the longitudinal separation distance  $X = 20$  feet and the transverse separation distance  $Y = 0$  feet.

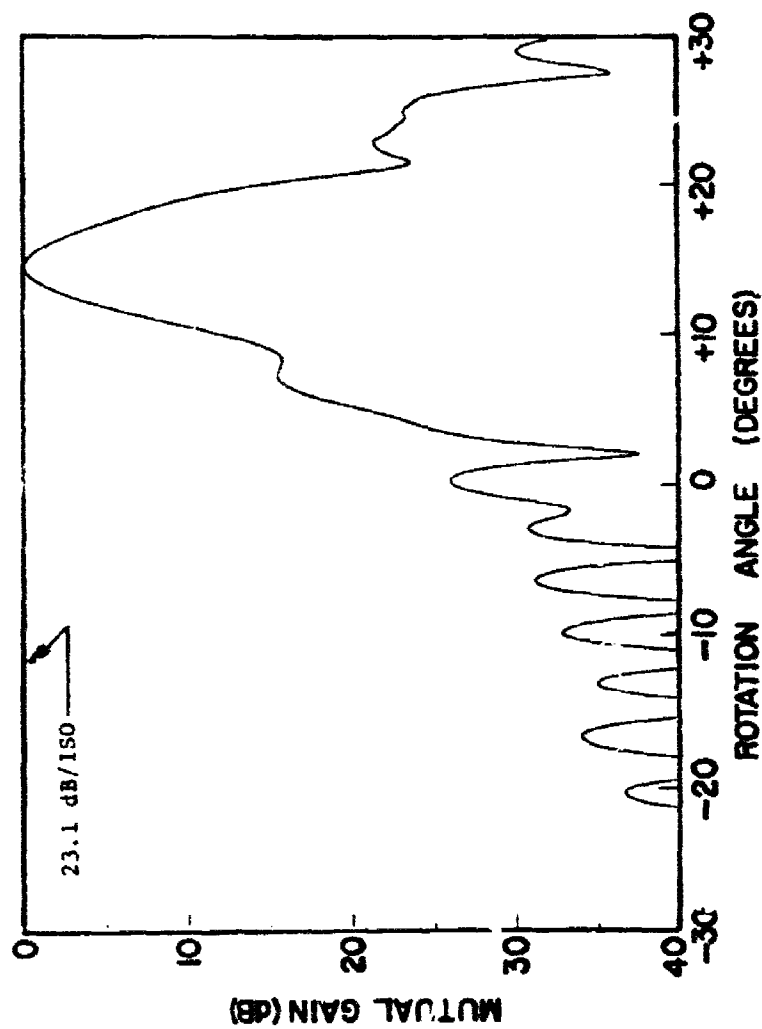


Figure 3-10. Mutual Gain versus rotation angle for both antennas operating in-band at 5.5 GHz for waveguide feed power flow entirely in the  $TE_{10}$  mode for the longitudinal separation distance  $X = 20$  feet and the transverse separation distance  $Y = 5$  feet.

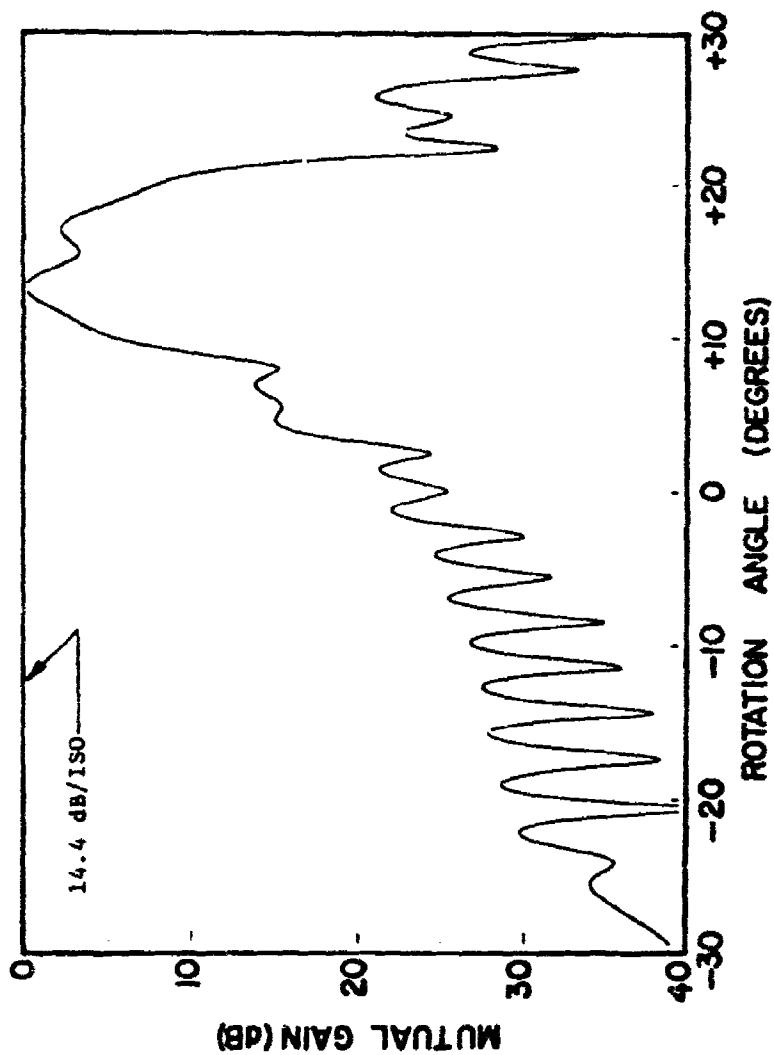


Figure 3-11. Mutual Gain versus rotation angle for both antennas operating out-of-band at 6.5 GHz for equal waveguide feed power flow in the  $TE_{10}$  and  $TE_{20}$  modes with relative phase of 35 degrees for Antenna A and -50 degrees for Antenna B for the longitudinal separation distance  $X = 20$  feet and the transverse separation distance  $Y = 5$  feet.

the interposed obstacle on the antenna coupling the total transverse spectrum for the transmitting antenna and the obstacle which is incident upon the receiving antenna must be determined. This calculation, which is fully described in References [21] and [22], is the basis for the evaluation of the far-field pattern degradation caused by the near-field obstacle. For the case of the interposed obstacle, the spectrum incident on the receiver is the sum of the transmitting antenna spectrum  $A(\bar{k})$  and the obstacle scattered spectrum  $A^s(\bar{k})$  given by Equation (5-8) of Section V. Assuming that the multiple reflection effects are negligible, the complex voltage response can be computed from Equation (3-1) by replacing the antenna spectrum  $A(\bar{k})$  with the composite spectrum

$$A_t(\bar{k}) = A(\bar{k}) + A_s(\bar{k}) e^{-jk_x X_c} \quad (3-9)$$

The method of computation of the integral is thus the same whether or not an obstacle is present. The only difference is whether the antenna spectrum  $A(\bar{k})$  or the sum of the antenna and obstacle scattered spectrum  $A_t(\bar{k})$  is employed for the computation.

The plane wave spectrum scattering analysis algorithm was used to construct a data file corresponding to the sum of the transmitting antenna and obstacle scattered spectra. A second data file is then loaded with the receiving antenna spectrum, and the transmission integral evaluation is performed.

Recall that, for a tall cylindrical obstacle, the scattering matrix element function in the vertical ( $\phi = \text{constant}$ ) plane is of the form  $\text{SIN}(Z)/(Z)$ . The antenna spectra in the vertical direction were also approximated by appropriately chosen functions of  $\text{SIN}(Z)/(Z)$  form. These functions were chosen to produce the correct 3-dB beamwidth for the test antennas. The computation can be further simplified if the coupling integral is performed only over the azimuth plane (i.e.,  $\theta = \pi/2$ ,  $k_y$  variable). This approximation is termed a "linear spectrum" approximation, and it was found that this approximation, for the cases considered herein, was a good approximation to the use of the complete  $(k_y, k_z)$  spectra. Thus the "linear spectrum" approximation was used to derive the antenna decoupling data.

Measured data for both 6-inch diameter and 24-inch diameter cylinders located between 48-inch diameter paraboloidal, vertically-polarized reflector antennas operating at 5.5 GHz were available from previous measurement programs [ 23 ]. Figure 3-12 shows the antenna/obstacle geometry. The calculated antenna decoupling caused by the interposed 6-inch and 24-inch diameter cylinders for antenna separation distances of 17-feet and 47-feet is shown in Figure 3-13. The term "decoupling" is defined as the ratio of the received voltage with the obstacle present to the received voltage with the obstacle absent. Thus, the decoupling represents the decrease in mutual coupling due to the interposed obstacle.

As shown in Figure 3-13, the calculated and measured results for both the 6-inch and 24-inch diameter cylinders for the 47-foot separation distance are in very good agreement with the average measured data. We note that the actual measured data exhibit a periodic oscillation about the average values presented herein due to multiple reflections between the obstacle and antenna. Since these reflections are not considered in the present analysis, it is appropriate to compare the calculations with these average data. The typical maximum/minimum bounds on the measured data deviate from the average values by approximately  $\pm 1.5$  dB and  $\pm 0.5$  dB for the 24-inch diameter and 6-inch diameter cylinders, respectively.

The calculated decoupling for the 17-foot separation distance for the 6-inch diameter cylinder is also in very good agreement with the measured data. However, the results for the 17-foot separation distance for the 24-inch diameter cylinder exceed the measured data by a few decibels due to the approximations that were made in the analysis.

Plots of the measured and computed mutual gain versus the azimuth pointing angle of the receiving antenna are shown in Figures 3-14(a) and 3-14(b). The mutual gain plots shown in Figure 3-14(b) were obtained with no obstacle present. The mutual gain plots shown in Figure 14(b) were obtained with a 12.0-foot tall, 2.0-foot diameter mast located midway between the two 4.0-foot diameter paraboloidal reflector antennas that were separated 17.0 feet apart. The computed data were obtained via Equations 3-1 and 3-8. The elevation patterns of the antennas were characterized in the approximate manner described previously, and multiple reflections were ignored. Nevertheless, good agreement between measured and

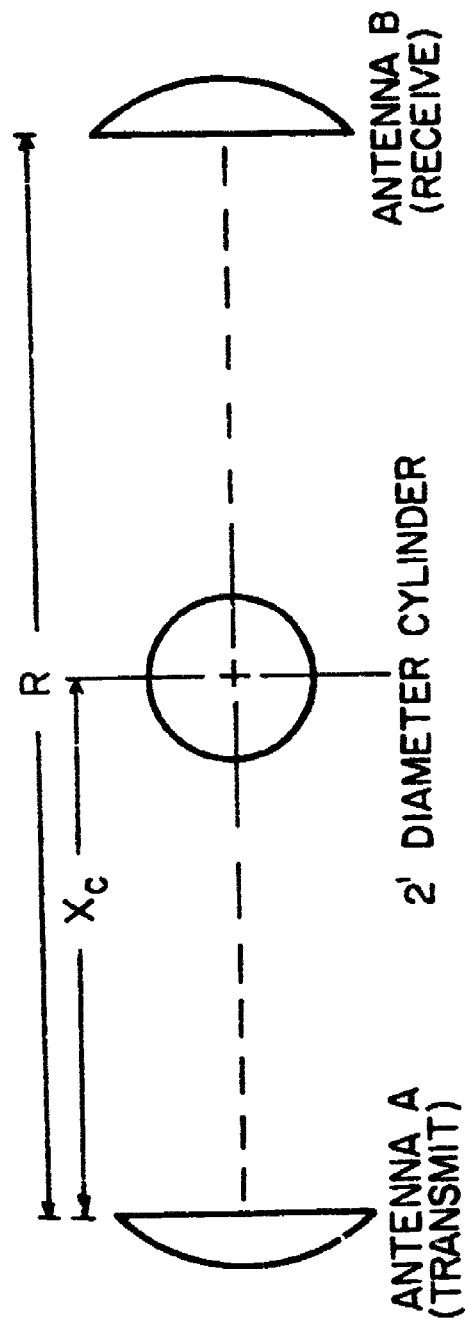


Figure 3-12. Antenna-to-Antenna coupling geometry with an interposed obstacle employed for the plane wave spectrum scattering analysis.



# 47 FOOT SEPARATION DISTANCE

— MEASURED

Δ COMPUTED-LINEAR SPECTRUM

# 17 FOOT SEPARATION DISTANCE

● MEASURED

○ COMPUTED-LINEAR SPECTRUM

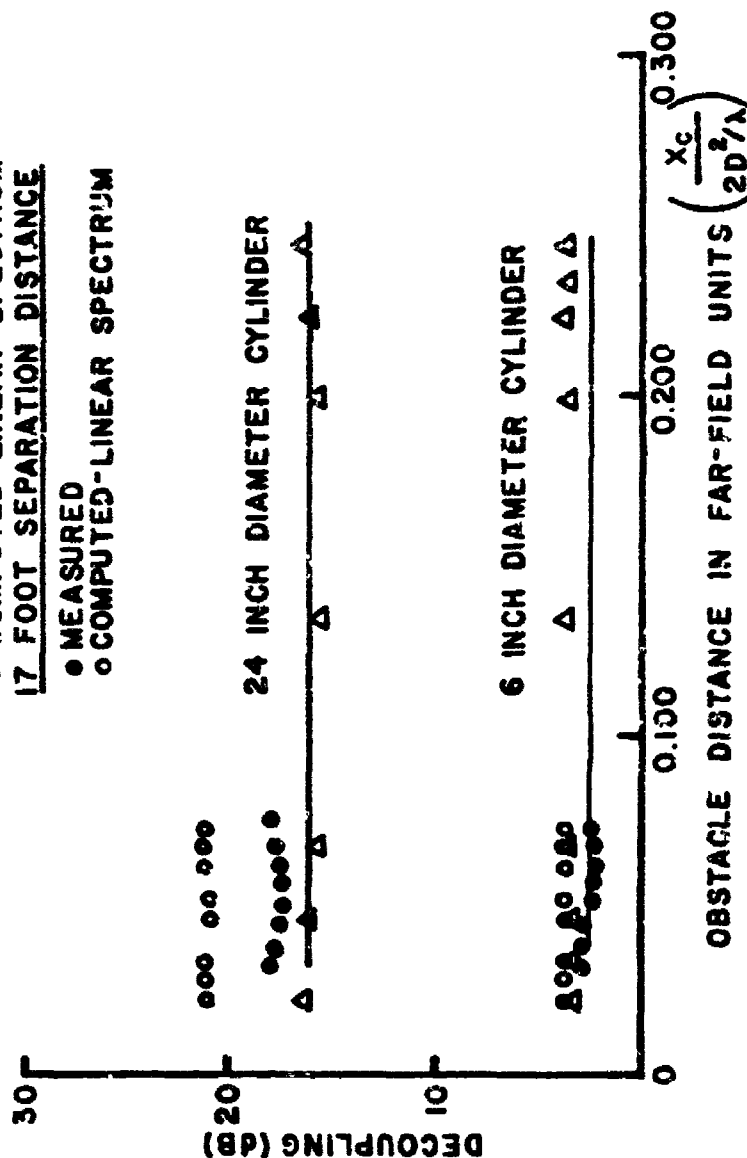


Figure 3-13. Mainbeam antenna decoupling caused by 24-inch and 6-inch diameter circular cylinders located on the boresight axis between two 48-inch diameter vertically-polarized paraboloidal antennas operating at 5.5 GHz.

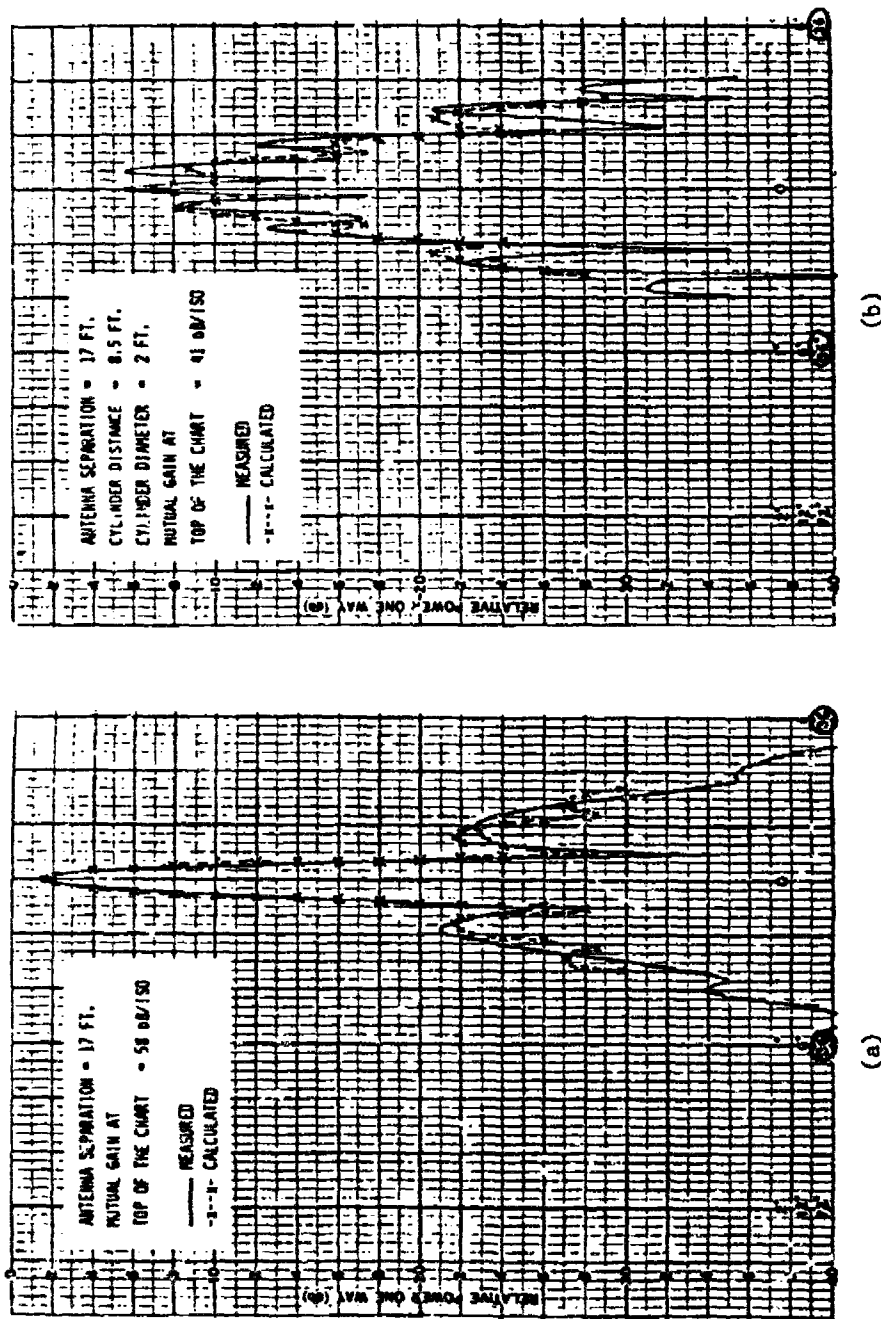


Figure 3-14. Measured and computed mutual gain versus azimuth rotation angle of the receiving antenna with (a) a clear site between the two antennas and (b) an intervening 12.0-foot tall, 2.0-foot diameter mast located midway ( $X=8.5$  feet) between the two antennas for the indicated antenna separation distance  $R=17.0$  feet, for vertically polarized signals at 5.5 GHz. The aperture diameter of each paraboloidal reflector antenna is 4.0 feet.

computed data is achieved for this sample situation as well as for situations involving cylindrical obstacles of 0.5-foot diameter and 4.0-foot diameter.

Application of the FWS equation to predict mutual coupling with an obstacle located between the two antennas shown in Figure 3-1 and displaced both vertically and laterally off the line joining the antenna rotation centers is well understood. The antenna/obstacle situation just described can be analyzed via existing equations. However, the application of FWS analysis to handle the effects of an intervening obstacle located between the two antennas depicted in Figure 3-15 or a non-intervening obstacle such as a common mounting pole to which two or more antennas are attached are areas where further research is needed.

### C. Spherical Wave Spectrum Coupling Analysis

The formulation of the SWS coupling analysis can be illustrated with the aid of the cosited antenna pair shown in Figure 3-15 and the antenna coordinate system depicted in Figure 3-16. The various symbols contained in Figures 3-15 and 3-16 are defined as

$\bar{R}$  = vector from center of Antenna A to center of Antenna B,

$\bar{R}'$  = vector from the center of Antenna A to a specified near-field point,

$\bar{R}-\bar{R}'$  = vector from the center of Antenna B to the specified near-field point,

$\alpha$  = azimuth rotation angle between Antenna A and Antenna B, and

$\beta$  = elevation rotation angle between Antenna A and Antenna B.

The complex voltage response  $V(\bar{R}, \beta, \alpha)$  of Antenna B when illuminated by Antenna A can be written as

$$V(\bar{R}, \beta, \alpha) = C_0 \cdot \int_{S'} \bar{E}^b(\bar{R}-\bar{R}') | \beta, \alpha \rangle \cdot \bar{E}^a(\bar{R}') dS' \quad (3-10)$$

where  $C_0$  is a frequency dependent factor and where  $\bar{E}^a$  and  $\bar{E}^b$  denote the complex near-field electric fields of Antenna A and Antenna B,

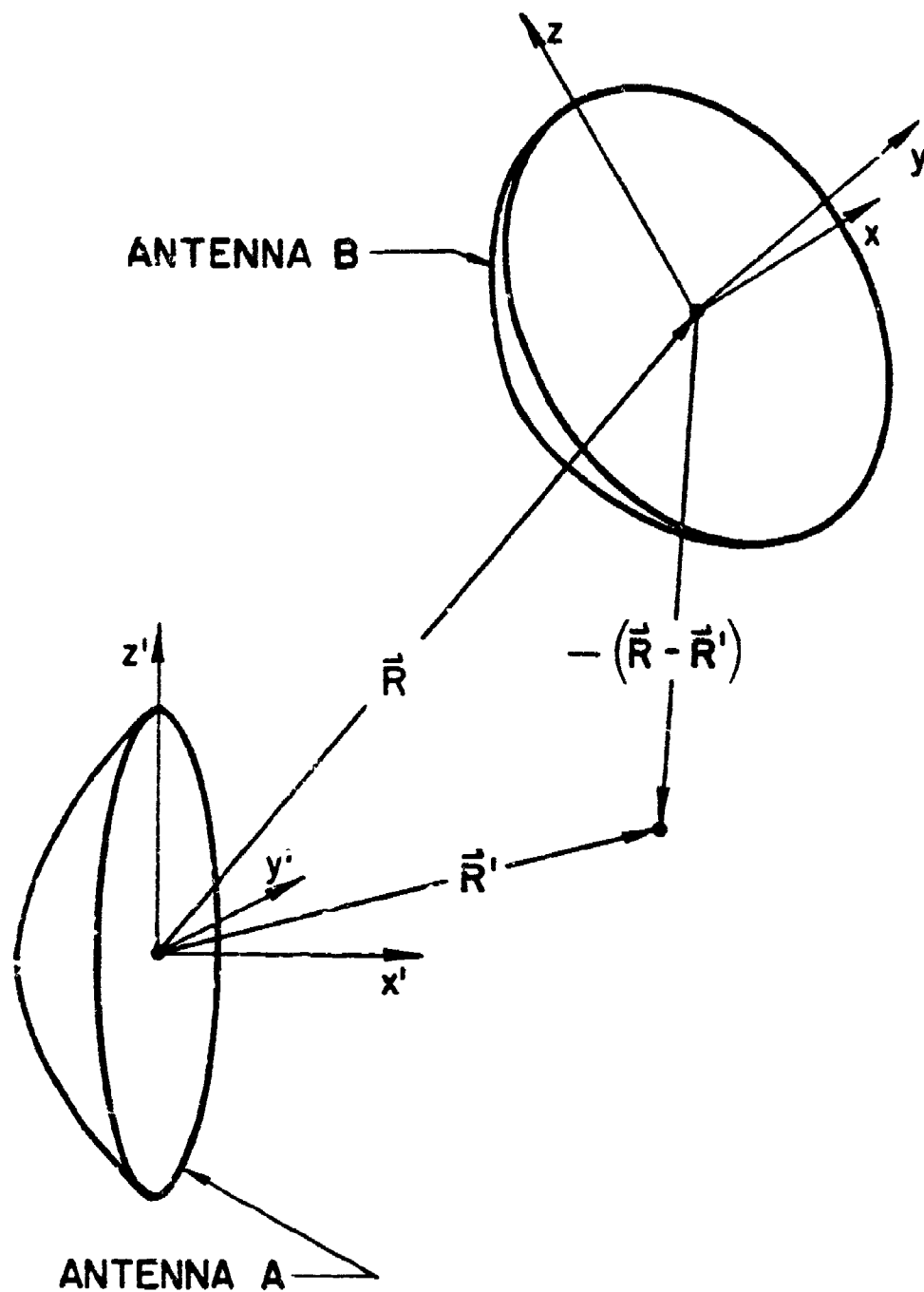


Figure C-15. Sketch depicting two arbitrarily oriented near-field antennas and geometric parameters.

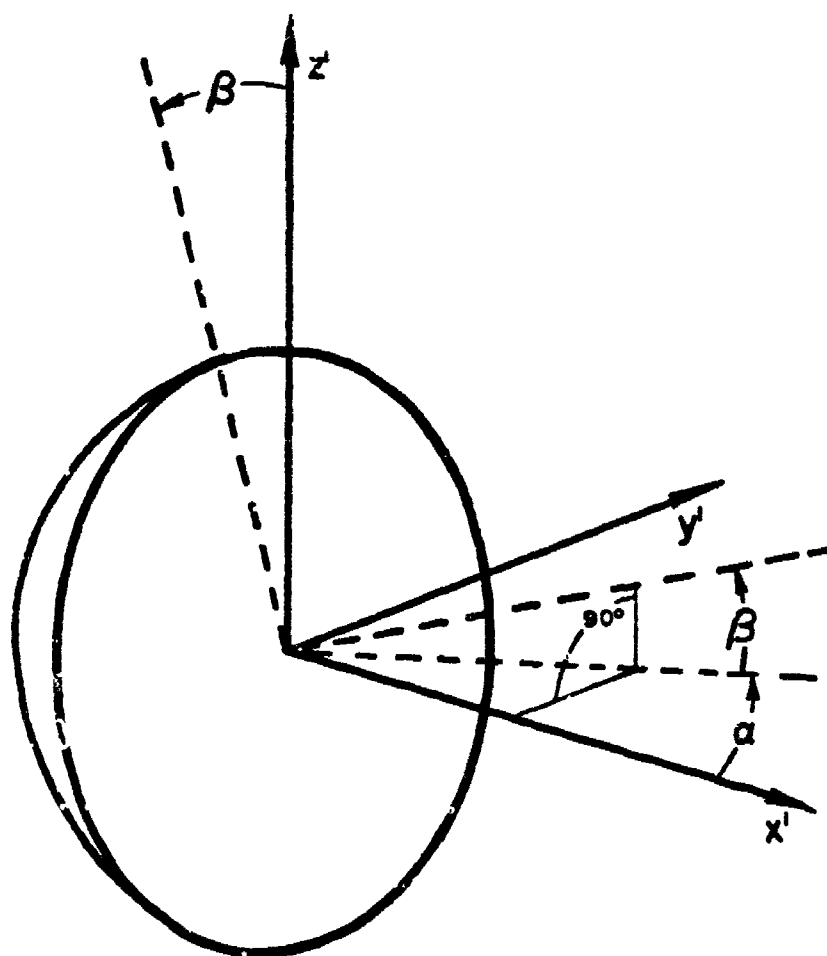


Figure 3-16. Sketch depicting the azimuth rotation angle  $\alpha$  and the elevation rotation angle  $\beta$  associated with Antenna B of Figure 2.

respectively. The surface integral in Equation (3-10) is integrated over the surface of the sphere of radius  $R'$ .

The vertically-polarized and horizontally polarized components of the electric field of Antenna A on the sphere of radius  $R'$  centered at Antenna A may be computed as

$$E_v^a(R', \theta', \phi') = \sum_m \sum_n A_{mn}^v h_n^{(2)}(KR') L_{nm}(\cos \theta') e^{-jm\phi'} \quad (3-11)$$

for vertical polarization and

$$E_h^a(R', \theta', \phi') = \sum_m \sum_n A_{mn}^h h_n^{(2)}(KR') L_{nm}(\cos \theta') e^{-jm\phi'} \quad (3-12)$$

for horizontal polarization. The symbol  $h_n^{(2)}$  denotes the spherical Hankel function of the second kind and order  $n$ , and the symbol  $L_{nm}$  denotes the associated Legendre polynomial of the first kind of order  $n$  and degree  $m$ . The coefficients  $A_{mn}^v$  and  $A_{mn}^h$  are readily computed if  $E_v^a$  is known on any spherical surface. It is assumed that the vertically-polarized and horizontally-polarized far-field patterns are known, and consequently, the coefficients can be computed from them. Equations analogous to Equations (3-11) and (3-12) can be written for the vertically-polarized and horizontally-polarized field of Antenna B, and a coordinate transformation can be applied to refer the fields of Antenna B to the Antenna coordinates or vice versa.

The power coupled into Antenna B due to illumination by Antenna A is then

$$P(\bar{R}, \beta, \alpha) = \left| \sum_m \sum_n \sum_{m'} \sum_{n'} \bar{A}_{nm} \cdot \bar{B}_{n'm'}^* I_{nm}(\bar{R}, \beta, \alpha) \right|^2 \quad (3-13)$$

where  $\bar{A} = A^v \hat{\theta} + A^h \hat{\phi}$  and  $\bar{B} = B^v \hat{\theta} + B^h \hat{\phi}$ . The coefficients  $\bar{A}$  and  $\bar{B}$  and the integral  $I(\bar{R}, \beta, \alpha)$  are computed as

$$\bar{A}_{nm} = \int_0^{2\pi} \int_0^\pi \bar{E}^a(\theta, \phi) L_{nm}(\cos \theta) e^{-jm\phi} \sin \theta d\theta d\phi, \quad (3-14)$$

$$\bar{B}_{n',n'} = \int_0^{2\pi} \int_0^\pi \bar{F}^b(\theta, \phi) L_{m',n'}(\cos\theta) e^{-jm'\phi} \sin\theta d\theta d\phi, \text{ and } (3-15)$$

$$I_{nm}(\bar{R}, \beta, \alpha) = R \int_0^{2\pi} \int_0^\pi h_n(KR') h_n(K|\bar{R}-\bar{R}'|) L_{nm}(\cos\theta') L_{n',m'}(\cos(\theta'-\alpha)) \\ e^{-jm(\phi'-\alpha)} \sin(\theta') d\theta' d\phi' . \quad (3-16)$$

The quantities  $\bar{F}^a(\theta, \phi)$  and  $\bar{F}^b(\theta, \phi)$  are the total vectorial angular spectra of Antennas A and B, respectively. These total spectra are just the sum of the vectorial spectra  $\bar{F}_\mu^a$  or  $\bar{F}_\mu^b$  for each propagating mode of the antenna feed system. Hence,

$$\bar{F}^a(\theta, \phi) = \sum_\mu a_\mu \bar{F}_\mu^a(\theta, \phi) \text{ and } (3-17)$$

$$\bar{F}^b(\theta, \phi) = \sum_\mu b_\mu \bar{F}_\mu^b(\theta, \phi) \quad (3-18)$$

where  $a_\mu$  and  $b_\mu$  denote complex excitation coefficients for the propagating waveguide modes.

The statistical average power is obtained in the straightforward but tedious procedure described previously. The resulting expression is

$$\sum_n \sum_m \sum_{n'} \sum_{m'} \sum_p \sum_q \sum_{p'} \sum_{q'} \langle \bar{A}_{nm} \cdot \bar{A}_{pq}^* \rangle \langle \bar{B}_{n'm'} \cdot \bar{B}_{p'q'}^* \rangle I_{nm}(\bar{R}, \beta, \alpha) I_{pq}(\bar{R}, \beta, \alpha) \\ I_{n'm'}(\bar{R}, \beta, \alpha) I_{p'q'}(\bar{R}, \beta, \alpha) \quad (3-19)$$

The joint statistical moment  $\langle \bar{A}_{nm} \cdot \bar{A}_{pq}^* \rangle$  is computed as

$$\langle \bar{A}_{nm} \cdot A_{pq}^* \rangle = \int_0^{2\pi} \int_0^\pi \int_0^{2\pi} \int_0^\pi \langle \bar{F}^a(\theta, \phi) \cdot \bar{F}^{a*}(\theta', \phi') \rangle L_{nm}(\cos\theta) L_{pq}(\cos\theta') \\ \times \exp[j(p-n)\phi] \sin(\theta) \sin(\theta') d\theta' d\phi' d\theta d\phi \quad (3-20)$$

and  $\langle \bar{B}_{n'm'} \cdot \bar{B}_{p'q'}^* \rangle$  is computed similarly. The joint statistical moment  $\langle \bar{F}^a(\theta, \phi) \cdot \bar{F}^a(\theta', \phi') \rangle$  is obtained from a knowledge of the waveguide modal coefficient excitation statistics, to wit:

$$\langle \bar{F}^a(\theta, \phi) \cdot \bar{F}^{a*}(\theta', \phi') \rangle = \sum_{\mu} \sum_{\mu'} \langle a_{\mu} a_{\mu'}^* \rangle \bar{F}_{\mu}^a(\theta, \phi) \bar{F}_{\mu'}^{a*}(\theta', \phi') \quad (3-21)$$

and similarly for  $\langle \bar{F}^b(\theta, \phi) \cdot \bar{F}^{b*}(\theta', \phi') \rangle$ .

Finally, the joint statistical moments  $\langle a_{\mu} a_{\mu'}^* \rangle$  and  $\langle b_{\mu} b_{\mu'}^* \rangle$  must be specified from theory or experiment. The deterministic analysis is, of course, recovered from the statistical equations in the limit of vanishing covariances  $C_{\mu, \mu'}$  for all indices  $\mu$  and  $\mu'$ .

The rigorous spherical wave spectrum analysis is considerably more involved than the plane wave spectrum analysis. However, the spherical wave spectrum technique has the very desirable attribute of being applicable to arbitrary arrangements and orientations of a near-field antenna pair. Nonetheless, computer run times may be excessive for routine use of the SWS technique in its present "rigorous" form. However, it appears that a substantial reduction in the computer run time may be achieved without seriously degrading the accuracy of the SWS analysis by deriving approximate series representations of the integrals via either the residue calculus or replacement of the full spherical wave series by asymptotic series. Moreover, it appears that



further theoretical and numerical studies of the SWS technique would expedite the development of valid PWS equations for analyzing arbitrary antenna/obstacle/antenna geometries. Accordingly, the SWS technique is considered to be a potentially valuable area for candidate further study in future investigations.

#### D. GTD Analysis

Relatively simple equations are presented in Reference 30 for estimating the coupling of power between cosited reflector antennas. The equations were derived with aid of the GTD analysis. They are applicable to situations whereby the "mainbeams" of the two antennas are not directed toward each other. That is, the equations are applicable to "sidelobe-to-sidelobe" coupling situations. They are not applicable to "mainbeam-to-mainbeam" or "mainbeam-to-sidelobe" coupling situations. Thus, the GTD equations complement the current PWS method presented previously which is particularly well suited for the mainbeam-to-mainbeam and mainbeam-to-sidelobe coupling situations. It should be noted that the equations lack the rigor associated with the PWS and SWS analyses and that it is difficult to judge the absolute accuracy of the equations. Nevertheless, the equations are potentially useful for "rough" engineering estimates of sidelobe-to-sidelobe antenna coupling.

The simplified GTD coupling analysis can be illustrated by considering the coplanar arrangement of two circular-aperture horn-fed paraboloidal reflector antennas shown in Figure 3-17. The various symbols shown on the figure are defined as

- $d_1$  = aperture diameter of Antenna 1,
- $d_2$  = aperture diameter of Antenna 2,
- $l_1$  = length of OP,
- $l_2$  = length of OQ<sub>1</sub>,
- $l_3$  = length of OQ<sub>2</sub>,
- $l_4$  = length of Q<sub>1</sub>P,
- $l_5$  = length of Q<sub>2</sub>P,
- $l_6$  = separation between antenna centers.

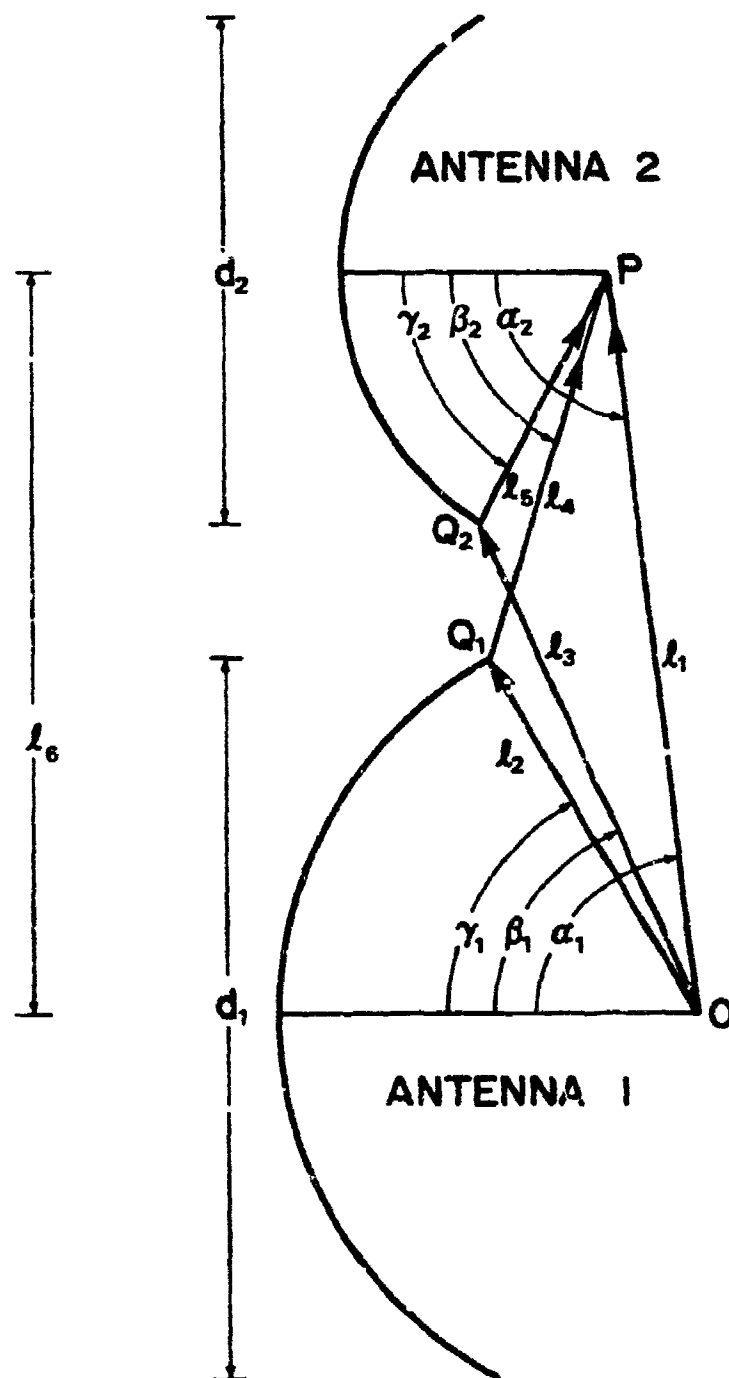


Figure 3-17. Sketch depicting the linear distances and the angles used in the GTD antenna coupling analysis.

The angles  $\alpha_1, \beta_1, \delta_1, \alpha_2, \beta_2, \delta_2$  open positive as shown.

Two different types of coupling are depicted in Figure 3-17. These are (1) direct coupling of the feed horns along  $\overline{OP}$ , (2) and single diffraction coupling along  $\overline{OQ_1-Q_1P}$  and also along  $\overline{OQ_2-Q_2P}$ . Thus, there are three contributions to the total coupling between the antennas.

The author of Reference 24 calculates the coupling coefficient for each type of coupling when only that particular coupling mechanism exists. The coupling coefficient is defined as the ratio of the received power to the transmitted power. The total coupling coefficient  $\eta$  when both types of coupling exist (implying three contributions as noted in the preceeding paragraph) is computed as

$$\eta = \eta_1 + \eta_2 + \eta_3 + 2\sqrt{\eta_1\eta_2} \cos(\xi_{12}) + 2\sqrt{\eta_2\eta_3} \cos(\xi_{23}) + 2\sqrt{\eta_1\eta_3} \cos(\xi_{13}) \quad (3-22)$$

where

- $\eta_1$  = power coupling coefficient for direct  $\overline{OP}$  coupling,
- $\eta_2$  = power coupling coefficient for single diffraction  $\overline{OQ_1-Q_1P}$  coupling,
- $\eta_3$  = power coupling coefficient for single diffraction  $\overline{OQ_2-Q_2P}$  coupling.

and where  $\xi_{12}$ ,  $\xi_{23}$ , and  $\xi_{13}$  are the relative phase angles between the electric fields arriving at P via paths indicated by the subscripts.

The power coupling coefficients  $\eta_1$ ,  $\eta_2$ , and  $\eta_3$  presented in Reference 24 may be written in our notation as

$$\eta_1 = \frac{\lambda^2 G_1 G_2}{(4\pi L_1)^2} \left[ \bar{H}_1(\alpha_1) \cdot \bar{H}_2(\alpha_2) \right]^2 \quad (3-23)$$

$$n_2 = \frac{\lambda^3 G_1 G_2}{16\pi^4 d_1^2 \ell_2 \ell_6} \left[ \bar{S}_1(\gamma_1, \theta_1, \theta_s) \cdot \bar{H}_2(\beta_2) \right]^2 \sin^2(\beta_2), \text{ and} \quad (3-24)$$

$$n_3 = \frac{\lambda^3 G_1 G_2}{16\pi^4 d_1^2 \ell_3 \ell_6} \left[ \bar{S}_2(\beta_1, \theta_1, \theta_s) \cdot \bar{H}_2(\gamma_2) \right]^2 \sin^2(\gamma_2). \quad (3-25)$$

where

$\lambda$  = the wavelength in free space,

$G_1$  = the peak gain of feed horn 1, and

$G_2$  = the peak gain of feed horn 2.

$\bar{H}_1$  and  $\bar{H}_2$  in Equation (3-23) are the vectorial horn patterns with azimuthal and elevation vectorial components  $\hat{\phi}$  and  $\hat{\theta}$ . The vector  $\bar{S}_1$  and the vectorial pattern  $\bar{H}_2$  appearing in Equation (3-24) are defined with respect to the edge diffraction point coordinate system erected at  $Q_1$  with  $\hat{\phi}_1$  tangent to the edge and  $\hat{\theta}_1$  perpendicular to the edge. Similarly,  $\bar{S}_2$  and  $\bar{H}_2$  appearing in Equation 3-25 are defined with respect to the edge diffraction point coordinate system erected at  $Q_2$  with  $\hat{\phi}_2$  tangent to the edge and  $\hat{\theta}_2$  perpendicular to the edge.

$\bar{S}_1$  and  $\bar{S}_2$  are then written as

$$\bar{S}_1(\gamma_1, \theta_s) = H_{\phi_{11}}(\delta_1) F_{\phi_1}(\theta_i, \theta_s) \hat{\phi}_1 + H_{\theta_{11}}(\delta_1) F_{\theta_1}(\theta_i, \theta_s) \hat{\theta}_1 \quad (3-26)$$

and

$$\bar{S}_2(\beta_1, \theta_s) = H_{\phi_{12}}(\delta_2) F_{\phi_2}(\theta_i, \theta_s) \hat{\phi}_2 + H_{\theta_{12}}(\delta_2) F_{\theta_2}(\theta_i, \theta_s) \hat{\theta}_2 \quad (3-27)$$

where the notation  $H_{\phi_{11}}$  indicates the component of  $H_1$  with respect to the coordinate system  $(\phi_1, \theta_1)$ , etc. The angles of incidence  $\theta_i$  and the angle of scatter  $\theta_s$  appearing in the edge diffraction function  $F$  are

associated with an edge point are, of course, specified with respect to the particular edge point coordinates shown in Figure 3-18.  $F_{\phi 1}(\theta_i, \theta_s)$  and  $F_{\theta 1}(\theta_i, \theta_s)$  are computed as

$$F_{\phi 1}(\theta_i, \theta_s) = \frac{\cos\left[\frac{\theta_i}{2}\right] \sin\left[\frac{\theta_s}{2}\right]}{\cos(\theta_s) - \cos(\theta_i)} \quad (3-26)$$

$$F_{\theta 1}(\theta_i, \theta_s) = \frac{\sin\left[\frac{\theta_i}{2}\right] \cos\left[\frac{\theta_s}{2}\right]}{\cos(\theta_s) - \cos(\theta_i)} \quad (3-27)$$

where it is assumed that the scattering angle of interest is away from the shadow boundary defined by  $\theta_s = \pm\theta_i$ . This restriction can be eliminated via the use of modified edge diffraction formulas as presented in References [25,26]. However, (3-26) and (3-27) are satisfactory for our purposes.

This simplified version of the very powerful GTD analysis technique can be used to make rapid computer estimates of out-of-band as well as in-band antenna coupling by specifying the feed horn patterns of the two antennas over the frequency intervals of interest. It is again noted that the equations are applicable only to sidelobe-to-sidelobe coupling situations. Stochastic equations based on the foregoing GTD equations could be derived expressed in terms of the mode excitation coefficients. However, the PWS and/or the SWS techniques are envisioned as the more promising methods for stochastic coupling analysis for arbitrary situations and, consequently, the GTD analysis was not pursued further.

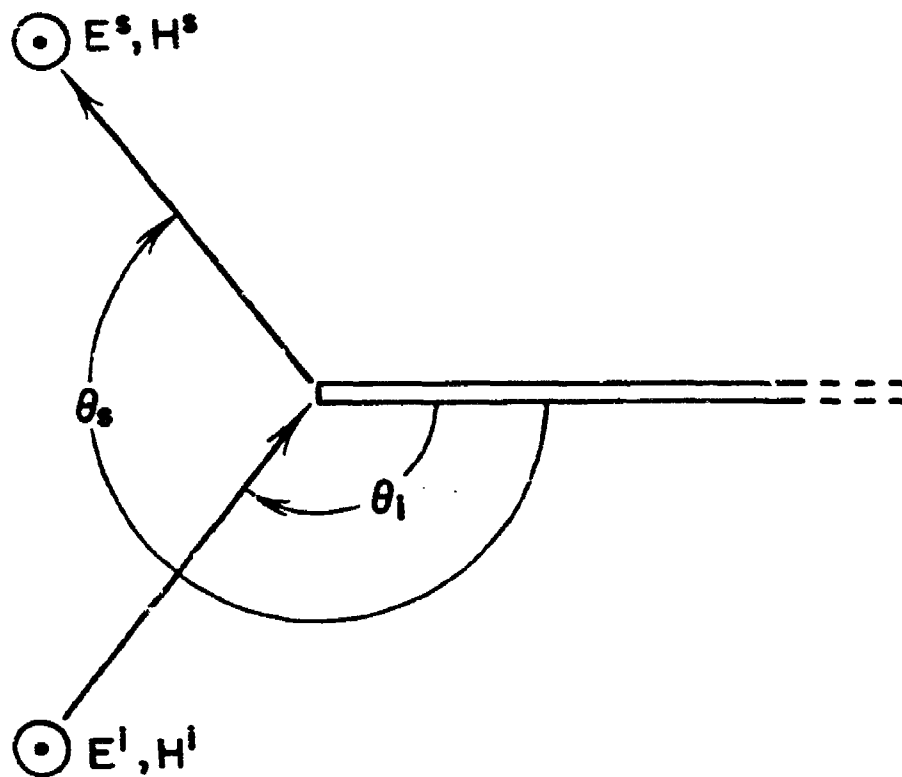


Figure 3-12. Diffraction by a half-plane showing the incident ( $\theta_i$ ) and scattering ( $\theta_s$ ) angles used in the diffraction coefficient.

## SECTION IV

### SYSTEM DEVICE EFFECTS

#### A. Introduction

The two main objectives for this task were (1) to develop a method for analyzing the antenna pattern effects of higher order modes generated and/or propagated by common feed system devices and (2) to assess the feasibility of deducing the mode excitations for a radiating feed system from analysis of measured out-of-band pattern data. The first objective has been achieved via the theory and equations developed during the course of the research work on Task I and Task II presented in Sections II and III, respectively. The results of the research work pertaining to the second objective are presented and discussed in subsection B of this section.

The timely completion of the required research work for this task permitted a brief digression into another important aspect of the out-of-band response of system devices. In particular, equations were sought to describe the influence of particular waveguide devices on the excitation and subsequent propagation of out-of-band waveguide modes. Three waveguide devices were considered in this exploratory study, namely (1) coax-to-waveguide adapters, (2) radial bends, and (3) ferrite phase shifters. Program constraints precluded a detailed quantitative analysis of all three kinds of devices. Accordingly, the research efforts were concentrated mainly on the theoretical and numerical analysis of a coax-to-waveguide adapter. The results of the exploratory study are summarized in subsection C.

#### B. Computation of Mode Coefficients From Measured Out-of-Band Pattern Data

The mode coefficients for the propagating modes of a radiating feed system can be determined from a knowledge of the aperture tangential electric fields. The aperture fields can be determined to good approximation from the complex far-field electric field patterns of the feed system.

The hypothetical experimental arrangement consisting of an arbitrary feed system terminating in a large metallic "ground plane" is

shown in Figure 4-1. The feed system is assumed to consist of (1) an input section which, for example, might be a coax-to-waveguide adapter or a power coupling iris, (2) passive and/or active devices, such as a radial bend and a phase shifter, and (3) the radiative element, which is an unflared straight waveguide section. Note that the guide axis is along the  $\hat{x}$  coordinate and that the  $\hat{y}$  and  $\hat{z}$  coordinates are the transverse coordinates. This orientation of coordinate axes is a convenient one for the problem at hand.

A measurement is performed to determine the far-field complex vectorial electric field in the forward hemisphere. The measurement is probably most efficiently accomplished via the planar near-field measurement technique. The far-field electric field is then accurately computed via established FFT processing of the near-field data [25].

The transverse electric fields  $\bar{E}(y,z)$  in the aperture of the radiating system may be computed accurately as

$$\bar{E}(y,z) = \sum_p \sum_q \bar{E}_{pq} \exp[-j(k_{ypq} y + k_{zq} z)] \quad (4-1)$$

where the coefficient  $\bar{E}_{pq}$  is the complex far-field electric field in the direction defined by ( $k_y = k_{ypq}$ ,  $k_z = k_{zq}$ ) where

$$k_{ypq} = k_0 \sin(\theta_q) \sin(\phi_p), \quad (4-2)$$

$$k_{zq} = k_0 \cos(\theta_q), \text{ and} \quad (4-3)$$

$$k_0 = 2\pi/\lambda \quad (4-4)$$

where  $\lambda$  is the free space wavelength.

The mode coefficients are determined by solving the simultaneous equations obtained from the continuity of the tangential components of the  $\bar{E}$  and  $\bar{H}$  fields at the aperture. The appropriate equations at the aperture ( $x=0$ ) may be written as

$$\sum_K a_K \bar{Y}_K^+ (y,z) + \sum_K b_K \bar{Y}_K^- (y,z) = \sum_p \sum_q \bar{E}_{pq} \varphi_{pq} (y,z), \text{ and} \quad (4-5)$$



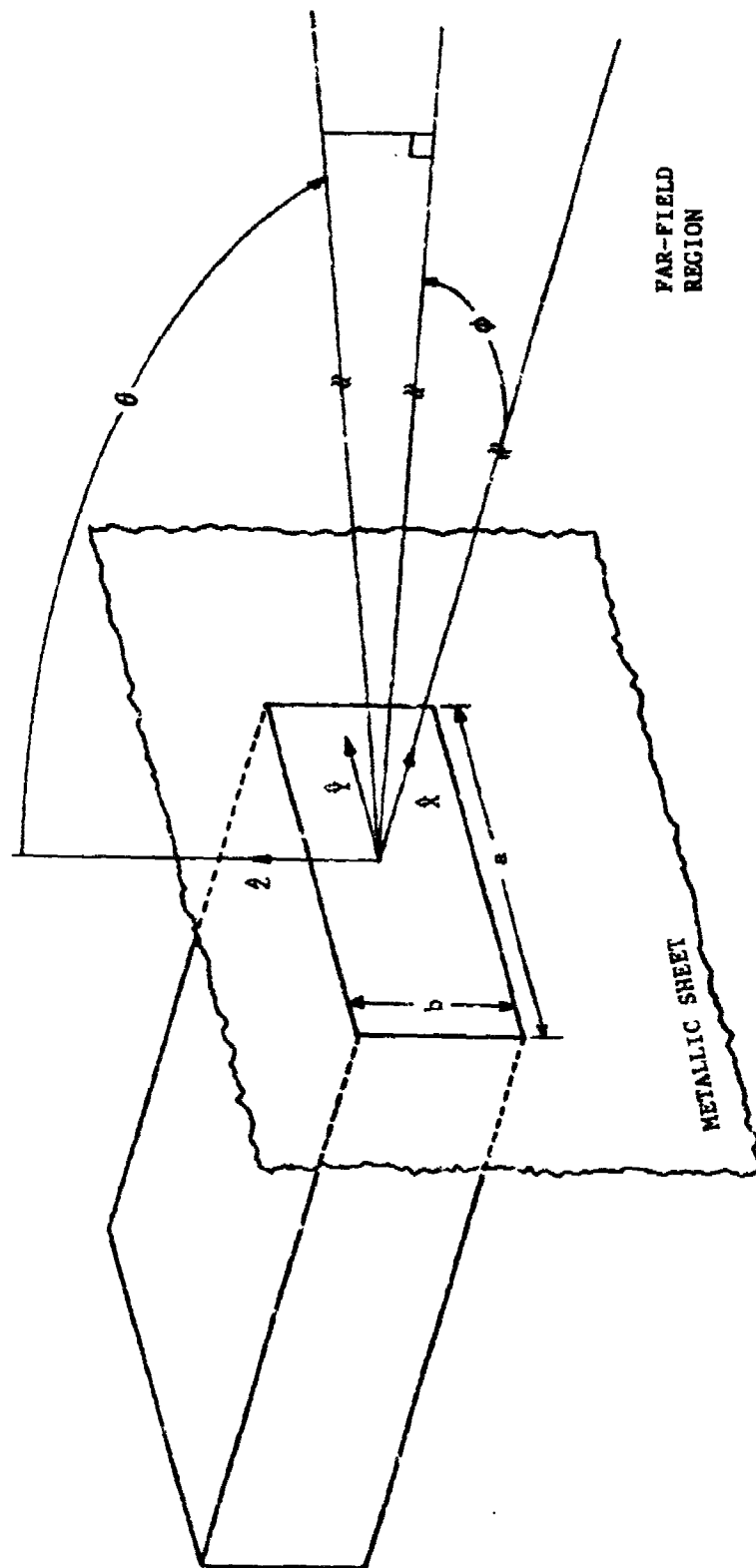


Figure 4-1. Sketch depicting a rectangular waveguide transmission line terminating in a large "ground plane" and showing selected geometrical variables.

$$\sum_{\kappa} a_{\kappa} \bar{\Gamma}_{\kappa} \cdot \bar{\Psi}_{\kappa}^{+}(\tau, z) - \sum_{\kappa} b_{\kappa} \bar{\Gamma}_{\kappa} \cdot \bar{\Psi}_{\kappa}^{-}(y, z) = \sum_p \sum_q \bar{\Gamma}_{pq} \cdot \bar{E}_{pq} \varphi_{pq}(y, z). \quad (4-6)$$

where,

$a_{\kappa}$  = the complex excitation coefficient for the allowed  $\kappa$ th waveguide mode,

$b_{\kappa}$  = the complex reflection coefficient for the  $\kappa$ th waveguide mode,

$\bar{\Psi}_{\kappa}^{(\pm)}(y, z)$  = the transverse-to- $\hat{x}$  vectorial waveguide electric field function for propagation in the  $(\pm)$   $x$ -direction,

$$\varphi_{pq}(y, z) = \exp[-j(k_{ypq} y + k_{zq} z)], \quad (4-7)$$

$\bar{\Gamma}_{pq}$  = the effective wave admittance dyadic for the radiated fields,  $\Gamma_{pq} = k_0 \sin(\theta_q) \cos \phi_p / \omega \mu$ , and

$\bar{\Gamma}_{\kappa}$  = the wave admittance dyadic for the waveguide field functions.

The waveguide admittance dyadic  $\bar{\Gamma}_{\kappa}$  is just

$$\bar{\Gamma}_{\kappa} \equiv \begin{bmatrix} \Gamma_{\kappa} \hat{y} \hat{y} & 0 \\ 0 & -\Gamma_{\kappa} \hat{z} \hat{z} \end{bmatrix} \quad (4-8)$$

where  $[\Gamma_{\kappa} = \beta_{\kappa} / \omega \mu]$  for TE-to- $\hat{x}$  modes and  $[\Gamma_{\kappa} = \omega \epsilon / \beta_{\kappa}]$  for TM-to- $\hat{x}$  modes. The effective wave admittance dyadic  $\bar{\Gamma}_{pq}$  for the radiated fields is

$$\bar{\Gamma}_{pq} = \begin{bmatrix} \Gamma_{pq} \hat{y} \hat{y} & 0 \\ 0 & -\Gamma_{pq} \hat{z} \hat{z} \end{bmatrix} \quad (4-9)$$

where  $\Gamma_{pq} = [k_0 \sin(\theta_q) \cos(\phi_p)] / \omega \mu$ .

The waveguide electric field functions are assumed to be arranged in ascending order of cut-off frequency. The electric fields for the TE and TM modes that have the same cutoff frequency require special handling in order to preserve a desirable orthogonality property of the mode fields. In particular, if  $\bar{U}_\kappa^+(y, z)$  is a TE mode field with cut-off wavelength  $\lambda_c$  and  $\bar{V}_\kappa^+(y, z)$  is the TM mode field with the same cut-off wavelength, the waveguide field functions  $\bar{V}_\kappa^+(y, z)$  and  $\bar{V}_{\kappa+1}^+(y, z)$  are taken to be

$$\bar{V}_\kappa^+(y, z) = \bar{U}_\kappa^+(y, z), \text{ and} \quad (4-10)$$

$$\bar{V}_{\kappa+1}^+(y, z) = \alpha_\kappa \bar{U}_\kappa^+(y, z) + \bar{V}_\kappa^+(y, z), \quad (4-11)$$

where

$$\alpha_\kappa = - \frac{\iint [\bar{U}_\kappa^+(y, z)]^* \cdot \bar{V}_\kappa^+(y, z) dydz}{\iint [\bar{U}_\kappa^+(y, z)]^* \cdot \bar{U}_\kappa^+(y, z) dydz} \quad (4-12)$$

$\alpha_\kappa$  is set equal to zero for any pair of modes that have different cut-off wavelengths. The integrals are evaluated over the guide cross section.

The z-polarized and y-polarized electric fields for the TE waveguide modes traveling in the positive x-direction are

$$[U_\kappa^+(y, z)]_z = + \frac{j\omega\mu(\frac{n\pi}{a})}{[(\frac{n\pi}{b})^2 + (\frac{n\pi}{a})^2]} \sin[\frac{n\pi}{a}(y + \frac{a}{2})] \cos[\frac{n\pi}{b}(z + \frac{b}{2})] \exp[-j\beta_\kappa x] \text{ and} \quad (4-13)$$

$$[U_\kappa^+(y, z)]_y = + \frac{j\omega\mu(\frac{n\pi}{b})}{[(\frac{n\pi}{b})^2 + (\frac{n\pi}{a})^2]} \cos[\frac{n\pi}{a}(y + \frac{a}{2})].$$

$$\sin \left[ \frac{m\pi}{b} \left( z + \frac{b}{2} \right) \right] \exp \left[ \pm j\beta_{\kappa} x \right], \quad (4-14)$$

where

$$\beta_{\kappa} = \sqrt{k_0^2 - \left( \frac{n\pi}{a} \right)^2 - \left( \frac{m\pi}{b} \right)^2}, \text{ and} \quad (4-15)$$

where the  $n$  and  $m$  indices are chosen based on the mode ordering scheme previously discussed. Similarly, the  $z$ -polarized and  $y$ -polarized electric fields for the TM modes are

$$\begin{aligned} [V_{\kappa}^{+}(y, z)]_z &= \frac{\mp j\beta_{\kappa} \left( \frac{m\pi}{b} \right)}{\left[ \left( \frac{m\pi}{b} \right)^2 + \left( \frac{n\pi}{a} \right)^2 \right]} \sin \left[ \frac{n\pi}{a} \left( y + \frac{a}{2} \right) \right] \\ &\cos \left[ \frac{m\pi}{b} \left( z + \frac{b}{2} \right) \right] \exp \left[ \mp j\beta_{\kappa} x \right] \text{ and} \end{aligned} \quad (4-16)$$

$$\begin{aligned} [V_{\kappa}^{+}(y, z)]_z &= \frac{\mp j\beta_{\kappa} \left( \frac{m\pi}{b} \right)}{\left[ \left( \frac{m\pi}{b} \right)^2 + \left( \frac{n\pi}{a} \right)^2 \right]} \cos \left[ \frac{n\pi}{a} \left( y + \frac{a}{2} \right) \right] \\ &\sin \left[ \frac{m\pi}{b} \left( z + \frac{b}{2} \right) \right] \exp \left[ \pm j\beta_{\kappa} x \right] \end{aligned} \quad (4-17)$$

It should be noted here that mode sets other than the mode sets TE and TM to the longitudinal axis can be employed. However, this is frequently a convenient set of modes and serves to illustrate the basic theory and equations.

The solution for the mode coefficients  $a_\kappa$  is readily achieved by (1) scalarly multiplying Equation (4-6) by  $(\bar{v}_\kappa^+)^*$  and integrating both sides of the equation over the guide cross section; (2) scalarly multiplying Equation (4-5) by  $(\bar{v}_\kappa^+)^* \cdot \bar{\Gamma}_\kappa$  and integrating both sides of the equation over the guide cross section, making use of the orthogonality of the mode fields to retain only the  $\kappa = \kappa'$  terms, and solving the simultaneous equations in the unknown  $a_\kappa$  and  $b_\kappa$  for  $a_\kappa$ . The solution for  $a_\kappa$  so obtained is

$$a_\kappa = \frac{\sum_p \sum_q \bar{T}_{pq\kappa} \cdot [\bar{\Gamma}_\kappa + \bar{\Gamma}_{pq}] \cdot \bar{E}_{pq}}{2 \int_{-\frac{a}{2}}^{\frac{a}{2}} \int_{-\frac{b}{2}}^{\frac{b}{2}} [\bar{v}_\kappa^+(y,z)]^* \cdot \bar{\Gamma}_\kappa \cdot \bar{v}_\kappa^+(y,z) dz dy} \quad (4-18)$$

where

$$\bar{T}_{pq\kappa} = \int_{-\frac{a}{2}}^{\frac{a}{2}} \int_{-\frac{b}{2}}^{\frac{b}{2}} \varphi_{pq}(y,z) [\bar{v}_\kappa^+(y,z)]^* dz dy \quad (4-19)$$

is the complex conjugate of the vectorial far-field electric field pattern radiated by the  $\kappa^{\text{th}}$  waveguide mode. All of the quantities on the right-hand side of Equations (4-18) and (4-19) are known from experiment or theory and, hence, the coefficients  $a_\kappa$  may be computed.

### C. Summary of Out-of-Band Waveguide Device Characteristics

The emphasis in this brief study was on obtaining a qualitative understanding of the basic out-of-band mode excitations and propagation characteristics of (1) a coax-to-waveguide adapter, (2) radial bends, and (3) ferrite phase shifter. A detailed quantitative study of each device was outside the scope of these exploratory investigations due to the complexity of the solutions obtained for multimoding waveguides. Accordingly, attention was focused primarily on the coax-to-waveguide adapter. The key analytical results for the radial bends and the ferrite phase shifter are first briefly summarized in the following

paragraphs. The salient analytical numerical results for the coax-to-waveguide adapter are then presented and discussed.

### 1. Waveguide Radial Bends

The propagation of electromagnetic energy through radial "E-plane" and "H-plane" waveguide bends has been studied by a large number of authors during the last 45 years. A partial list of references is included in Section VII as References 26 through 34. Out-of-band as well as in-band propagation has been addressed. Rigorous solutions for the electric fields in bends are presented in References 26, 31, 32, and 33 in terms of infinite series of Bessel functions. The matrix solution due to Rice [30] is also capable of providing rigorous results. Rigorous solutions for the generation of higher order modes at the junction of straight and curved portions of a waveguide run have also been derived [32]. The rigorous solutions are generally valid for "sharp" bends as well as for "gradual" bends. A sharp bend is defined herein as one for which  $\Delta R/R \leq 1$  and a gradual bend is one for which  $\Delta R/R \ll 1$ , where  $R$  is the bend radius and  $\Delta R$  is the thickness of the bend along  $\theta$ , as per Figure 4-2.

The approximate analysis of a gradual H-plane bend by Jouget [27,28] furnishes valuable physical insight as well as useful approximate equations for the intermodal coupling coefficients at the junction of the straight and curved guides. The corresponding analysis for the round waveguides are also presented by Jouget in a separate paper [29]. Expressions for the mode cutoff frequencies and the mode phase velocities in the curved portions of the waveguide are also derived. The corresponding analysis for an E-plane bend is presented to second order by Lewin [34]. Good engineering approximations for the mode conversion coefficients at the entrance and/or exit junctions are possible even for moderately sharp bends where  $\Delta R/R \approx 0.1$ .

### 2. Ferrite Phase Shifter

The main difficulty in the analysis of a waveguide containing a ferrite phase shifter is in obtaining a valid representation for the electric field or the magnetic field in the portion of the guide containing the ferrite slab. Once these characteristic fields are obtained, the usual procedure of requiring continuity of the fields at

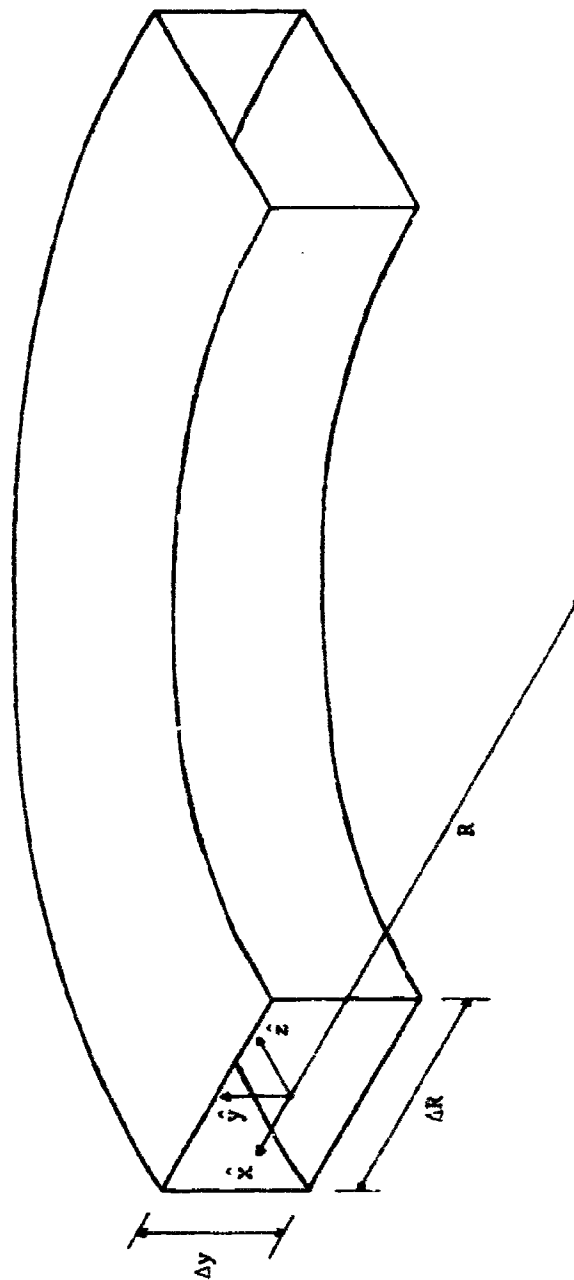


Figure 4-2. Sketch depicting a radial bend and pertinent geometrical variables.

the entrance and exit faces of the slab can be invoked. This leads, of course, to a set of simultaneous equations that are readily solved to provide reflection and transmission coefficients as functions of the phase shifter control setting for a specified incident mode. For example, the fields for a rectangular guide containing a ferrite slab extending fully across one dimension of the guide, as per Figure 4-3, can be solved exactly. However, the exact solution for slab geometry shown in Figure 4-4 is too complex to be useful and, hence, approximate techniques are sought.

The ferrite phase shifter is generally a lossy, anisotropic medium and, consequently, the application of perturbational or variational techniques is more complex than for typical waveguide problems [11,35]. Nonetheless, the application of variational techniques to the ferrite phase shifter problem is potentially very useful. The equations presented by Moshen [36] appear to be particularly well-suited for this problem. Moshen derives a stationary quantity  $F$  that is valid for a lossy, anisotropic, inhomogeneous medium which, for a source free region, is

$$\begin{aligned}
 F = & [\bar{\nabla} \times \bar{E}, \bar{H}]_S + [\bar{\nabla} \times \bar{H}, \bar{E}]_S \\
 & + j\omega ([\bar{B}, \bar{H}]_S - [\bar{D}, \bar{E}]_S) \\
 & + [\bar{E}, \bar{H}]_C
 \end{aligned} \tag{4-20}$$

where quantities of the form  $[\bar{A}, \bar{B}]_S$  and  $[\bar{A}, \bar{B}]_C$  denote the "inner products"

$$[\bar{A}, \bar{B}]_S = \iint_S \bar{A} \cdot \bar{B}^\dagger ds \text{ and} \tag{4-21}$$

$$[\bar{A}, \bar{B}]_C = \int_C \bar{A} \cdot (\hat{n} \times \bar{B}^\dagger) ds, \tag{4-22}$$



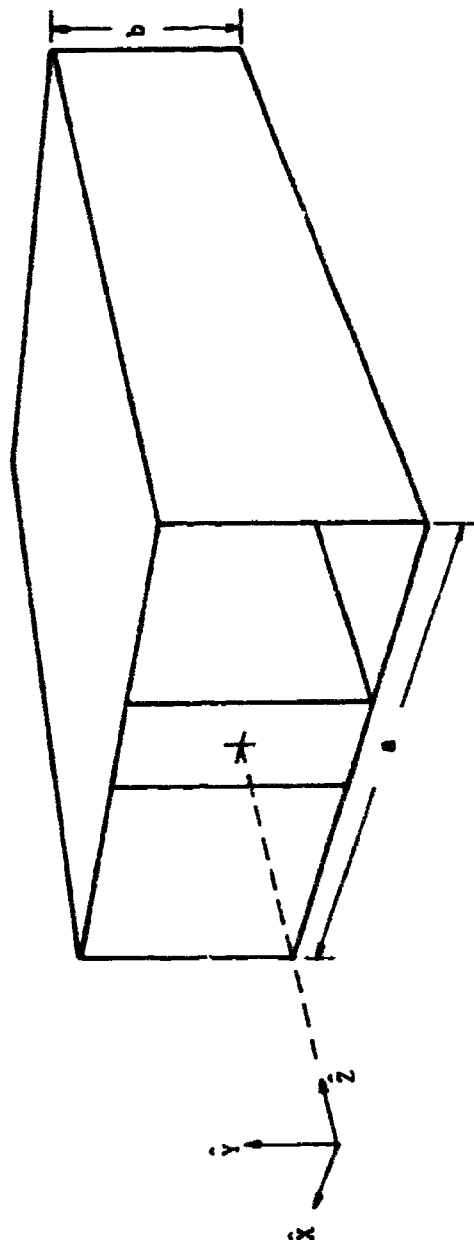


Figure 4-3. Sketch depicting a section of rectangular waveguide containing a ferrite waveguide slab whose height equals the waveguide height.

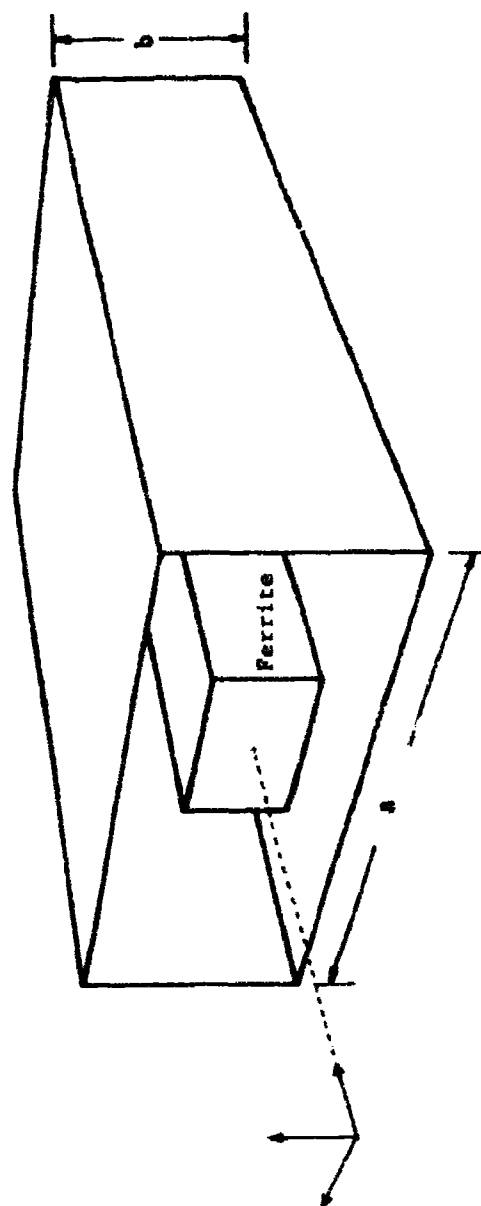


Figure 4-4. Sketch depicting a section of rectangular waveguide containing a ferrite slab whose two transverse dimensions are less than the corresponding dimensions of the waveguide.

respectively. The symbols  $\vec{E}$ ,  $\vec{H}$ , and  $\vec{B}$  denote the electric field vector, the magnetic field intensity vector, and the magnetic field vector, consecutively. The inner product  $[\vec{A}, \vec{B}]_s$  is evaluated over the guide cross section. The inner product  $[\vec{A}, \vec{B}]_c$  is evaluated around the periphery of the guide cross section. The superscript symbol  $+$  denotes the adjoint of the field quantity to which it is appended.

A variational expression for the propagation constant in the ferrite phase shifter can be obtained from Equation (4-20). The trial field  $\vec{E}(x, y, z)$  may be conveniently chosen as the superposition of mode fields  $\vec{\Psi}_k(x, y, z)$  for the empty waveguide, to wit:

$$\vec{E}(x, y, z) = \sum_k C_k \vec{\Psi}_k(x, y, z), \quad (4-23)$$

The trial  $\vec{H}$  and  $\vec{B}$  vectors are obtained from Equation (4-23) via the Maxwell curl relation and the constitutive relation  $\vec{B} = \vec{\mu} \cdot \vec{H}$ , where  $\vec{\mu}$  is the permeability tensor [34] for the ferrite slab. The expansion coefficients  $C_k$  which extremize the propagation coefficient are found by numerically solving the set of simultaneous equations obtained from the variational equations. Thus, the electric field  $\vec{E}$  given by Equation (4-23) is determined and can thence be employed in the analysis and computation of reflection and transmission coefficients for the ferrite section.

### 3. Study of the Coax-to-Waveguide Adapter Device

The goal of this study is to obtain a qualitative understanding of the higher order mode excitation and propagation characteristics of the coax-to-waveguide adapter. The results of this study provide useful insight into the basic out-of-band characteristics of a coax-to-waveguide adapter.

The solution for the mode excitation coefficients for the coax-to-waveguide adapter shown in Figure 4-5 can be obtained with the aid of equations given in Collin [34]. Note that  $y$  and  $x$  are transverse coordinates and the longitudinal axis of the guide is along  $z$ . In particular, the dyadic Green function  $\vec{G}(x', y', z' | x, y, z)$  derived by

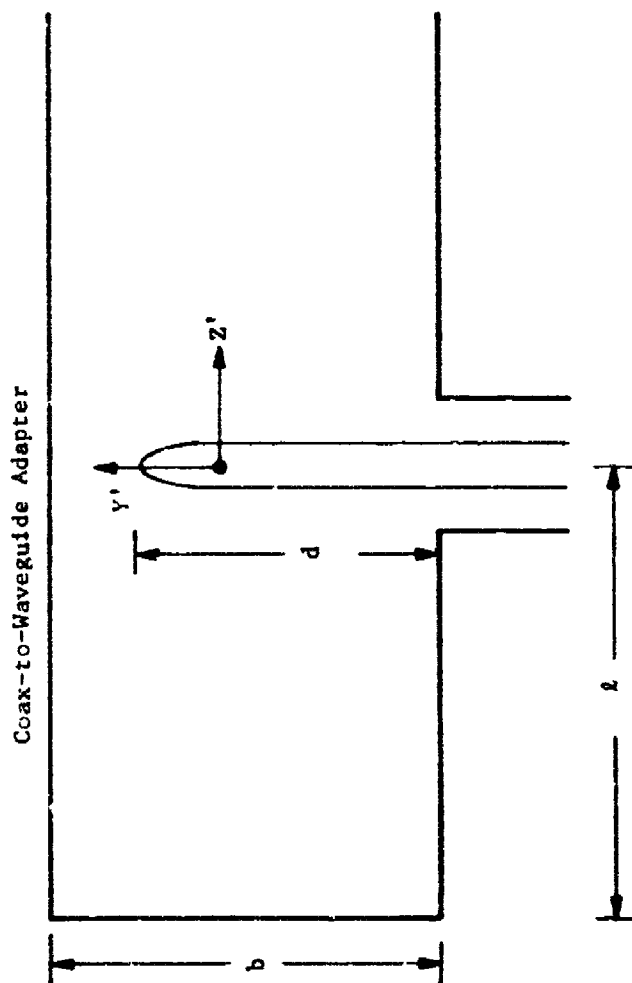


Figure 4-5. Sketch depicting a side view of a coax-to-waveguide adapter and showing selected geometrical variables.

Collin for an infinitesimal electric dipole, located at  $(x', y', z')$  in a rectangular waveguide is applicable to both in-band and out-of-band waveguides. The magnetic vector potential  $A = \bar{A}_y \hat{y}$  produced by an assumed current density  $\bar{J} = \hat{y} J_0 \sin [k_0(d-y')]$  on the probe and is derived by integrating the product  $\bar{G} \cdot \bar{J}$  along the probe surface  $S_0$ , to wit:

$$\bar{A}(x, y, z) = -\mu_0 \int_{S_0} \int \bar{G}(x', y', z' / x, y, z) \cdot \bar{J}(y') da' \quad (4-24)$$

Expressions for  $\bar{E}(x, y, z)$  and  $\bar{H}(x, y, z)$  are then readily obtained via the well known operations

$$\bar{E}(x, y, z) = -j\omega \bar{A}(x, y, z) + \frac{\bar{\nabla}(\bar{\nabla} \cdot \bar{A})}{j\omega \epsilon_0 \mu_0} \quad (4-25)$$

and

$$\bar{H}(x, y, z) = \frac{1}{\mu_0} (\bar{\nabla} \times \bar{A}) \quad (4-26)$$

The electric field  $\bar{E}(x, y, z)$  obtained from Equation (4-25) can be written as an expansion.

$$\bar{E}(x, y, z) = \sum_n \sum_m b_{nm} \bar{\chi}_{nm}(x, y, z) \quad (4-27)$$

where  $m = 0, 1, 2, 3, 4, \dots$  and  $n = \text{odd positive integer } n = 1, 3, 5, 7, \dots$ , the selection of the values of index  $n$  being imposed by the requirement that the vector potential  $\bar{A}(x, y, z) \neq 0$ . The expansion functions  $\bar{\chi}_{nm}$  are the  $TM_{nm}^y$  waveguide mode functions which have no component of  $\bar{H}$  along the transverse  $y$  direction. (Thus, one can anticipate that longitudinal power flow is associated only with the  $y$ -polarized electric fields of the  $TM_{nm}^y$  modes since  $E_x H_y = 0$ ). The coefficients  $b_{nm}$  are

$$b_{nm} = \left[ \frac{\exp[-j\beta_{nm} z] - \exp[-j\beta_{nm} (z+l)]}{j\beta_{nm}} \right] \cdot \left[ 2\pi \sin\left[\frac{n\pi}{2}\right] J_0 \frac{k_0 [\cos(k_0 d) - \cos(m\pi \frac{d}{b})]}{(\frac{m\pi}{b})^2 - k_0^2} \right] \cdot \epsilon_{om} \quad (4-28)$$

where  $\epsilon_{om} = 1$  for  $m = 0$   
and  $\epsilon_{om} = 2$  otherwise.

The vector function  $\tilde{\chi}_{nm}(x, y, z)$  is expressed in terms of its components as

$$\begin{aligned} \chi_{nmx} \hat{x} = & \left\{ \left[ \frac{-2}{j\omega\epsilon_0 ab} \right] \left[ \frac{m\pi}{ab} \right]^2 \cos \left[ \frac{n\pi}{a} \left( x + \frac{a}{2} \right) \right] \cdot \right. \\ & \left. \cdot \sin \left[ \frac{m\pi}{b} \left( y + \frac{b}{2} \right) \right] \right\} \hat{x} \end{aligned} \quad (4-29)$$

$$\begin{aligned} \chi_{nmy} \hat{y} = & \left\{ \left[ -\frac{2\mu_0}{ab} \right] \left[ j\omega + \frac{1}{j\mu_0\epsilon_0\omega} \left( \frac{m\pi}{b} \right)^2 \right] \cdot \right. \\ & \left. \cdot \sin \left[ \frac{n\pi}{a} \left( x + \frac{a}{2} \right) \right] \cos \left[ \frac{m\pi}{b} \left( y + \frac{b}{2} \right) \right] \right\} \hat{y}, \end{aligned} \quad (4-30)$$

$$\begin{aligned} \chi_{nmz} \hat{z} = & \left\{ \left[ \left( \frac{m\pi}{b} \right) j\beta_{nm} \right] \sin \left[ \frac{n\pi}{a} \left( x + \frac{a}{2} \right) \right] \cdot \right. \\ & \left. \cdot \cos \left[ \frac{m\pi}{b} \left( y + \frac{b}{2} \right) \right] \right\} \hat{z}. \end{aligned} \quad (4-31)$$

The electric field  $E(x,y,z)$  can be expressed with the aid of Equation (4-25) as

$$\bar{E}(x,y,z) = \frac{1}{j\omega\epsilon_0\mu_0} \left\{ \frac{\partial^2 A}{\partial x \partial y} \hat{x} + \frac{\partial^2 A}{\partial y^2} \hat{y} + \frac{\partial^2 A}{\partial z \partial y} \hat{z} \right\} \quad (4-32)$$

and  $\bar{H}(x,y,z)$  via Equation (4-26) as

$$\bar{H}(x,y,z) = \frac{1}{\mu_0} \left( \frac{\partial A}{\partial x} \hat{z} - \frac{\partial A}{\partial z} \hat{x} \right) \quad (4-33)$$

The average power density  $S_z$  transported along the  $\hat{z}$  direction is

$$S_z = \bar{S} \cdot \hat{z} = \frac{1}{2} \operatorname{Re} \left[ \frac{1}{\mu_0} E_y \left( \frac{\partial A}{\partial z} \right)^* \right] \quad (4-34)$$

where  $\bar{S}$  is the pointing vector defined as

$$\bar{S} = \frac{1}{2} \operatorname{Re}(\bar{E} \times \bar{H}^*) \quad (4-35)$$

$H^*$  the complex conjugate magnetic field vector and  $\hat{z}$  the unit vector in the direction of propagation. Utilizing Equations (4-24 to 4-36), a closed form expression for the power  $P_{nm}$  propagated in a coax-to-waveguide adapter can be derived by integrating Equation (4-35) over the guide cross section to obtain

$$P_{nm} = \frac{1}{2} \operatorname{Re} \frac{U_o}{ab} J_o^2 \pi^2 \epsilon_n \epsilon_m \epsilon_{om}^2 \sin^2 \left[ \frac{m\pi}{2} \right] k_o^2 \frac{[\cos k_o d - \cos m\pi (\frac{d}{b})]^2}{[(\frac{m\pi}{b})^2 - k_o^2]^2}$$

$$\cdot \frac{[\exp(-j\beta_{nm} z) - \exp\{-j\beta_{nm}(z+l)\}] \cdot [\exp(-j\beta_{nm} z) - \exp(-j\beta_{nm}(z+l))]}{j\beta_{nm}}^*$$

$$\cdot (j\omega + \frac{1}{j\omega \epsilon_o} (\frac{m\pi}{b})^2) \quad (4-36)$$

where Re means "real part of" and where all other symbols have been defined previously. The total power propagating along the waveguide is partitioned among the different possible  $TM_{nm}^y$  modes that have  $n > 0$  for a particular operating frequency. Calculations of the power distribution among the different higher order modes were made for standard S-band coax-to-waveguide adapters for frequencies ranging from 3.0 to 10.0 GHz. The values of the various physical parameters of the adapter and waveguide for the numerical study are as follows:

$$\begin{aligned} a &= 7.112 \text{ cm} \\ b &= 3.302 \text{ cm} \\ d &= 1.9 \text{ cm} \\ z &= 3.5 \text{ cm} \\ l &= 2.4 \text{ cm} \end{aligned}$$

The calculations were performed on the assumption of the total power radiated to be equal to 1.0 watt corresponding to a dipole resistance  $R = 500$  ohms and a current  $J_o = 45$  milliams.

It should be noted again that the power flow down the guide is associated entirely with the  $\hat{y}$ -polarized component of the electric field of the excited modes. The  $\hat{x}$ -component of the electric field does not contribute to the longitudinal power flow since the  $\hat{y}$  componet of the magnetic field is zero for the  $TM_{nm}^y$  modes.



Results of the computer calculations are tabulated for selected frequencies in Table 4-1. In particular, the modal power flow for each excited  $TM_{nm}^y$  modes is tabulated as the percentage of the total power flowing in all of the excited modes for the in-band frequency of 3.0 GHz and for the out-of-band frequencies of 6.0 GHz, 7.5 GHz, 9.0 GHz, 9.5 GHz, and 10.0 GHz. Inspection of the tabulated data shows how the total power flow is partitioned among the excited modes for each frequency. The dispersive character of the waveguide over the out-of-band frequency range from 6.0 GHz to 10.0 GHz is clearly evident in the data. The frequency sensitivity of the modal power flow distributions for the frequencies of 6.0 GHz, 7.5 GHz, 9.0 GHz, and 9.5 GHz is partially due to the fact that the total power flow is partitioned among 2 modes, 3 modes, 4 modes and 5 modes, consecutively. However, considerable frequency sensitivity is also evidenced for the out-of-band frequencies of 9.5 GHz and 10.0 GHz, both of which have the total power flow distributed among the same 5  $TM_{nm}^y$  modes.

It should be noted that the analysis of a coax-to-waveguide adapter having a non-filamentary current probe can be obtained via the equations presented in Reference 35 and herein. The Green function for empty rectangular waveguide presented in Chapter 7 of Reference 35 must be numerically integrated over the surface of the current probe that is being modeled. It would be particularly beneficial to analyze the out-of-band behavior of a coax-to-waveguide adapter having the shape of an elongated "teardrop" found in many commercial adapters. Adapters which have a concentric dielectric sleeve enclosing the current probe require the use of a more complicated Green function. It would also be of considerable practical value to numerically analyze the out-of-band characteristics of the dielectrically-sleeved adapters.

TABLE 4-1

MODAL POWER FLOW FOR THE  $TM_{nm}^y$  MODES FOR THE  
INDICATED FREQUENCIES FOR WR-284 WAVEGUIDE  
EXCITED BY AN IDEALIZED COAX-TO-WAVEGUIDE ADAPTER  
HAVING A FILAMENTARY CURRENT PROBE\*

Frequency	$TM_{nm}^y$ Modes	Modal Power Flow
(GHz)	(n,m indices)	(% of Total)
3.0	10	100.0
6.0	10	6.96
	11	93.04
7.5	10	11.99
	11	7.00
	30	81.01
9.0	10	47.05
	11	13.62
	30	0.45
	31	38.88
9.5	10	47.83
	11	17.86
	30	10.64
	31	6.40
	12	17.27
10.0	10	32.86
	11	11.51
	30	20.33
	31	0.00
	12	35.30

\* $TM_{nm}^y$  waveguide modes are defined with respect to the coordinate system depicted in Figure 4-5.

## SECTION V

### SITE EFFECTS

#### A. Introduction

It is well known that the performance of an antenna can be significantly degraded due to scattering of electromagnetic energy from metallic or dielectric structures located within the radiating near-field of the antenna. Several techniques are available for analyzing the effects of near-field obstacles for a specified operating frequency. Prominent among these techniques are aperture integration, the Geometrical Theory of Diffraction (GTD), and the Plane Wave Spectrum Scattering (PWSS) analysis. Although any of these techniques could be used for out-of-band frequency analysis, they have generally been applied to the analysis of in-band effects at a few selected frequencies of interest.

The analysis of the distortion of the envelope of a narrow time pulse requires a knowledge of the frequency domain antenna/obstacle response over a frequency interval exceeding the bandwidth of the pulse. Alternatively, a direct time domain analysis can be formulated and applied to near-field scattering problems, as per Reference[37]. However, a frequency domain analysis appears to be more flexible and appropriate for the wide variety of antenna/scattering situations that are encountered at Army directive antenna installations. Moreover, experience has shown that the PWSS method of antenna/obstacle analysis is particularly well suited for analyzing near-field obstacle effects. Accordingly, the frequency domain approach employing the PWSS scattering technique has been used to study the effects of near-field obstacles on the wideband CW and pulsed response of directive antennas for both in-band and out-of-band frequencies. The basic theory and equations are presented and discussed in subsection B, and the results of a numerical study of wideband site effects are summarized in subsection C.

#### B. PWSS Formulation

The monochromatic PWSS analysis is readily adapted to analyze near-field obstacle effects for wideband CW or pulsed systems. The

theory and equations for the deterministic monochromatic PWSS are outlined first.

### 1. Plane Wave Spectrum Analysis Concept

The basic theory of the Plane Wave Spectrum Scattering Matrix analysis is presented in References 22 and 38. A brief, somewhat heuristic synopsis is presented here. Figure 5-1 illustrates the basic concept and the antenna/obstacle geometry. Conceptually, the antenna Plane Wave Spectrum (PWS) referred to the antenna aperture propagates in the near-field and is incident upon an obstacle. Each component plane wave in the antenna spectrum excites a complete spectrum of obstacle scattered plane waves. The total scattered spectrum is thus the superposition of the scattered plane wave spectra due to the incident antenna spectrum.

If the antenna aperture is located in the  $x = 0$  plane, the antenna PWS  $\bar{A}(k_y, k_z)$  can be expressed as,

$$\bar{A}(k_y, k_z) = \frac{1}{(2\pi)^2} \int_{-\infty}^{\infty} \int_{-\infty}^{\infty} \bar{E}_t(0, y, z) e^{j(k_y y + k_z z)} dy dz, \quad (5-1)$$

where  $k_x = k_0 \sin \theta \cos \phi$ ,  $k_y = k_0 \sin \theta \sin \phi$ ,  $k_z = k_0 \cos \theta$ ,  $k_0 = 2\pi/\lambda$ ,  $\bar{E}_t(0, y, z) = \hat{y}E_y(0, y, z) + \hat{z}E_z(0, y, z)$  is the electric field transverse to  $x$  and an  $e^{j\omega t}$  time dependence is suppressed.

Equation (5-1) expresses the transverse antenna spectrum  $\bar{A}(k_y, k_z)$  as the Fourier transformation of the transverse aperture electric field  $\bar{E}_t$ . Via the inverse transformation the transverse to  $x$  electric field in the charge-free region  $x > 0$  can be expressed as [11,35]

$$\bar{E}_t(x, y, z) = \int_{-\infty}^{\infty} \int_{-\infty}^{\infty} \bar{A}(k_y, k_z) e^{-j\vec{k} \cdot \vec{r}} dk_y dk_z, \quad (5-2)$$

where  $\vec{k} = \hat{x}k_x + \hat{y}k_y + \hat{z}k_z$  and  $\vec{r} = \hat{x}x + \hat{y}y + \hat{z}z$ .

In the far-field where  $x \gg 0$ , an asymptotic expression can be derived by the method of steepest descent as,

$$\bar{E}_t(r, \theta, \phi) = j2\pi k_x \bar{A}(k_{y0}, k_{z0}) \frac{e^{-jk_0 r}}{r}, \quad (5-3)$$

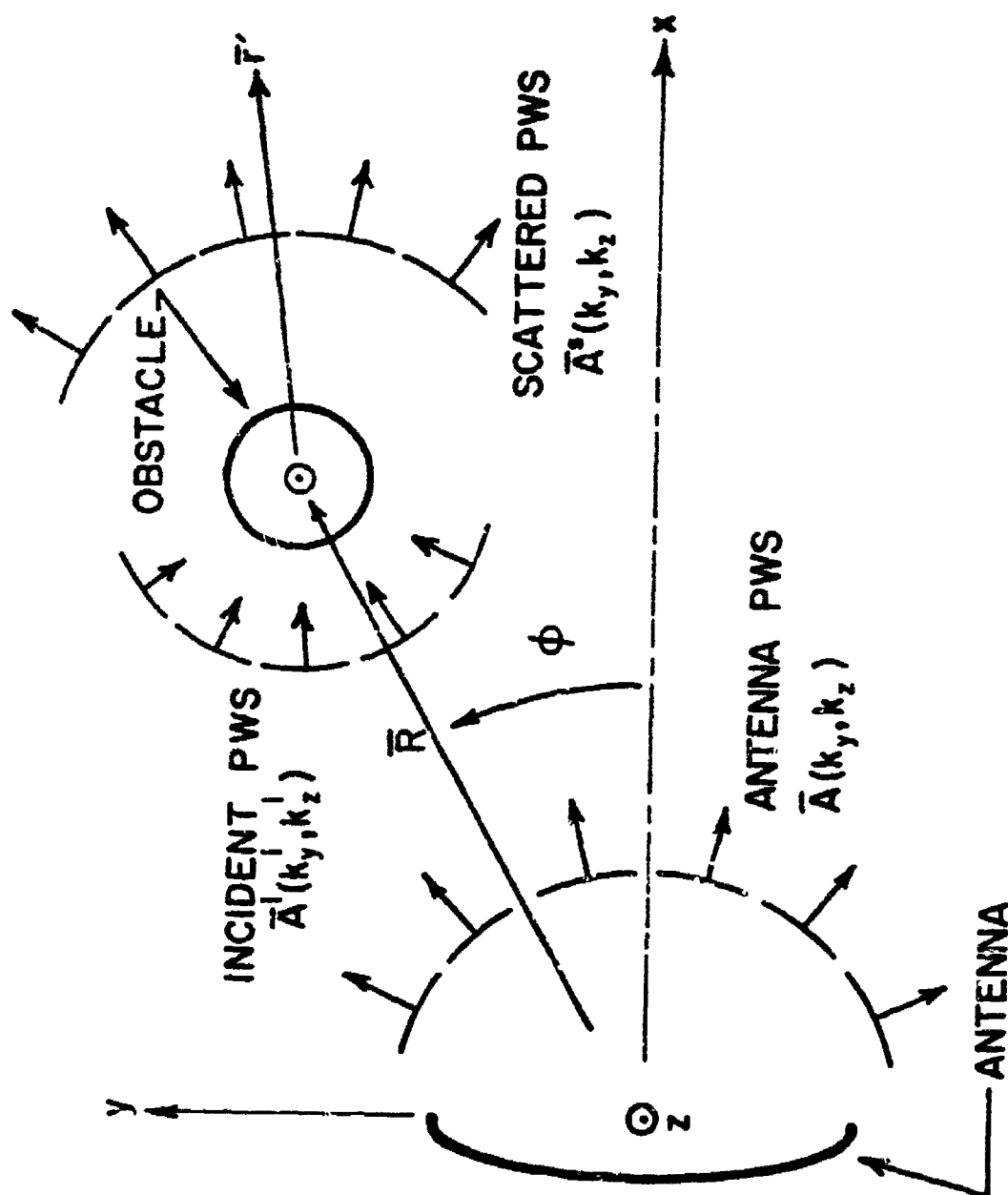


Figure 3-1. Diagram of the antenna/obstacle geometry and the plane wave spectra used in the scattering analysis.

where the wavenumbers  $k_{y0}$  and  $k_{z0}$  are the values of  $k_y$  and  $k_z$  at the saddle point of the integral of Equation (5-2).

The far-zone scattered field due to a single component of the plane wave spectrum incident on the obstacle shown in Figure 5-1 can be expressed as

$$\bar{E}_t^s(r', \theta, \phi) = \bar{\mathcal{D}}(k_y, k_z; k_y^i, k_z^i) \cdot \bar{A}^i(k_y^i, k_z^i), \quad (5-4)$$

where  $\bar{A}^i(k_y, k_z) = \bar{A}(k_y, k_z) e^{-jk_i \cdot \bar{R}}$ ,  $\bar{R}$  denotes the obstacle location and  $\bar{\mathcal{D}}$  is the plane wave to spherical wave scattering dyad for the obstacle with phase reference at the obstacle location. The incident wavenumber  $\bar{k}^i$  is given by

$$\bar{k}^i = \hat{x} \sqrt{k_0^2 - (k_y^i)^2 - (k_z^i)^2} + \hat{y} k_y^i + \hat{z} k_z^i, \quad (5-5)$$

and the term  $e^{-jk_i \cdot \bar{R}}$  shifts the antenna spectrum to the obstacle reference center located at  $\bar{R}$ .

For our purpose, it is convenient to express Equation (5-4) as

$$\bar{A}^s(k_y, k_z) = \bar{S}(k_y, k_z; k_y^i, k_z^i) \cdot \bar{A}^i(k_y^i, k_z^i), \quad (5-6)$$

where by using the asymptotic relation of Equation (5-3)

$$\bar{S}(k_y, k_z; k_y^i, k_z^i) = \frac{r'_0 e^{jk_0 r'_0}}{j2\pi k_x} \bar{\mathcal{D}}(k_y, k_z; k_y^i, k_z^i). \quad (5-7)$$

is the plane wave spectrum scattering dyad that specifies the obstacle scattered plane wave spectrum for the case of excitation by an incident plane wave traveling in the direction defined by  $(k_y^i, k_z^i)$ .

The total obstacle scattered plane wave spectrum can now be expressed as a superposition of the scattered spectra due to each component of the incident antenna spectrum as,

$$\bar{A}^s(k_y, k_z) = \int_{-k_{zL}}^{k_{zL}} \int_{-k_{yL}}^{k_{yL}} \bar{S}(k_y, k_z; k_y^i, k_z^i) \cdot \bar{A}^i(k_y^i, k_z^i) dk_y^i dk_z^i, \quad (5-8)$$

where  $k_{yL}$  and  $k_{zL}$  are the wavenumber limits of the incident spectrum.

In practice, it is more convenient to evaluate Equation (5-8) in the angle  $(\theta, \phi)$  space since most computer programs for scattering analysis employ  $(\theta, \phi)$  coordinates. This transformation results in,

$$\bar{A}^s(\theta, \phi) = -k_o^2 \int_{\theta_L}^{\theta_L} \int_{\phi_L}^{\phi_L} \bar{S}(\theta, \phi; \theta^i, \phi^i) \cdot \bar{A}(\theta^i, \phi^i) \sin^2 \theta^i \cos \phi^i d\theta^i d\phi^i, \quad (5-9)$$

where  $\theta_L$  and  $\phi_L$  are the angular limits on the incident spectrum space.

It is also convenient to express the scattering dyad in terms of spherical coordinates as

$$\bar{S}(\theta, \phi; \theta^i, \phi^i) = \begin{pmatrix} \hat{\phi}\hat{\phi} S_{\phi\phi} & \hat{\phi}\hat{\theta} S_{\phi\theta} \\ \hat{\theta}\hat{\phi} S_{\theta\phi} & \hat{\theta}\hat{\theta} S_{\theta\theta} \end{pmatrix}, \quad (5-10)$$

where  $S_{\phi\theta}$  is the scattering function for the  $\phi$ -polarized component of the scattered field for a  $\theta$ -polarized incident plane wave and so forth. It is apparent that this form fits nicely with scattering analyses expressed in terms of the conventional TE and TM incident plane wave modes, and the scattered spectra for the obstacle are readily expressed in terms of orthogonal  $(\theta, \phi)$  components [11].

The resulting total spectrum is given by the sum of the antenna and scattered spectra in the  $(\theta, \phi)$  space as,

$$\bar{A}_{\text{total}}(\theta, \phi) = \hat{\theta}[\bar{A}_{\theta}(\theta, \phi) + \bar{A}_{\theta}^s(\theta, \phi)] + \hat{\phi}[\bar{A}_{\phi}(\theta, \phi) + \bar{A}_{\phi}^s(\theta, \phi)], \quad (5-11)$$

and the composite far-zone pattern can be readily obtained from the total spectrum.

The spectrum  $\bar{A}(k_y, k_z)$  which is derived via the Fourier transformation of the transverse to  $\hat{x}$  electric field  $\bar{E}(0, y, z)$  is termed the "transverse vectorial spectrum" [21]. Since far-zone radiation patterns are conventionally expressed in terms of the angular  $(\theta, \phi)$  coordinates, and it is sometimes convenient to evaluate the scattering matrix for  $(\theta, \phi)$  coordinates, it is often necessary to convert the transverse vectorial spectrum expressed in the  $(x, y, z)$  cartesian coordinates to the  $(\theta, \phi)$  angular coordinates. To accomplish this transformation, we define after Kerns [21], the orthogonal unit vectors

$$\hat{k}_1 = \frac{(\hat{y}k_y + \hat{z}k_z)}{\sqrt{k_y^2 + k_z^2}}, \quad (5-12)$$

and

$$\hat{k}_2 = \hat{x} \times \hat{k}_1. \quad (5-13)$$

Note that the unit vectors  $\hat{k}_1$  and  $\hat{k}_2$  are respectively "radial" and "tangential" unit vectors associated with polar coordinates in the  $(y, z)$  plane. The individual plane wave components of the spectrum propagate in the plane defined by  $\hat{k}_1$  and the  $\hat{x}$  axis. Thus an electric field aligned with  $\hat{k}_1$  is parallel to the plane of incidence ( $E_{TM}$  or Transverse Magnetic) and an electric field aligned with  $\hat{k}_2$  is perpendicular to the plane of incidence ( $E_{TE}$  or Transverse Electric).

The scalar spectral density functions corresponding to the basis vectors  $\hat{k}_1$  and  $\hat{k}_2$  for the outgoing vectorial spectrum are defined as

$$\begin{aligned} b(1, \bar{k}) &= \hat{k}_1 \cdot \bar{A}(\bar{k}), \\ b(2, \bar{k}) &= \hat{k}_2 \cdot \bar{A}(\bar{k}), \end{aligned} \quad (5-14)$$



where  $\bar{K} = \hat{y}k_y + \hat{z}k_z$

Finally, the complete vectorial spectrum  $\bar{a}(\bar{K})$  which includes all of the cartesian (x,y,z) components of the outgoing spectrum is given by the relation

$$\bar{a}(\bar{K}) = b(1,\bar{K}) \left[ \bar{K}_1 + \hat{x} \frac{\bar{K}}{k_x} \right] + b(2,\bar{K}) \hat{K}_2, \quad (5-15)$$

where

The complete cartesian based vectorial spectrum  $\bar{a}(\bar{K})$  can then be converted to the angular  $(\hat{r}, \hat{\theta}, \hat{\phi})$  basis vectors via the relations

$$\begin{aligned} \hat{x} &= \hat{r} \sin\theta \cos\phi + \hat{\theta} \cos\theta \cos\phi - \hat{\phi} \sin\phi, \\ \hat{y} &= \hat{r} \sin\theta \sin\phi + \hat{\theta} \cos\theta \sin\phi + \hat{\phi} \cos\phi, \text{ and} \\ \hat{z} &= \hat{r} \cos\theta - \hat{\theta} \sin\theta. \end{aligned} \quad (5-16)$$

The foregoing analysis which was described for a single mast obstacle is applicable to any number of obstacles. It is only necessary to specify the scattering dyad  $\bar{S}$  for the obstacle cluster and the vector  $\bar{K}$  from the antenna to a designated phase reference center.

The PWS dyad  $\bar{S}$  for the obstacle or group of obstacles may be specified from theory or experiment. The PWS dyad can be constructed from GTD, physical optics or the Method of Moments solutions. The PWS dyad for multiple obstacles must account for multiple scattering among the obstacles in order to achieve accurate results for closely spaced scatterers [39]. However, accurate approximate equations are available only for collections of parallel cylinders or spheres of small diameter. Generalized practical techniques for constructing the PWS dyad for closely spaced obstacles of arbitrary shapes are not available at the present time. Accordingly, this remains as one of the most important problem areas in the analysis of site effects for many real-world antenna installations.

The PWS technique is readily adapted for wideband antenna analysis.

The extension to wideband stochastic in-band and out-of-band situations is presented and discussed in the following paragraphs.

## 2. Wideband Analysis

It will be advantageous to write the total electric field for radian frequency  $\omega = 2\pi f$  as

$$\begin{aligned} \bar{E}(\omega, r, \theta, \phi) = & \frac{j h(\theta, \phi) \exp[-j\omega(r/c)]}{cr} \\ & \cdot \omega [A^a(\omega, \theta, \phi) + \exp[j\omega(\frac{\hat{K} \cdot \bar{R}}{c})] A^s(\omega, \theta, \phi)] \end{aligned} \quad (5-17)$$

where

$\bar{E}(\omega, r, \theta, \phi)$  = total field,

$h(\theta, \phi) = \sin\theta \cos\phi$

$\hat{K} = \sin\theta \cos\phi \hat{x} + \sin\theta \sin\phi \hat{y} + \cos\theta \hat{z}$

$c$  = the speed of light in free space

where the superscripts  $a$  and  $s$  on  $\bar{A}$  denote the antenna and scatterer, respectively. The scattered antenna spectrum  $\bar{A}^s$  in Equation (5-17) is referred to a coordinate origin located in the geometrical center of the scatter. The exponential factor  $\exp[j\omega(\hat{K} \cdot \bar{R}/c)]$  "moves" the scattered spectrum to location of the origin of the antenna rotation coordinates. The quantity  $(1/cr)$  will be suppressed in the remaining equations, and the total field will be written as  $\bar{E}(\omega, \theta, \phi)$  in recognition that the factor  $(1/cr)$  is being suppressed.

The antenna spectrum function  $\bar{A}^a(\omega, \theta, \phi)$  for an overmoded reflector antenna is comprised of the weighted sum of spectrums for all of the propagating modes in the antenna feed system. Hence, the resultant antenna spectrum is

$$\bar{A}^a(\omega, \theta, \phi) = \sum_{\mu} a_{\mu}(\omega) \bar{A}_{\mu}(\omega, \theta, \phi) \quad (5-18)$$

where

$a_{\mu}(\omega)$  = the complex excitation coefficient for the  $\mu$ th waveguide mode for frequency  $\omega$ , and

$A_{\mu}(\omega, \theta, \phi)$  = the antenna spectrum produced by the  $\mu$ th waveguide mode.

It then follows that the scattered spectrum function  $\bar{A}^s(\omega, \theta, \phi)$  is

$$\bar{A}^s(\omega, \theta, \phi) = \sum_{\mu} a_{\mu}(\omega) \bar{A}_{\mu}^s(\omega, \theta, \phi) \quad (5-19)$$

where

$$\begin{aligned} \bar{A}_{\mu}^s(\omega, \theta, \phi) = & -\left(\frac{\omega}{c}\right)^2 \int_{\theta_L}^{\pi-\theta_L} \int_{-\phi_L}^{\phi_L} \{S(\omega | \theta, \phi; \theta', \phi') \cdot \bar{A}_{\mu}^a(\omega, \theta', \phi') \\ & \cdot \exp[-j \frac{\omega}{c} [(\sin(\theta)\cos(\phi))X + [\sin(\theta')\sin(\phi')]Y + [\cos(\theta')]Z \\ & \cdot \sin^2(\theta')\cos(\phi')d\phi' d\theta'] \} \end{aligned} \quad (5-20)$$

The deterministic power density  $P(\omega, \theta, \phi)$  at observation angles  $(\theta, \phi)$  for frequency  $\omega$  is proportional to  $\bar{E}^*(\omega, \theta, \phi) \cdot \bar{E}(\omega, \theta, \phi)$  and is written explicitly in terms of the complex mode excitation coefficients  $a(\omega)$  as

$$P(\omega, \theta, \phi) = \sum_{\mu} \sum_{\mu} a_{\mu}^*(\omega) a_{\mu}(\omega) P_{\mu, \mu}(\omega, \theta, \phi) \quad (5-21)$$

where

$$\begin{aligned} P_{\mu, \mu}(\omega, \theta, \phi) = & \omega^2 h^2(\theta, \phi) [A_{\mu}^{a*}(\omega, \theta, \phi) A_{\mu}^a(\omega, \theta, \phi) + A_{\mu}^{s*}(\omega, \theta, \phi) A_{\mu}^s(\omega, \theta, \phi) \\ & + \exp[+j\omega \frac{\hat{K} \cdot \bar{R}}{c}] A_{\mu}^{a*}(\omega, \theta, \phi) A_{\mu}^s(\omega, \theta, \phi) \\ & + \exp[-j\omega \frac{\hat{K} \cdot \bar{R}}{c}] A_{\mu}^a(\omega, \theta, \phi) A_{\mu}^{s*}(\omega, \theta, \phi)] \end{aligned} \quad (5-22)$$

The statistical average power density  $\langle P(\omega, \theta, \phi) \rangle$  is obtained from Equation (5-21) by statistically averaging over the product  $a_{\mu'}^*(\omega) a_{\mu}(\omega)$  of the complex mode excitation coefficients. The waveguide mode excitations generally are correlated, and so the stochastic average value  $\langle P(\omega, \theta, \phi) \rangle$  of the power density is written in the form

$$\begin{aligned} \langle P(\omega, \theta, \phi) \rangle = & \sum_{\mu'} \sum_{\mu} \langle a_{\mu'}^*(\omega) \rangle \langle a_{\mu}(\omega) \rangle P_{\mu', \mu}(\omega, \theta, \phi) \\ & + \sum_{\mu} \sigma_{\mu}^2(\omega) P_{\mu\mu}(\omega, \theta, \phi) \\ & + \sum_{\mu'} \sum_{\mu} c_{\mu', \mu}(\omega) P_{\mu', \mu}(\omega, \theta, \phi) \end{aligned} \quad (5-23)$$

where

$\sigma_{\mu}^2(\omega)$  = the variance of the  $\mu$ th mode coefficient,  
 $c_{\mu', \mu}(\omega)$  = the covariance function for the  $\mu$ th mode coefficient  
 and the conjugate of the  $\mu'$ th mode, and

where the primes on the last double sum signify that only terms  $\mu \neq \mu'$  are included in the sum.

Equations (5-21) and (5-23) are the appropriate equations for obtaining average power patterns over designated frequency intervals for deterministic and random situations, respectively. This process has been described and numerically simulated in Section II for a phased array antenna. Equations for time domain analysis are needed. Accordingly, attention is focused on the time domain response in the following paragraphs.

The time domain electric field  $E(t, \theta, \phi)$  can be computed as the discrete Fourier transform of the frequency domain response  $E(\omega_n, \theta, \phi)$  as

$$\bar{E}(t, \theta, \phi) = \frac{1}{2\pi} \sum_n \bar{E}(\omega_n, \theta, \phi) H(\omega_n) \exp[j\omega_n t] \quad (5-24)$$

where  $H(\omega_n)$  is the pulse spectrum function and where the summation is over a set of frequencies exceeding twice the bandwidth of the input pulse spectrum. The  $\bar{E}(\omega_n, \theta, \phi)$  in Equation (5-24) are the frequency domain fields obtained when the input frequency spectrum is uniformly weighted in amplitude. The time domain power density  $P(t, \theta, \phi)$  proportional to  $E^*(t, \theta, \phi)E(t, \theta, \phi)$  and is written explicitly as

$$P(t, \theta, \phi) = \frac{1}{4\pi^2} \sum_n \sum_n \{ \bar{E}^*(\omega_n, \theta, \phi) \bar{E}(\omega_n, \theta, \phi) d^*(\omega_n) H(\omega_n) \exp[j(\omega_n - \omega_n)t] \} \quad (5-25)$$

This equation for  $P(t, \theta, \phi)$  can be expressed directly in terms of the mode propagation coefficients  $a(\omega)$  as

$$P(t, \theta, \phi) = \frac{1}{4\pi^2} h^2(\theta, \phi) \sum_n \sum_n \sum_{\mu} \sum_{\mu} \{ a_{\mu}^*(\omega_n) a_{\mu}(\omega_n) \omega_n \omega_n \cdot H^*(\omega_n) H(\omega_n) \exp[j(\omega_n - \omega_n) \frac{n}{c}] \cdot P_{n'n\mu'\mu}(\omega_n, \omega_n | \theta, \phi) \} \quad (5-26)$$

where

$$\begin{aligned} P_{n'n\mu'\mu}(\omega_n, \omega_n | \theta, \phi) = & \{ \bar{A}_{\mu'}^{a*}(\omega_n, \theta, \phi) \bar{A}_{\mu}^a(\omega_n, \theta, \phi) \\ & + \bar{A}_{\mu'}^{s*}(\omega_n, \theta, \phi) \bar{A}_{\mu}^s(\omega_n, \theta, \phi) \\ & + \exp[j\omega \frac{\hat{K} \cdot \hat{R}}{c}] \bar{A}_{\mu'}^{a*}(\omega_n, \theta, \phi) \bar{A}_{\mu}^s(\omega_n, \theta, \phi) \\ & + \exp[-j\omega \frac{\hat{K} \cdot \hat{R}}{c}] \bar{A}_{\mu}^{a*}(\omega_n, \theta, \phi) \bar{A}_{\mu'}^s(\omega_n, \theta, \phi) \} \end{aligned} \quad (5-27)$$

and where all other symbols have been previously defined. Equation (5-26) is the appropriate equation for computing the power density envelope of the radiated pulse at the far-field observation point  $(\theta, \phi)$  for a specified input time pulse whose spectrum is  $H(\omega_n)$ . The pulse amplitude envelope is, of course, the square root of  $P(t, \theta, \phi)$ . The statistical average value of the power density envelope of the time pulse is obtained by statistically averaging over the mode coefficient products  $a_{\mu}(\omega_n) \cdot a_{\mu}^*(\omega_n)$ . Making use of the fact that the mode coefficients for different frequencies are uncorrelated, the statistical average value  $\langle P(t, \theta, \phi) \rangle$  of  $P(t, \theta, \phi)$  is written as

$$\begin{aligned} \langle P(t, \theta, \phi) \rangle = & \frac{1}{4\pi^2} h^2(\theta, \phi) \sum_n \sum_{\mu} \sum_{\mu'} \{ \langle a_{\mu}^*(\omega_n) \rangle \langle a_{\mu}(\omega_n) \rangle \\ & (\mu' \neq \mu) \\ & \omega_n, \omega_{n'} E^*(\omega_n) H(\omega_n) \exp[j(\omega_n - \omega_{n'})r/c] \cdot P_{n\mu\mu'}(\omega_n, \omega_{n'} | \theta, \phi) \} \\ & + \sum_n \sum_{\mu} \sum_{\mu'} \{ \omega_n^2 H^*(\omega_n) H(\omega_n) \\ & - P_{n\mu\mu'}(\omega_n, \omega_n | \theta, \phi) \cdot C_{\mu\mu'}(\omega, \theta, \phi) \} \end{aligned} \quad (5-28)$$

The statistical average value of the envelope of the pulse amplitude cannot be obtained by taking the square root of Equation (5-28) because the average value of the square root of a random variable is not equal to the square root of the average value. The statistical average value of the amplitude of the pulse can be computed numerically with the aid of the Nakagami p.d.f. if it is needed. However, the statistical average value of the envelope of the pulse power density given by Equation (5-28) is the quantity of interest in this study.

### C. Time Domain Simulations

Numerical computations were performed to compute the pulse envelope power density of non-random pulses radiated by a waveguide horn-fed reflector antenna for both in-band and out-of-band operation in the presence of a nearby metallic cylinder. The computations were made with aid of existing computer programs APATT and MBD previously

developed at Georgia Tech [6, 38]. APATT was used to generate the clear-site in-band and out-of-band antenna patterns as a function of frequency. MBD was employed to compute the total electric field (antenna + scatterer) versus frequency for the antenna/obstacle situations. The radiated pulse power density was calculated via Equation (5-21).

The antenna used for the simulations is a 4-foot diameter paraboloidal reflector antenna fed by a waveguide horn. The design in-band center frequency is 3.0 GHz and the design in-band antenna polarization is vertical. The waveguide portion of the feed system consists of a 6-inch long section of standard WR- S-band waveguide excited by a coax-to-waveguide adapter. The antenna operates in the presence of a 12-foot tall, 2-foot diameter metal cylinder located within the near-field of the antenna.

Plots of the radiated pulse power density envelope are shown in Figures 5-2 through 5-7 for a single input rectangular pulse of two nanoseconds duration. Figures 5-2 and 5-3 show the radiated pulses for in-band operation of the antenna while Figures 5-4 through 5-7 show the radiated pulses for out-of-band operation of the antenna. The plots are sequenced as follows. Figures 5-2 and 5-3 show the radiated pulse in the antenna boresight (0-degree) direction for the clear site and the blocked condition, respectively. Figures 5-4 and 5-5 show the out-of-band radiated pulse in the boresight direction antenna boresight for clear-site and blocked operation, respectively. Similarly, Figures 5-6 and 5-7 show the out-of-band radiated pulse in a sidelobe region for the clear site and blocked situations, respectively. For the blocked case, the metal cylinder was located six feet away from the antenna along the 50° radial. The four out-of-band figures are sequenced in the same manner and the obstacle was located at the same position just described for the in-band computations.

The in-band pulses were computed from the antenna or antenna/obstacle electric field for frequencies from 2.0 GHz to 4.0 GHz in 0.05 GHz steps. Similarly, the out-of-band pulses were computed from the antenna or antenna/obstacle electric fields for frequencies from 5.5 GHz to 7.5 GHz in 0.05 GHz steps. The pulse carrier frequencies

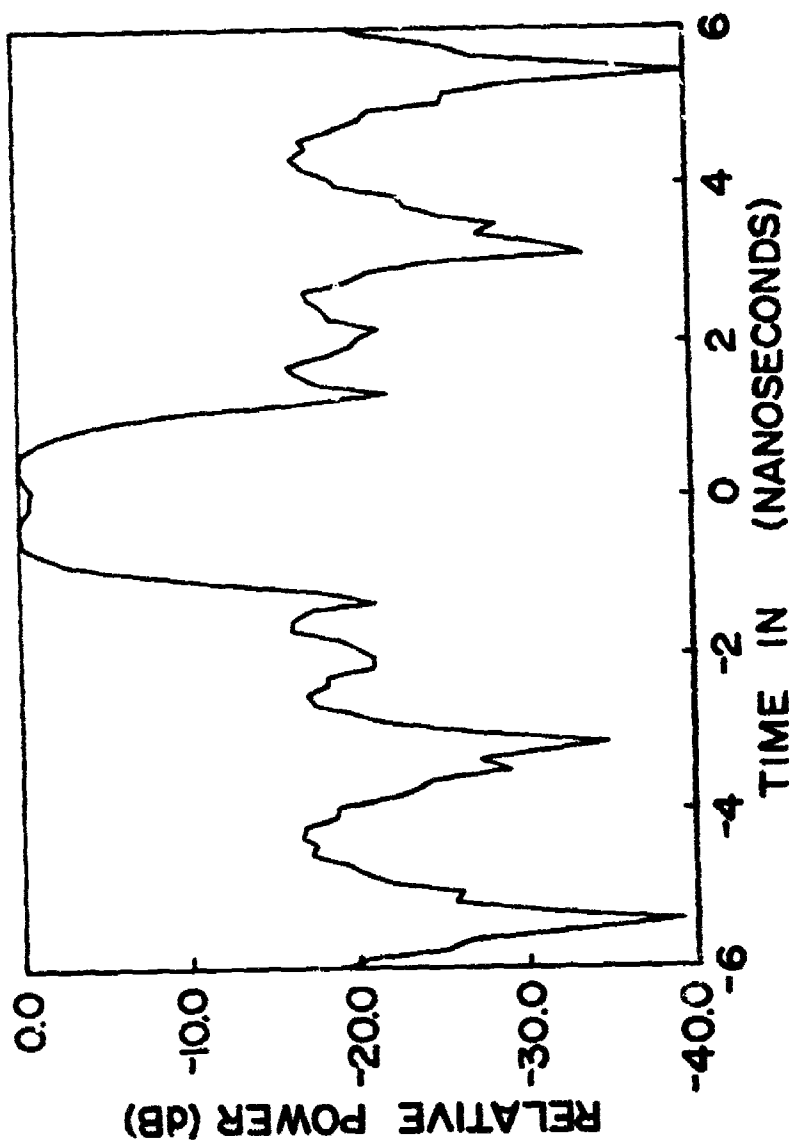


Figure 5-2. Radiated pulse envelope in the antenna boresight direction for the unobstructed 4.0-foot diameter reflector antenna for an input 2.0-nanosecond rectangular pulse with carrier frequency at the in-band frequency of 3.9 GHz.



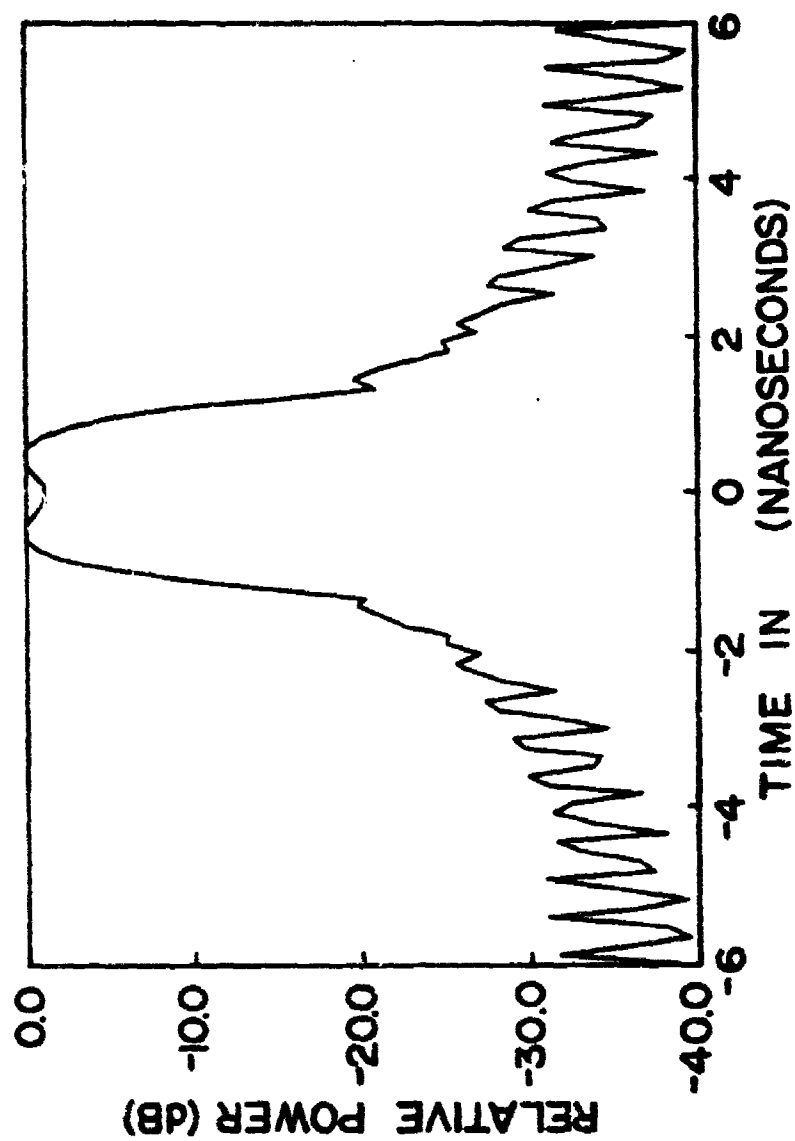


Figure 5-3. Radiated pulse envelope in the boresight direction for the 4.0-foot diameter reflector antenna partially blocked by a 2.0-foot diameter cylinder located 6.0 feet away along the 5.0-degree radial for an input 2.0-nanosecond rectangular pulse with carrier frequency at the in-band frequency of 3.0 GHz.

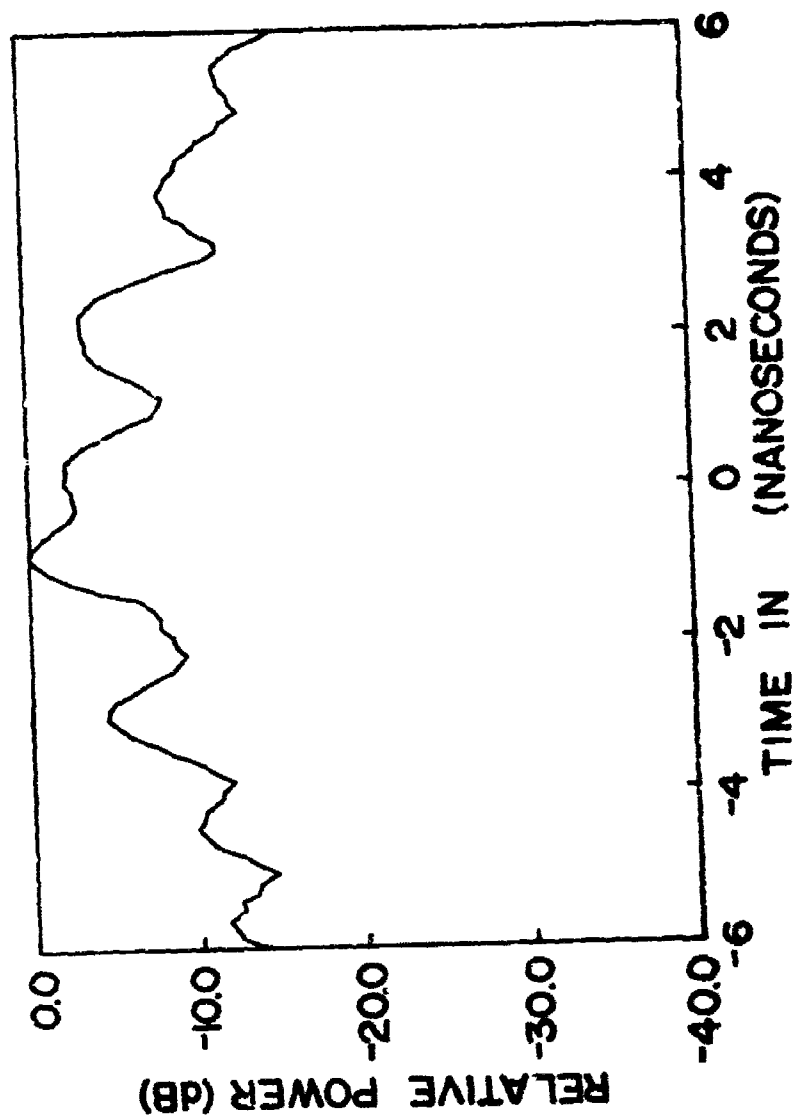


Figure 5-4. Radiated pulse envelope in the antenna boresight direction for the unobstructed 4.0-foot diameter reflector antenna for an input 2.0-nanosecond rectangular pulse with carrier frequency at the out-of-band frequency of 6.5 GHz.

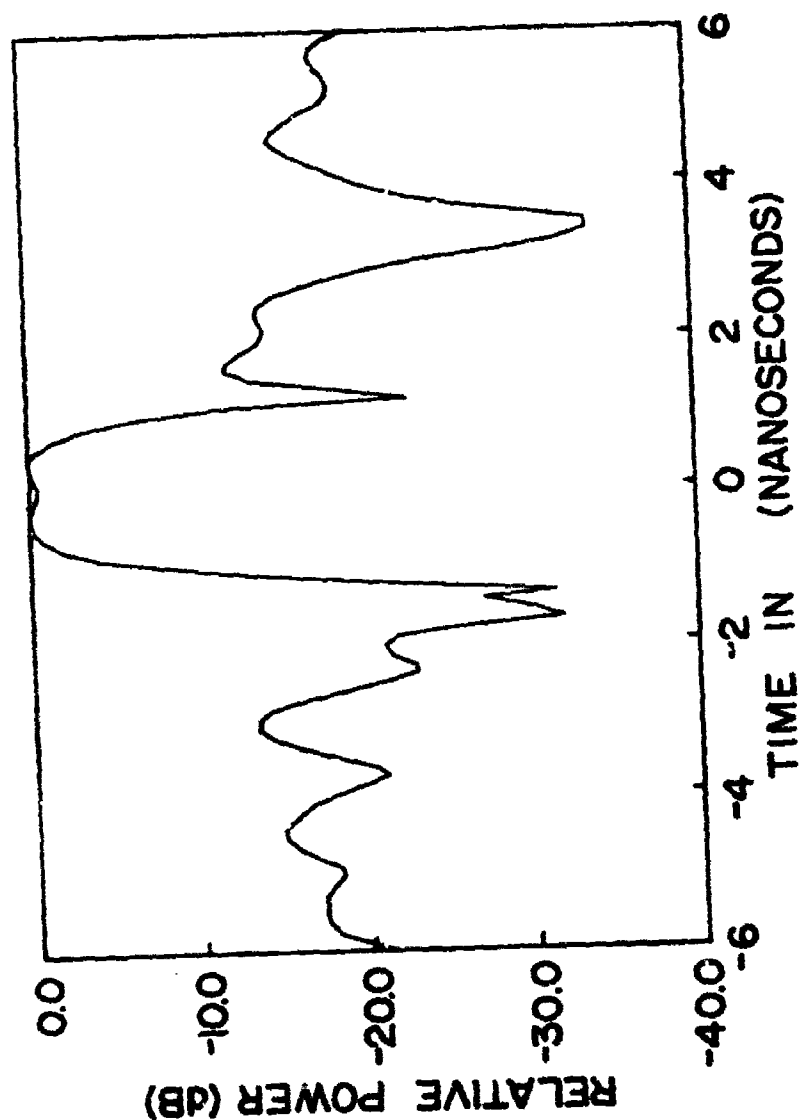


Figure 5-5. Radiated pulse envelope in the antenna boresight direction for the 4.0-foot diameter reflector antenna partially blocked by a 2.0-foot diameter cylinder located 6.0 feet away along the 5.0-degree radial for an input 2.0-nanosecond rectangular pulse with carrier frequency at the out-of-band frequency of 6.5 GHz.

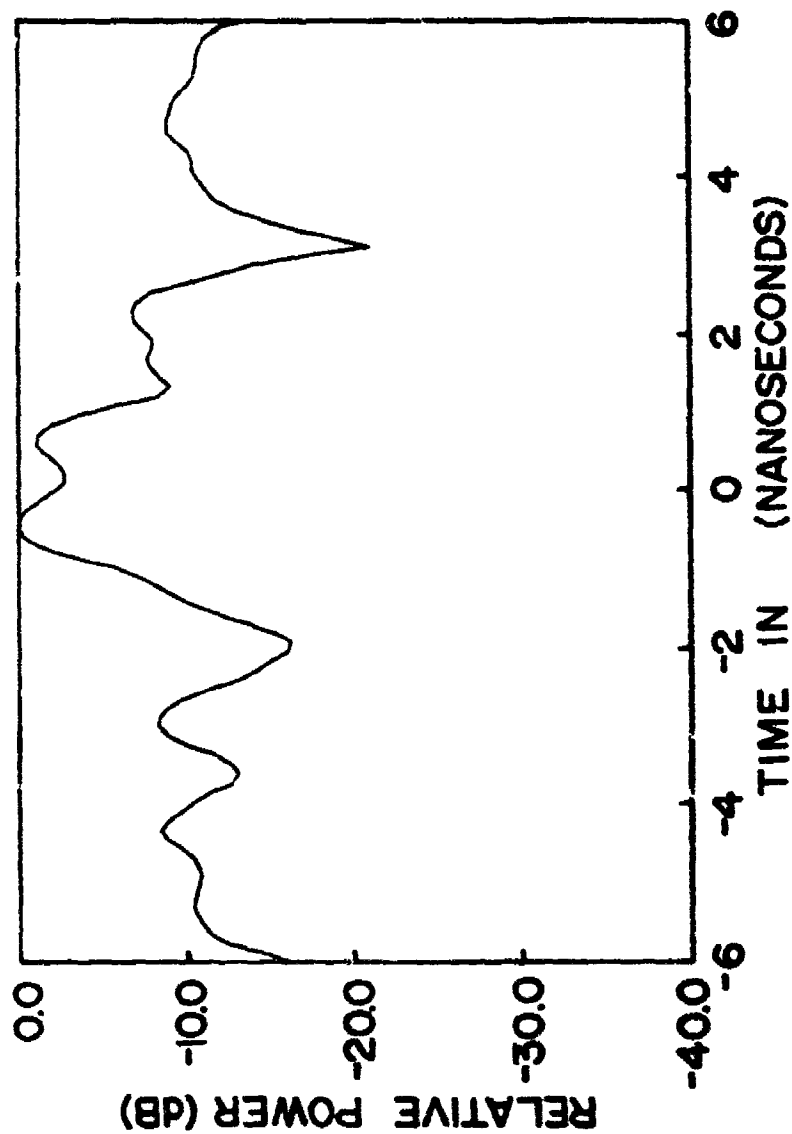


Figure 5-6. Radiated pulse envelope at 6.0 degrees off the antenna boresight direction for the unobstructed 4.0-foot diameter reflector antenna for an input 2.0-nanosecond rectangular pulse with carrier frequency at the out-of-band frequency of 6.5 GHz.

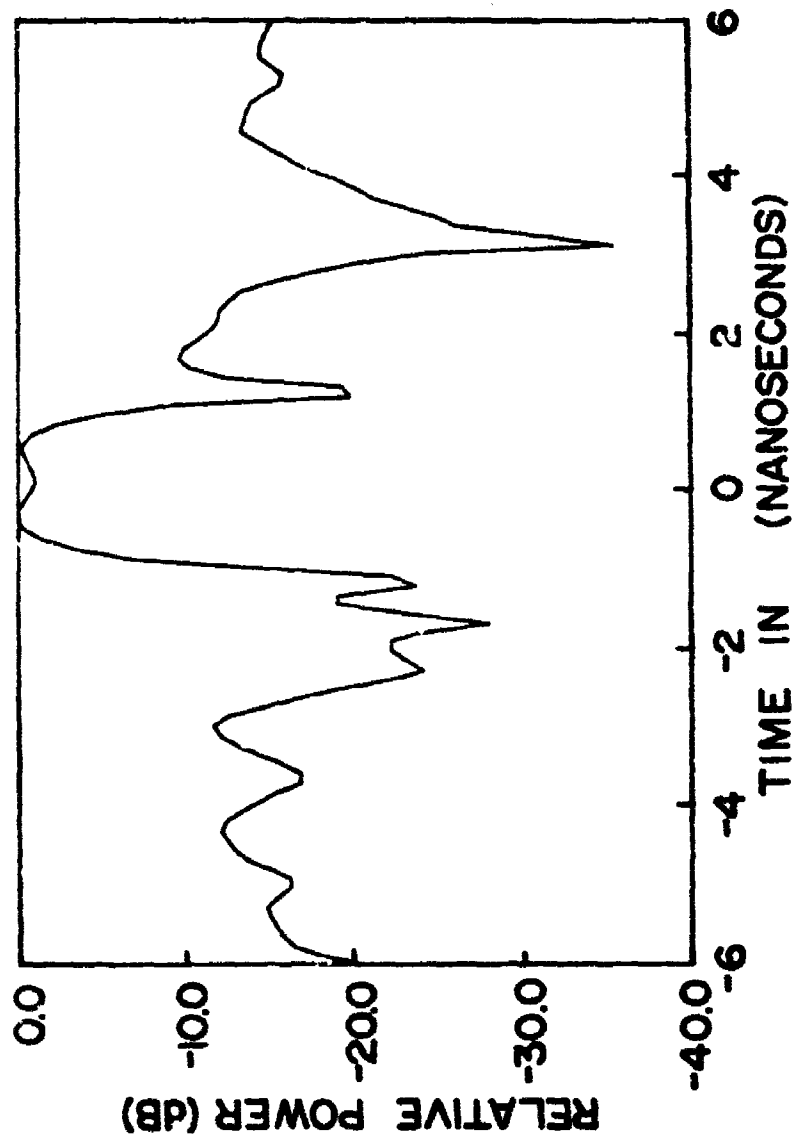


Figure 5-7. Radiated pulse envelope at 6.0 degrees off the antenna boresight direction for the 4.0-foot diameter reflector antenna partially blocked by a 2.0-foot diameter cylinder located 6.0 feet away along the 5.0-degree radial for an input 2.0-nanosecond rectangular pulse with carrier frequency at the out-of-band frequency of 6.5 GHz.

for the in-band and out-of-band pulses are 3.0 GHz and 6.5 GHz, respectively.

The waveguide power flow for the in-band computations was entirely in the  $TE_{10}$  mode. The waveguide power flow was randomly distributed among the allowed modes for the out-of-band computations. In particular, the mode coefficients at each incremental frequency were obtained from a random draw via a pseudo-random number generator. The statistical average power for each allowed mode was chosen to be  $(1.0/N)$  watt, where  $N$  is the total number of allowed modes at a particular frequency.

The in-band pulses displayed in Figures 5-2 and 5-3 are noticeably distorted. In particular, the radiated pulses for both the clear-site and partially blocked situations are characterized by the appearance of time sidelobes and noticeable increase in the pulsewidth, as expected from theory. The pulse for the partially blocked antenna suffers less distortion than the pulse for the unobstructed antenna. This result is attributed to the fact that the variations in the amplitudes and phases of frequency domain electric fields are less dramatic for the partially blocked antenna than for the unobstructed antenna.

The out-of-band pulses displayed in Figures 5-4 through 5-7 are severely distorted. The out-of-band pulses in the antenna boresight direction are considerably more distorted than their in-band counterparts. Of course, this result is expected because the electric field varies more dramatically over the out-of-band frequency interval than for the in-band frequency interval. The out-of-band pulse in the boresight direction for the unobstructed antenna does not resemble the input 2.0 nanosecond rectangular pulse. However, the out-of-band pulse in the boresight direction for the partially blocked antenna does resemble a rectangular pulse and the distortion is manifested primarily in the appearance of time sidelobes. The trend toward smaller pulse distortion for the partially blocked antenna for the pulses in the boresight direction is also evident in Figures 5-6 and 5-7 for the pulses radiated in the sidelobe directions.

The observed trend toward less distortion for the partially blocked antenna than for the unobstructed antenna is attributed to the

moderating effect of the scattering obstacle on the variations of the amplitude and phases of the electric field over the 2.0 GHz frequency interval. However, it should be noted that the 2.0 foot cylinder is large in terms of wavelength and, consequently, the scattered fields are less frequency sensitive than the scattered fields for resonant scatterers. Accordingly, it would be premature to generalize the distortion results to other scattering environments involving structures that have dimensions comparable to the wavelengths in the pulse spectrum, particularly those environments where dielectric scatterers are present. Additional analytical, numerical, and experimental research is needed in order to characterize the wideband cw and pulsed effects of arbitrary scattering environments.

## SECTION VI

### CONCLUDING REMARKS AND RECOMMENDATIONS

The research work described herein meets or exceeds the stated objectives for this basic research program. The overall main objective was to advance the state of knowledge concerning near-field theory and techniques for wideband radiating systems at in-band and out-of-band frequencies. This was achieved by the successful completion of four research tasks. The task objectives and the key results for each task are described below. These results are followed by recommendations for further research work in the four task areas.

#### A. Summary of Results

Task 1. Provide a near-field methodology to characterize electromagnetic emitter radiation patterns at in-band and out-of-band frequencies for wide bandwidth radiators. The objective of this task was to develop the appropriate theory and equations based on statistical analysis techniques for efficient characterization of wideband radiators.

The theory and equations were developed for characterizing the radiation patterns of wideband cw or pulsed antennas over both in-band and out-of-band frequency intervals from measured data collected via near-field measurement techniques. The results are applicable to either phased array or reflector antennas. Numerical simulations were performed for (1) a 20-element out-of-band waveguide phased array with no inter-element coupling. The effect of statistical correlations of the near-field data was studied and methods for handling correlation effects were derived. Useful approximations for the probability density function for the radiated power pattern statistics for correlated sources were also identified.

The key results obtained via the Task 1 efforts may be summarized as follows:

- (1) The statistical average patterns and standard deviations at selected frequencies can provide a very succinct engineering description of the important EMC characteristics of wideband CW multimoding antennas. The statistical average patterns and standard deviations are a practical



alternative to the comparatively more expensive and cumbersome Monte Carlo simulations.

- (2) The statistical average pattern for a given frequency may be computed from a knowledge of the following near-field statistical parameters:
  - (a) statistical average value of the electric field at all near-field measurement points,
  - (b) the standard deviation of the electric field at all measurement points, and
  - (c) the covariance functions for the electric fields at all different near-field measurement points.
- (3) The statistical average pattern versus time for a pulsed system depends on all of the above near-field statistical parameters listed in Item 2, and the following far-field statistical parameters:
  - (a) the statistical average value of the far-field electric field at all frequencies in the frequency band,
  - (b) the standard deviation of the far-field electric field at all frequencies in the frequency band, and
  - (c) the covariance functions of the electric field at all different frequencies in the frequency band.

However, the far-field statistical parameters listed above can be computed from the near-field statistical parameters. Thus, pulsed antennas characterization does not require knowledge of any additional statistical near-field data.

- (4) The probability density function (p.d.f.) for the far-field electric fields of correlated random sources or scatterers can be accurately approximated for most antenna or scattering problems via the use of Nakagami's p.d.f. and linear operator theory. A less accurate but relatively simple expression for the p.d.f. was also derived that is suitable for certain engineering applications.

Task 2. Theoretically relate the radiation pattern characterization to the basic data needed for efficient optimization analysis of electromagnetic spectrum usage. The objective of this task was to relate the near-field derived wideband antenna characterization to antenna coupling of antenna systems which co-exist in the same EM environment.

The efforts on this task were devoted to deriving approximate but accurate coupling prediction equations. Three different techniques for coupling analysis were considered. These three techniques are denoted respectively as (1) Plane Wave Spectrum (PWS), (2) Spherical Spectrum Wave (SWS), and (3) the Geometrical Theory of Diffraction (GTD). Most of the research efforts were devoted toward development of the PWS technique. Multiple scattering effects are not addressed in the analysis. However, multiple scattering effects can be approximately analyzed if the scattering matrix of each antenna is specified from theory or measurements. Theory and equations for the PWS, SWS, and GTD approaches were presented and discussed. Results of numerical simulations using the PWS approach for analyzing antenna coupling are also presented. The GTD technique for deterministic antenna analysis was adapted to yield comparatively simple equations for certain classes of antenna coupling problems.

The analyses for this task were conducted in the frequency domain. The primary goal was to obtain equations valid over wide frequency bandwidths. The time domain response can then be obtained by numerically computing the Fourier Transform of the frequency domain equations. The wideband frequency response of swept CW radiating systems is then characterized by numerically computing the frequency-averaged pattern and standard deviation.

Task 3. Provide the methodology to assess the effects of system devices (i.e., higher-order mode generation) on the radiation pattern. The two main objectives for this task were (1) to develop a method for analyzing the antenna pattern effects of higher order modes generated and/or propagated by common feed system devices and (2) to assess the feasibility of deducing the mode excitations for a radiating feed system from analysis of measured out-of-band pattern data.

Equations were derived during Task 1 and Task 2 to permit the out-of-band radiation pattern statistics to be computed from a knowledge of the system device statistics which describe the higher-order mode generation and propagation. Theory and equations for identifying the higher-order mode excitations of a feed containing passive and/or active waveguide devices through utilization of wideband or pulsed near-field measurements were also derived.

The timely completion of the required research work for this task permitted a brief digression into another important aspect of the out-of-band response of system devices. In particular, equations were sought to describe the influence of particular waveguide devices on the excitation and subsequent propagation of out-of-band waveguide modes. Three waveguide devices were considered in this exploratory study, namely (1) coax-to-waveguide adapters, (2) radial bends, and (3) ferrite phase shifters. Program constraints precluded a detailed quantitative analysis of all three kinds of devices. Accordingly, the research efforts were concentrated mainly on the theoretical and numerical analysis of a coax-to-waveguide adapter.

Task 4. Investigate the impact of site effects on the near-field antenna analysis technology. The objective of this task was to extend the existing monochromatic spectrum scattering matrix analysis to study antenna siting effects on the wideband and out-of-band performance of radiating systems.

A theoretical study was performed to investigate techniques and derive the equations for extending the existing monochromatic spectrum scattering matrix theory to analyze site effects over wide frequency bandwidths. In particular, frequency domain equations were derived via the Plane Wave Spectrum Scattering (PWSS) technique. The pulse envelope response is obtained from the Fourier Transform of the frequency domain PWSS equations. Based upon the results of the theoretical study, a numerical simulation of the site effects on the wideband in-band and out-of-band performance of a pulsed radiating system was performed for a reflector antenna partially blocked by a round metal cylinder located in the antenna's near-field.

#### B. Recommendations

The results of the research work conducted for this basic research program significantly advance the state of knowledge concerning near-field wideband in-band and out-of-band radiation and/or scattering phenomena. However, further advances can and should be made through additional research work. Accordingly, recommendations for further research work are presented herewith:

**Task 1.**

- (a) Conduct theoretical and numerical analyses to derive a reliable, accurate practical method to compute the near-field covariance functions from the near-field data obtained from a single probe.
- (b) Conduct theoretical and numerical analyses to derive the probability density function for correlated sources or scatterers.
- (c) Conduct theoretical and numerical analyses to derive the inter-element coupling and covariance functions for a multimoding array of out-of-band waveguide elements.
- (d) Conduct near-field measurements for a multimoding waveguide array to provide validation data for item (c).

**Task 2.**

- (a) Conduct theoretical and numerical analyses to derive antenna coupling model(s) that are valid for arbitrary orientations and locations of in-band as out-of-band wideband cw or pulsed reflector antennas in the presense of environmental scattering obstacles.
- (b) Conduct near-field antenna coupling measurements in the presence of selected scattering obstacles in order to provide validation data for item (a).

**Task 3.**

- (a) Conduct theoretical and numerical analyses to device improved approximate methods for computing the higher-order mode excitations and propagation constants for common waveguide components such as radial bends, ferrite phase shifters, coax-to-waveguide adapters, and waveguide rotary joints.
- (b) Conduct near-field measurements for multimoding feed systems to generate validation data for item (a) and to provide insight into realistic mode excitations encountered in real-world feed systems.

**Task 4.**

- (a) Conduct theoretical and numerical analyses to derive simplified expressions for making rapid but accurate approximate analyses of the wideband cw or pulsed response of reflectors or phased array antennas that are partially obstructed by one or more near-field obstacles.

- (b) Conduct experiments to measure the wideband cw or pulsed response of partially blocked antennas to provide validation data for item (a).

## SECTION VII

### REFERENCES

1. F. L. Cain, B. J. Cown, and E. E. Weaver, "Out-of-Band Frequency Investigations of Near-Field Obstacle Effects and Phased Arrays," Georgia Institute of Technology, Final Engineering Report, Contract N00024-73-C-1141, February 1974.
2. F. L. Cain, B. J. Cown, E. E. Weaver, and C. E. Ryan, "Far-Field Antenna Performance Investigations Concerning In-Band Effects of Near-Field Structures and Out-of-Band Phased Arrays," Georgia Institute of Technology, Final Engineering Report, Contract No. N00024-74-C-1215, January 1975.
3. B. J. Cown, F. L. Cain, and E. F. Duffy, "Statistical Prediction Model for EMC Analysis of Out-of-Band Phased Array Antennas," IEEE Transactions on Electromagnetic Compatibility, Vol. 18, No. 4, 163-170, November 1976.
4. B. J. Cown and C. E. Ryan, Jr., "Near-Field Theory and Techniques for Wideband Radiating Systems at In-Band and Out-of-Band Frequencies," Georgia Institute of Technology, Interim Technical Report No. 1, Contract DAAG-78-C-0029, January 1979.
5. B. J. Cown and C. E. Ryan, Jr., "Near-Field Theory and Techniques for Wideband Radiating Systems at In-Band and Out-of-Band Frequencies," Georgia Institute of Technology, Interim Technical Report No. 2, Contract DAAG-78-C-0029, March 1980.
6. T. B. Wells and C. E. Ryan, Jr., "Out-of-Band Reflector Antenna Model," Georgia Institute of Technology, Final Technical Report, Contract DAAG29-80-C-0083, May 1981.
7. B. J. Cown, E. E. Weaver, and C. E. Ryan, Jr., "Antenna Pattern Measurements to Characterize the Out-of-Band Behavior of Reflector Antennas," Georgia Institute of Technology, Final Technical Report, Contract F19628-80-C-0024, 30 September 1981.
8. A. Papoulis, Probability, Random Variables, and Stochastic Processes, McGraw-Hill, Inc., 1965.
9. B. J. Cown, C. E. Ryan, Jr., and P. Major, "Statistical Model for EMC Analysis of Wideband Phased Arrays," 1980 IEEE International Electromagnetic Compatibility Symposium Record, October 1980.
10. B. J. Cown, C. E. Ryan, Jr., A. L. Bridges, and J. D. Adams, "A Study of the Application of Near-Field Measurements for NASA Requirements," Georgia Institute of Technology, Final Technical Report, Contract NAS5-2234.

11. R. F. Harrington, Time Harmonic Electromagnetic Fields, McGraw-Hill Book Company, New York, 1961.
12. S. M. Selby, Standard Mathematical Tables, Chemical Rubber Co., Cleveland, Ohio, 1970.
13. J. H. Wilkinson, The Algebraic Eigenvalue Problem, Clarendon Press Oxford, 1965.
14. K. Tanabe, "Projection Method for Solving a Singular System of Linear Equations and its Applications," Numerical Mathematics, 17, Springer-Verlag 1971, pp. 203-214.
15. Larry E. Corey, "Analytical Compensation for Near-Field Probe Positioning Errors in Calculated Far-Field Antenna Patterns," Ph.D. Thesis, Electrical Engineering, Georgia Institute of Technology, Contract No. DAAG-78-C-0029, May 1980.
16. M. Nakagami, "The  $m$ -Distribution - A General Formula of Intensity Distribution of Rapid Fading," Statistical Methods in Radio Wave Propagation, W. C. Hoffman, editor, Pergamon Press, 1960.
17. P. Beckmann and A. Spizzichino, The Scattering of Electromagnetic Waves From Rough Surfaces, Pergamon Press, 1963.
18. S. O. Rice, "Mathematical Analysis of Random Noise," Bell System Technical Journal, 24, 1945, pp. 46-156.
19. R. S. Hoyt, "Probability Functions for the Modulus and Angle of the Normal Complex Variate," Bell System Technical Journal, 24, 1947, pp. 318-359.
20. Lord Rayleigh, The Theory of Sound, Sec. 42a, 3rd edition, London 1896.
21. D. M. Kerns, Plane Wave Scattering Matrix Theory of Antennas and Antenna-Antenna Interaction, NBS Monograph 162, U. S. Government Printing Office, Washington, 1981.
22. C. E. Ryan, Jr., E. E. Weaver and B. J. Cown, "Plane-Wave Spectrum Scattering Analysis of Near-Field Obstacle Effects on Directive Antenna Patterns," IEEE Transactions on Antennas and Propagation, Vol. 27, No. 6, November 1979, pp. 772-773.
23. F. L. Cain, C. E. Ryan, Jr., C. P. Burns, and B. J. Cown, "Near-Field Obstacle Effects and Phased Array Studies," Georgia Institute of Technology, Final Engineering Report, Contract No. N00024-71-C-1120, January 1972.
24. B. Ye. Kinber, "Decoupling of Closely Situated Reflector Aerials," Radiotekhnika i Elektronika 6, No. 6, 1961, pp. 907-916.

25. G. D. Bergland, "A Guided Tour of the Fast Fourier Transform," IEEE Spectrum, July 1969.
26. H. Bucholtz, "Der Einfluss der Krümmung von Rechteckigen Hohlleitern auf das Phasenmass Ultrakurzer Wellen," E. N. T., Vol. 16, 1939, pp. 73-85.
27. M. Jouget, "Les Effets de la Courbure et des Discontinuités de Courbure sur la Propagation des Ondes dans les Guides à Section Rectangulaire," Annales des Télécommunication, Vol. 2, No. 3, 1947, pp. 78-94.
28. M. Jouget, "Propagation dans les Tujaux Courbés," Comptes Rendus - Academie des Sciences, Paris, Jan. 6, 1947.
29. M. Jouget, "Effects of Curvature on the Propagation of Electromagnetic Waves in Guides of Circular Cross-Section," Câbles et Transmission, Paris, Vol. 1, No. 2, July 1947, pp. 133-153.
30. S. O. Rice, "Reflections from Circular Bends in Rectangular Waveguides - Matrix Theory," Bell System Technical Journal, Vol. 27, 1948, pp. 305-349.
31. J. A. Cochran and R. G. Pecina, "Mode Propagation in Continuously Curved Waveguides," Radio Science, Vol. 1, No. 6, June 1966, pp. 679-696.
32. C. P. Bates, "Intermodal Coupling at the Junction Between Straight and Curved Waveguides," Bell System Technical Journal, Vol. 48, September 1969, pp. 2259-2280.
33. E. Bakar and G. Govindarajan, "Rectangular and Annular Modal Analyses of Multimode Waveguide Bends," IEEE Transactions on Microwave Theory and Techniques, Vol. 21, December, 1973, pp. 819-824.
34. L. Lewin, D. C. Chang, and E. F. Kuester, Electromagnetic Waves and Curved Structures, Peter Peregrinus, Ltd., Southgate House, Stevenage, Herts. SG1 1HQ, England (IEE Publication) 1977.
35. R. E. Collin, Field Theory of Guided Waves, McGraw-Hill, New York, 1960.
36. A. Moshen, "On the Variational Solution of Electromagnetic Problems in Lossy Anisotropic Inhomogeneous Media," Journal of Physics A: Math. Gen., (Great Britain) Vol. 11, No. 8, pp. 1681-1686.
37. C. L. Bennett, "Time Domain Electromagnetics and Its Applications," Proceedings of the IEEE, March 1978, pp. 299-318.



38. C. E. Ryan, Jr., E. E. Weaver, and W. P. Cooke, "Development of Total Electromagnetic Effectiveness During Ship Design," Georgia Institute of Technology, Final Technical Report, Contract No. N00024-77-C-5338, December 1979.
39. B. J. Cown, R. L. Moore, and C. E. Ryan, Jr., "Measurement and Analysis of Directive Antenna Gain Loss Caused by Shipboard Multiple Obstacles," Georgia Institute of Technology, Final Technical Report, Contract No. N00024-79-C-5679, March 1981.